Conceptual design of wave energy converters

by

Kush Bubbar
B.Sc., University of Waterloo, 2004
M.Eng, University of Waterloo, 2010

A Dissertation Submitted in Partial Fulfillment
of the Requirements for the Degree of

DOCTOR OF PHILOSOPHY

in the Department of Mechanical Engineering

University of Victoria

Supervisory Committee

Conceptual design of wave energy converters

by

Kush Bubbar
B.Sc., University of Waterloo, 2004
M.Eng, University of Waterloo, 2010

Supervisory Committee

Dr. Bradley Buckham, Department of Mechanical Engineering
Co-Supervisor

Dr. Peter Wild, Department of Mechanical Engineering
Co-Supervisor

Dr. Panajotis Agathoklis, Department of Electrical Engineering
Outside Member

Abstract

Despite presenting a vast opportunity as a renewable energy resource, ocean wave energy has yet to gain commercial success due to the design space being divergent. To facilitate convergence, this dissertation has proposed a method using the mechanical circuit framework to transform a linear representation of any wave energy converter into an equivalent single body absorber, or canonical form, through the systematic application of Thévenin's theorem. Once the canonical form for a WEC has been established, criteria originally derived to maximize power capture in single body absorbers is then applied.

Through this process, a master-slave relationship was introduced that relates the geometry and PTO parameters of a wave energy converter device to one another and presents a new method to establish the best possible power capture in analytical form based on dynamic response. This method has been applied to reprove the power capture limits derived by Falnes and Korde for their point absorber devices, and proceeds to introduce a new analytical power capture limit for the self-reacting point absorber architecture, while concurrently establishing design criteria required to achieve the limit. A new technology, the inerter, has been introduced as a means to implement the design criteria.

The method has been further developed to establish the generic optimal phase control conditions for complex WEC architectures. In doing so, generic equations have been derived that describe how a geometry control feature set is used to satisfy the required optimal phase criteria. Finally, this dissertation has demonstrated that applying this method with a generic reactive force source enacting the geometry control establishes

analytical optimal conditions on the force source to achieve optimal power capture. This work revealed how the analytical equations defining the optimal force source reactance derived in this dissertation for self-reacting point absorbers represents a tangible design constraint prior to specifying how that constraint must be satisfied. As the force source is generic and conceptual, substitution with a physical embodiment must adhere to this constraint thus, steering technology innovation.

Table of Contents

List of Tables

List of Figures

Acknowledgments

As any graduate student can attest, a dissertation is never the product of a sole individual's effort, but rather of a consortium of individuals all playing different support roles. As such, personal gratitude goes to my supervisory team; Professor Peter Wild for being the voice of reason whenever I strayed too far from my original objectives; and Dr. Bradley Buckham for his gentle mentorship in steering me into the unknown.

I would also like to thank Dr. Scotty Beatty and Mr. Bryce Bocking for diving into and sticking with our intense experimental WEC trials on the opposite side of the country.

Finally, I would like to thank my wife Meaghan for encouraging me to return to graduate school for a second time to begin this wonderful journey of exploration and reflection, and my wonderful children, Elani and Kaelan for all the sacrifices they had to endure while daddy was at school "learning".

Dedication

To my wife Meaghan for encouraging and supporting me to seek out my passion, while reminding me not to forget what matters most in life.

1 Introduction

For a planet in peril, the transition of the global energy economy from fossil fuel to renewable energy sources is often viewed as an imperative evolution for the long term survival of mankind. Of the available renewable energy resources, ocean wave energy is often perceived as the last untapped source [1]. Although the ocean is observed as a harsh environmental resource to tame, there are several positive drivers for seeking a means to harness wave energy. Three primary motivations are: 1) ocean waves are a high-density energy resource with the global average being at least ten times more dense, on a per unit area basis, than the average solar flux [2,3], 2) relative to alternative renewable energy resources, the resource is highly predictable allowing for less uncertainty in operating a stable energy network [4], and 3) in regions distant from the equator, the wave energy density peaks in the winter season, complementing with the solar and wind energy resources to, as a combined resource, satisfy local annual energy demand [3]. Although there is a clear benefit of extracting energy from ocean waves, commercial scale deployments of Wave Energy Converter (WEC) devices have yet to gain traction.

1.1 Overview of the Economics of WEC Development

A primary factor in dissuading market investment in WEC development is the relatively high Cost of Energy (CoE) in relation to alternative renewable sources [5]. Based on a recent report by the International Renewable Energy Agency[1], the CoE of WEC devices considered range from 0.33-0.63/kWh requiring a reduction by a factor of

[1] Kempener R., Neumann F., IRENA Ocean Energy Technology Brief 4, International Renewable Energy Agency (IRENA), June 2014

two to realize economic viability [6]. To realize reductions in CoE, efforts must focus on promoting the convergence of designs with a strong predicted power producing potential, while concurrently maturing supply chain logistics to reduce capital (CAPEX) and operating (OPEX) expenditures. At present, advancement in power production of WEC devices is challenging today as WEC development resides within a divergent design space — numerous new WEC devices are regularly introduced proclaiming to represent the future in WEC technology diluting collective progress. In recognition of this paramount need to reduce CoE, Weber [7,8] introduced the Technology Performance Level (TPL) versus Technology Readiness Level (TRL) matrix in Figure 1.

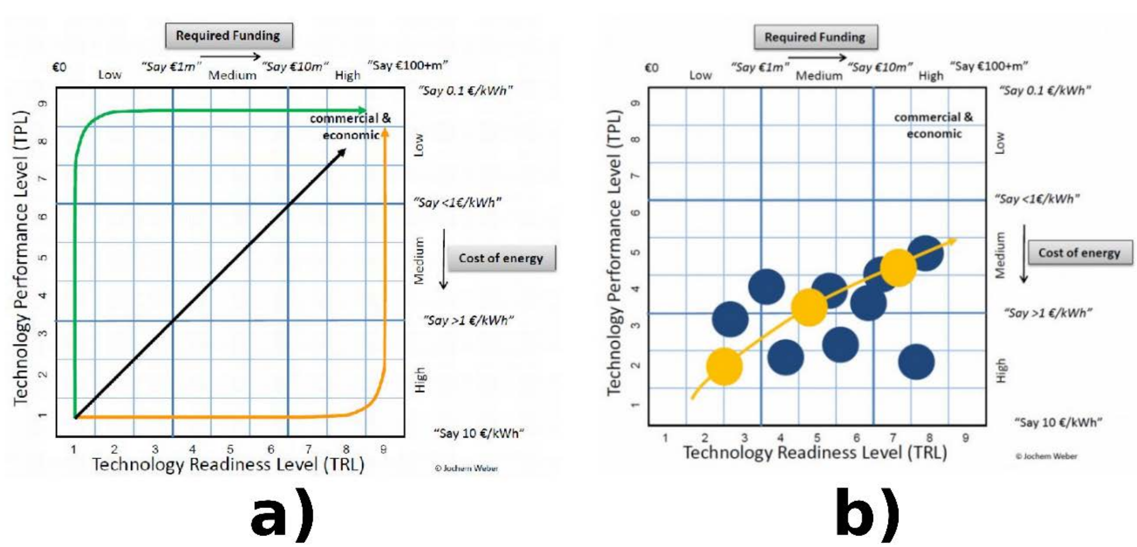

Figure 1: Technology Readiness Level versus Technology Performance Level Matrix [7]

The intent of the matrix is to persuade a WEC developer to follow a trajectory for which ideally TPL leads TRL (i.e. "Performance before Readiness" as observed in the green curve of **Figure 1**a). This approach emphasizes early stage evaluation of WEC performance via numerical modeling and experimental testing of scaled prototypes to ensure performance levels are adequate for economic feasibility prior to investing in maturing a technology for manufacture. Such a trajectory directly supports established systems engineering methodologies to minimize the probability of major design changes late in a development program which will inherently undermine investment to generate an economy of scale [9]. Following this trajectory requires establishing the best possible TPL and the associated design constraints for achieving this maximum at an early stage of a WEC development program. These design insights are invaluable at the early stages to define a performance metric to compare WEC configurations. In **Figure 1**b, it is curious to note Weber's observation from a selection of WEC programs represented by the blue dots, that WEC developers have a tendency to proceed along the opposite trajectory (i.e. "Readiness before Performance") [7]. As a metric, TPL is defined as the ratio of currency per unit energy (e.g. $/kWh). Based on this definition, a project may improve TPL by either reducing the CAPEX and OPEX cost and / or increasing the energy conversion efficiency. This dissertation focuses on defining the conditions to improve TPL through increasing the energy conversion efficiency.

1.2 Overview of the Ocean Wave Resource:

A vast resource of renewable energy exists due to ocean surface waves generated by wind-wave interactions [10]. Characterizing this wave resource begins with measuring surface elevation discretely as a function of time, defining a time series record. Assuming the time series record can be approximated as a superposition of a set of linear monochromatic surface waves, one can then apply the Discrete Fourier Transform (DFT) to yield the amplitude and relative phase contributions of the individual monochromatic surface waves superimposed to approximate the original wave elevation record in the time domain. Once these monochromatic wave components are determined, the data is typically represented as a histogram of the variance density spectrum, $S(\omega)$, of the monochromatic surface wave components as a function of frequency, while the phase information is discarded. This histogram data is then fit to the empirical Pierson-Moskowitz (PM) spectrum [10] to further simplify the data representation. Finally, over the course of a longer time period (e.g. one year) the number of instances for which the resource is represented by a particular PM spectrum is recorded, binned, and represented by a 2D histogram known as a power spectral density plot. In this sense, the estimation of the wave resource fundamentally assumes a superposition of planar surface waves and thus, aligns well with frequency domain modelling of wave energy converter dynamics. Alternatively, wind generated spectral models such as Simulating Waves Nearshore (SWAN)[2] can also be utilized to develop wave resource predictions and ultimately the free surface elevation profile. However, the same fundamental assumption of a superposition of planar surface waves is also at the core of SWAN.

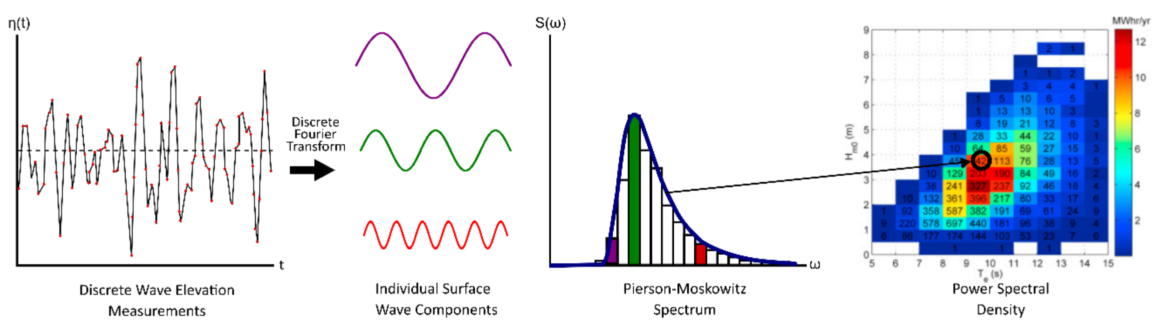

Figure 2: Example Spectral Representation of the Wave Energy Resource at a Geographical Site[3]

1.3 WEC Classification

WECs come in all shapes and sizes and are thus capable of harnessing energy from the wave resource using a multitude of methods [11]. This occurs as, in its most fundamental

[2] SWAN website, https://www.tudelft.nl/en/ceg/about-faculty/departments/hydraulic-engineering/sections/environmental-fluid-mechanics/research/swan/, Accessed 20181213

[3] Power spectral density plot obtained from, doi.org/10.1016/j.renene.2014.06.020

form, wave energy capture is the result of deconstructive interference between the incident and radiated wave fronts [12]. Therefore, any WEC device capable of realizing a deconstructive interference regime has the capacity to capture energy from a wave. A WEC realizes this through its own oscillatory motion generated via wave excitation. As a result, there is a wide diversity of devices capable of achieving this requirement and a classification scheme has been devised to define device classes based upon the operating principle of the WEC [1]. These classes include: 1) attenuators — elongated floating WEC with the dominant operating orientation parallel to the direction of the incident wave, 2) terminators — elongated floating WEC with the dominant operating orientation perpendicular to the direction of the incident wave, and 3) point absorber — WEC axis symmetric about a vertical axis and capable of accepting wave fronts from any direction.

Although this classification scheme is based upon operating principle, many devices across these classes may be represented by the same topology. For example, the bottom mounted surging flap (i.e. attenuator) and the Single Body Point Absorber (SBPA) (i.e point absorber) are ideally represented using the same topology (see Figure 3), but are based on a different dynamic representation (e.g. translation versus rotation).

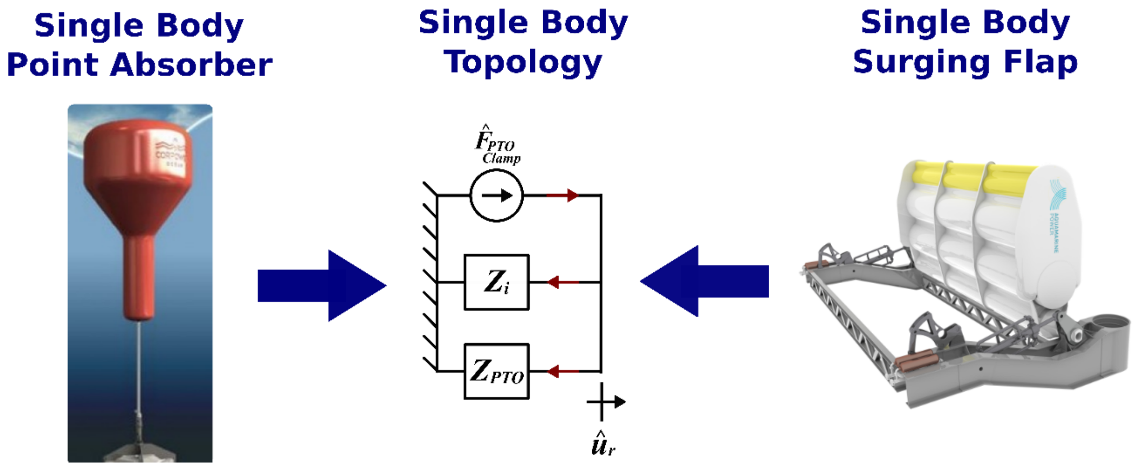

Figure 3: Example of Two[4,5] WEC Configurations of Different Classes Represented by the Same Topology

In both of these WECs the energy captured by the Power-Take Off (PTO) is maximized when resonance between the WEC and the hydrodynamic wave excitation force is achieved. The application of the mechanical circuit framework introduced in this dissertation provides a methodical process to determine these resonant conditions in analytical form irrespective of WEC class, provided the goal of maximizing WEC power capture is achieved at resonance. The resonant conditions are represented in analytical form as a constraint equation relating the various design parameters. The analytical form is critical as WEC developers may calculate general parameters from the constraint equations without locking down the design. In essence, adhering to the analytical constraint equations represent design insight to maximize power capture. To ensure the constraint equations are satisfied, control systems must be implemented into a WEC

[4]CorPower™~https://www.renewableenergymagazine.com/ocean_energy/corpower-ocean-to-test-wave-energy-converter-20160203, Accessed 2018-08-18

[5]Oyster2™~http://www.renewableenergyfocus.com/view/9523/aquamarine-power-unveils-oyster-2-design/, Accessed 2018-08-18

device as discussed in Section 1.5. For the context of this dissertation, devices classified as heaving point absorbers are only considered based on the availability of experimentally validated data at the University of Victoria [13] used for performing the ensuing analyses.

1.4 Frequency Domain Modelling of WEC Dynamics

Residing in a divergent design space, the challenge of an early stage WEC development program is an awareness of the complex relationships between the various WEC components and their influence on the WEC power capture performance. Analytical methods of modelling WEC dynamics are consistent with the needs of an early stage development process as they deliver families of analytical solutions relating the power capture to the various WEC design parameters; however, they fall short in terms of fidelity as they require a linear representation of the associated physics in order to permit representation in the frequency domain. Alternatively, time domain models of the WEC dynamics, offer the ability to describe more accurately the non-linear physical effects in the time domain, but at the cost of evaluating the performance for a specific configuration only. As an intermediary, non-linear frequency domain modelling approaches have recently been considered for modeling WEC devices demonstrating promising potential for assessing power production without the computational requirements of time domain models [14]. In recognition of the need to explore a wide possibility of WEC designs in a divergent design space, the convention in wave energy conversion is to initially build a frequency domain model.

It is typical to represent the frequency domain dynamic equations of motion using phasor notation [12]. This convention is based upon a series of specific assumptions on the underlying WEC system. First, the WEC dynamics must be linear and represented using a lumped parameter model with Linear Time-Invariant (LTI) coefficients yielding an Ordinary Differential Equation (ODE) defining the motion of each body in the WEC at each excitation frequency considered. Second, the WEC system must be experiencing a linear sinusoidal external excitation force. Finally, the system must be asymptotically stable. For such a system operating under steady-state conditions, the complete solution describing the ensuing motion of each body is approximated by the particular solution of the ODE, as the homogeneous solution will decay exponentially to zero in time. The particular solution illustrates the steady-state oscillatory motion of each body at a single wave excitation frequency. At each wave excitation frequency, each set of linear force inputs results in motion of the corresponding bodies at the same frequency. Therefore, frequency domain analysis underpins the study of WEC dynamics for which the state variables are defined by each body's amplitude and relative phase. Such a problem is well-represented using complex phasors relating the forces in the system to the resulting body velocities through a transfer function known as the mechanical impedance. The benefit of applying this phasor / impedance method is the amplitude and phase coefficients may be determined through mere algebraic manipulation rather than directly solving the system ODEs.

1.4.1 Mechanical Impedance Representation of a Heaving Vibration System:

The mechanical impedance (Z) is a complex number representing a frequency domain transfer function between a measured complex force amplitude $(\hat{F})$ and the measured difference in complex velocity amplitude $(\hat{u}_1 - \hat{u}_2)$ as detailed in (1) [15].

$$\hat{F} = Z(\hat{u}_1 - \hat{u}_2) \tag{1}$$

As a complex number, the impedance is constructed as a combination of a resistance and a reactance term detailed in (2) with: i) R representing the mechanical resistance coefficient defining the energy dissipation due to mechanical viscous damping over a cycle; ii) X representing the mechanical reactance coefficient defining the temporary energy storage over a cycle due to inertial effects. These bulk quantities are represented by the four basic elements detailed below.

$$Z = R + iX \tag{2}$$

In a mechanical vibration system subject to the conditions in Section 1.4, there exist four basic elements — masses, springs, dampers, and inerters [15,16] for which the mathematical representation of the mechanical impedance of the first three can be found in Bubbar et al. [17] (cf. Table 1), and the last in Bubbar and Buckham [18] (cf. Table 1) included in the Appendices. As such, physical mechanical vibration systems that comprise these four basic elements may be topologically represented as an interconnection of these basic elements otherwise known as a mechanical circuit.

Once a mechanical vibration system is represented as a mechanical circuit, parallel and series circuit transformations may be performed to simplify the circuit by combining the impedances of these basic interconnected elements into an effective single impedance element. When comparing electrical and mechanical circuits, it is important to note that the through and across variable definitions are not analogous. In electrical circuits, voltage is the potential variable and is represented as an “across” variable whereas current is represented as the “through” variable. This contradicts with mechanical circuits as force is the potential variable that is represented as a "through" variable and velocity is an "across" variable. These details are summarized in Table I.

Table I: Comparison of Through and Across Variable Representations for Electrical and Mechanical Circuits

Domain:	Across Variable:	Through Variable:
Electrical	Voltage	Current
Mechanical	Velocity	Force

This reciprocal relationship between the definitions of variables in each physical domain leads to a reciprocal relationship with the parallel and series equivalent impedance transformations in the mechanical domain as demonstrated in Figure 4 and expressed in equations (3) and (4).

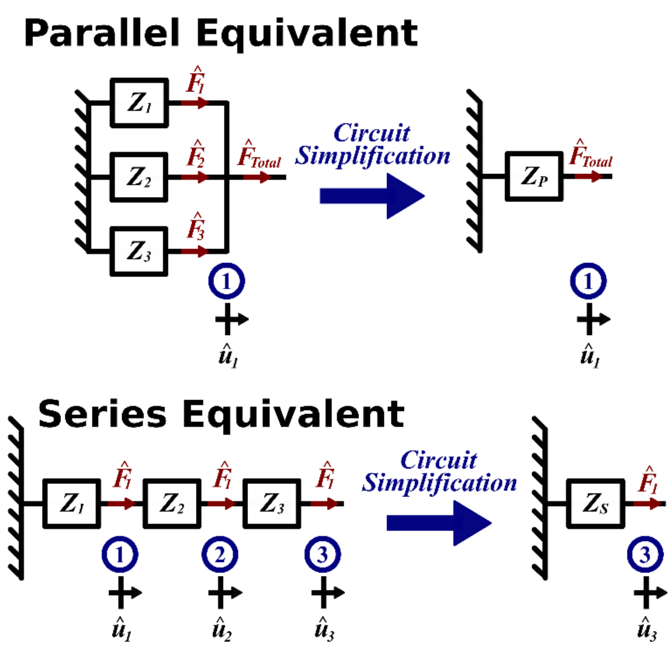

Figure 4: Mechanical Circuit Representations of the Parallel and Series Equivalent Transformations

$$\frac{1}{Z_S} = \sum_{k=1}^{n} \frac{1}{Z_k} \tag{3}$$

$$Z_P = \sum_{k=1}^{n} Z_k \tag{4}$$

Equations governing the system dynamics may be generated through applying Kirchhoff’s conservation laws when considering topological orientation: 1) Node Law — sum of all forces into a velocity node is equal to zero, 2) Loop Law — sum of relative velocities across elements in a closed loop is zero (cf. Figure 10.20 [15]). Finally, equivalent circuit transformations may be applied to a mechanical circuit at the insertion point of a mechanical load to transform the original circuit into an alternative equivalent circuit. These circuits include Thévenin, Norton, T, and π circuits [15], and for the context of this dissertation, the Thévenin equivalent circuit [19], represented as a force source in parallel with an intrinsic mechanical impedance and mechanical load, is applied to transform a complex WEC architecture into canonical form. The reciprocal relationship between the through and across variables also leads to reciprocal representation of the circuit topologies for the Thévenin and Norton equivalent circuits. Figure 5 represents the process of generating a mechanical circuit for a: 1) Single Body Point Absorber (SBPA) at the top, and 2) Self-Reacting Point Absorber (SRPA) at the bottom.

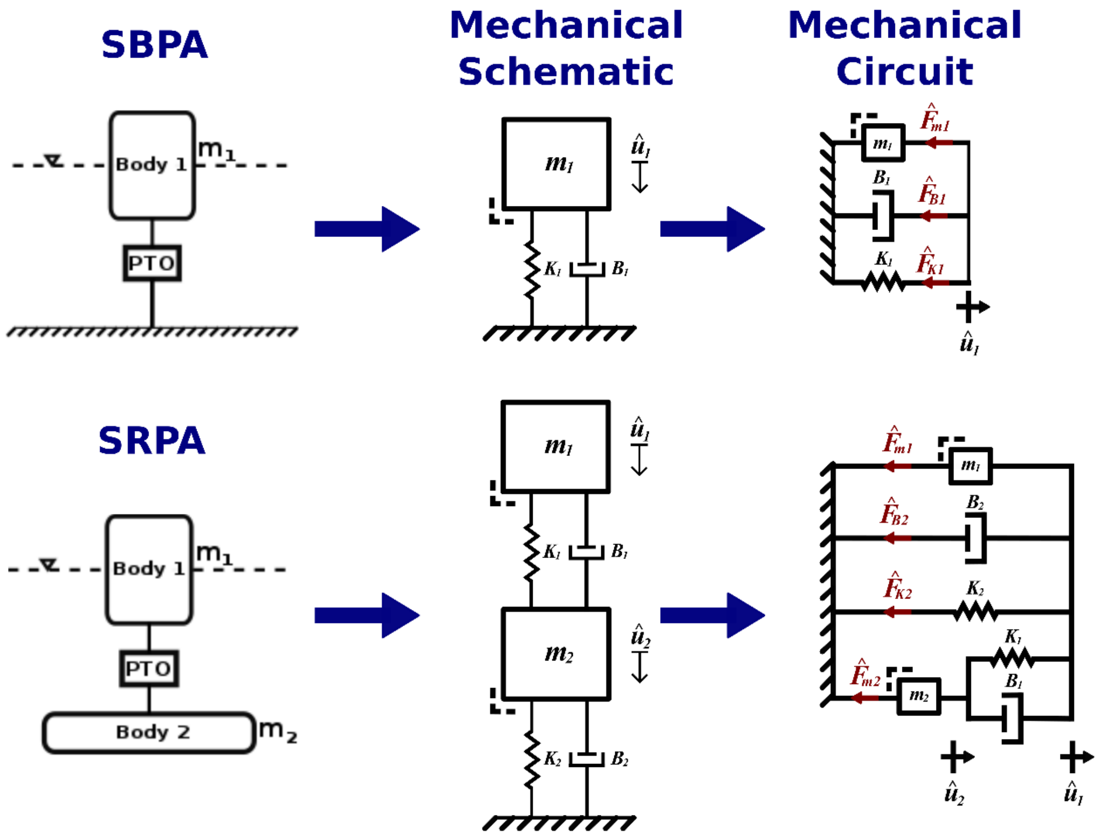

Figure 5: Pictorial Process of Generating a Mechanical Circuit from SBPA (top) and SRPA (bottom) WEC Architectures

1.4.2 Overview of Linear Wave Hydrodynamics:

One of the challenges in offshore ocean engineering is modelling the fluid interaction with large floating rigid bodies, as a complete non-linear hydrodynamic model requires heavy computational resources. As such, a simplified model of the wave hydrodynamic forces is often employed based on the assumption of potential flow combined with a linearization of system boundary conditions [20,21]. When considering a monochromatic planar surface wave as an input, this simplification of the wave hydrodynamics problem is approximated as a superposition of individual hydrodynamic force components on each floating body evaluated under independent conditions. These hydrodynamic components include the wave excitation force, the radiation force, the hydrostatic force, and the linearized drag force. The wave excitation force is decomposed into the diffraction and the Froude-Krylov (FK) forces. The diffraction force is the force experienced on a body fixed in space at its mean position by an incident wave field when that incident wave field is scattered by the presence of that body. The FK force on the other hand is determined under the same conditions except the body is transparent to the incident wave field (i.e. the FK force is the sum of the pressure field at the fluid-WEC interface in the absence of the WEC). Both components of the excitation force are related to the amplitude and phase of the incident wave. Next, the radiation forces are the result of water displacement in the vicinity of the moving bodies in the absence of an incident wave field. The radiation forces are also decomposed into the radiation damping and added mass forces [21]. The radiation damping force is the reaction force due to the oscillatory motion of a body generating waves that propagate away from the body. The added mass on the other hand is associated with oscillatory acceleration of water at the free surface in close proximity to the body, and results in an inertial force [22]. The hydrostatic force is the net force between gravity and the Archimedes buoyancy force. For bodies with a constant surface piercing area oscillating under the small amplitude approximation, the buoyancy force is linearly proportional to the instantaneous body displacement. This proportionality constant is termed the buoyancy stiffness and is treated as a constant across the frequency spectrum. The final hydrodynamic force considered is linearized drag. Drag is typically described using the empirical Morison equation that assumes a quadratic relationship between the body and fluid velocity. Such a representation violates the linear description of resistive damping required for a frequency domain model. Accordingly, the drag force must be linearized to fit a viscous damping representation [23]. The wave excitation and radiation forces are defined via state coefficients often obtained through the application of software tools that implement the panelized mesh-based Boundary Element Method (BEM). Software tools implementing BEM include WAMIT[6], and NEMOH[7]. However, standard BEM codes do not determine the linearized drag coefficient. The linearized drag coefficient can be obtained through applying system identification methods, which include impulse excitations on a physical model, or through application of mesh-based Computational Fluid Dynamics (CFD) simulations. For the WECs under study in this dissertation, defined in Section 2.4, the linearized drag coefficient was determined by Beatty et al. using the former method and is assumed to be constant across the frequency spectrum [24]. One such system identification technique is the equivalent energy method for which the energy dissipated through a cycle of a non-linear viscous drag process is equated to the equivalent energy that would be dissipated via a linear resistive process over the same period.

1.4.3 Other Forces in a WEC System:

The remaining forces often considered in a WEC system, consist of reaction forces from mechanical machinery — including the PTO, moorings, and reactive force sources. The PTO is the device in a WEC responsible for converting the kinetic motion of the floating rigid bodies into a useful form for future consumption (e.g. electricity). In the frequency domain, the PTO is often modelled as a tunable generic complex impedance element consisting of a resistance and reactance each with a separate role. The PTO

---

[6] https://www.wamit.com/, Accessed 2018-08-21.

[7] https://lheea.ec-nantes.fr/logiciels-et-brevets/nemoh-presentation-192863.kjsp, Accessed 2018-08-21.

resistance is responsible for representing the reaction force for which the floating body does work against to capture useful power. The PTO reactance represents the reaction force response of a temporary energy reservoir for the kinetic motion of the WEC, which alters the inertial dynamics of the WEC. The role of tuning the PTO reactance is to invoke resonant conditions between the WEC bodies and the wave excitation force.

The traditional role of the mooring is designed for station keeping, however active and reactive roles have been proposed in literature [25]. In general, mooring dynamics are a non-linear phenomena and modelling in the frequency domain requires the application of a linearization scheme. In these schemes the linear mooring parameters are derived from non-linear time domain models which often introduce errors in the final predictions [25] and are thus frequently excluded from frequency domain analysis.

The final element is the generic reactive force source often used by Korde [26–28] to represent a generalized inertial force response. As will be shown in this dissertation via Article 2 (Appendix B) and Article 3 (Appendix C), the reactive force source can be used as a placeholder within the power capture analysis of a WEC system to identify design insight in the form of constraint equations, for the optimal design of a WEC subsystem.

1.5 Controlling WEC Energy Conversion

In Section 1.1, the discussion focused on the necessity for improving the power capture performance of WEC devices for realizing their economic viability. A method to realize this performance improvement is to introduce control techniques into a WEC design that induce the conditions that maximize the power captured. By choosing to model WEC devices in the frequency domain, the WEC is represented as a vibration system with maximum power captured when the device is operating in resonance with the incoming wave excitation force.

Identifying resonant conditions for WEC devices with simple topologies is relatively straightforward at the conceptual stage of development. However, as topologies evolve in complexity to meet the demands of improving overall power capture, determining the resonant conditions for these complex WECs is inherently more difficult as discussed in Section 2.1. If WEC developers do not consider how to implement energy maximizing control strategies into more complex WEC designs during the conceptual stage of a development program, the risk that a particular WEC design does not deliver sufficient power production and satisfy the requirements for economic viability is high. Therefore, it is an important step in the conceptual design phase of a development program to identify both the: 1) power producing potential of a WEC, and 2) technical operating conditions for that WEC to achieve that potential. It is a natural preliminary step to approach this problem in the frequency domain with the objective of this dissertation to present a methodology for which both of these steps can be achieved.

1.6 Research Objectives:

To summarize the premise of this chapter, it is clear that the power capture performance of WECs must improve. WEC technology resides in a divergent design space, therefore to focus efforts on WEC devices with the largest power capture potential, WEC developers should invest resources to assess and mature TPL while a program is at low TRL. Assessing TPL at low TRL is difficult. This dissertation contends that at low TRL, there is a strong correlation of TPL with the analytical power capture upper bound. To assess the feasibility of approaching the upper bound, the conditions or analytical constraint equations for invoking the upper bound should be determined to identify design insight. Therefore, at low TRL a WEC developer may assess the feasibility of adhering to the constraint equations by exploring various technological solutions required to achieve the desired upper bound. To successfully identify the power capture upper bound and the associated design insight, a formulaic method must be introduced.

The objectives of this dissertation may be summarized as follows:

1.6.1 Objective 1 (OBJ1)

Identify a framework for which the analytical representation of the power capture upper bound of any WEC architecture may be determined.

1.6.2 Objective 2 (OBJ2)

Identify a method consistent with Newtonian dynamics to determine the conditions for which the power capture upper bound can be approached (i.e. design insight).

1.6.3 Objective 3 (OBJ3)

Validate the proposed method through verifying the analytical results against previously published work on point absorber WEC architectures.

1.6.4 Objective 4 (OBJ4)

Apply these analytical methods in a case study on a self-reacting point absorber with a geometry control feature set to extract design guidance.

1.6.5 Objective 5 (OBJ5)

Propose a new method for investigating new WEC innovations at the conceptual stage of the development process.

1.6.6 Objective 6 (OBJ6)

Propose a new technology, the inerter, which is capable of implementing the design insight to approach the power capture upper bound.

1.6.7 Objective 7 (OBJ7)

Identify a method to generalize the analytical phase control conditions for resonant WECs.

1.6.8 Objective 8 (OBJ8)

Investigate new design functions within the WEC architectures considered in this dissertation, identified using the proposed analytical framework.

1.7 Organization of this Dissertation

This dissertation is presented in manuscript style and is based on three individual manuscripts specifying the research developments found in Appendices A, B, and C. Each of these manuscripts has been published or is currently under review at a relevant international journal focusing on renewable energy research. The dissertation is organized to include: Chapter 1 — introduction to the ocean wave energy resource and WEC dynamics, Chapter 2 — review of the pertinent technical background relating to WEC control, and the identification of gaps in the research literature, Chapter 3 — detailed overview of the contributions of each manuscript in the appendices, and Chapter 4 — presents opportunities for future work. As a note, the detailed conclusions for each article listed in this dissertation are found in the individual articles reproduced in the Appendices. A summary of the conclusions for each article are found at the end of Sections 3.1-3.3.

2 Literature Review and Research Gaps

To frame the contributions in Section 3, the motivation of this section is to present the pertinent literature on: 1) frequency domain control of WECs, 2) the established power capture upper bounds in wave energy conversion, 3) the identified gaps related to both 1) and 2) in the context of conceptual design of WECs. This section concludes with a description of the WEC configurations used as case studies to validate the claims in this dissertation.

2.1 Literature Review on Frequency Domain Control of WECs

Section 1.1 stated that step reductions in the CoE from wave energy converters must be achieved for WEC technology to become economically viable [6]. It is well understood amongst the wave energy research community that the implementation of control technologies are vitally important for increasing the power capture capacity of a WEC device which can lead to a reduction in CoE [3,12,22,29–31]. This proposal is based on the premise that increasing the power capture performance requires inducing a resonant state between the motion of the WEC and the incoming excitation force. This argument was verified by several researchers whom independently derived the conditions for optimal power capture for the SBPA architecture, demonstrating such a condition occurred at resonance [32–34]. This formulation of the power capture control problem for the heaving point absorber was based upon identifying the optimal frequency dependent complex body velocity amplitude of the SBPA, which occurs when the PTO resistance is set equal to the radiation damping coefficient of the WEC body as in equation (5), while the sum of the total reactance of the PTO and the remaining WEC is zero as in equation (6) [32].

$$R_{PTO_{opt}} = R_i \tag{5}$$

$$X_{PTO} + X_i = 0 \tag{6}$$

Falnes recognized that equation (6) could be achieved if the PTO reactance was manipulated to satisfy equation (6) yielding equation (7). With this choice of requiring the PTO reactance to follow the intrinsic reactance of the SBPA, the combination of equations (5) and (7) could be creatively represented as a single complex constraint equation in (8).

$$X_{PTO_{opt}} = -X_i \tag{7}$$

$$Z_{PTO_{opt}} = Z_i^* \tag{8}$$

Falnes interpreted equation (8) as a mechanical impedance matching problem analogous of the problem defined in electrical antenna theory [35]. In other words, the PTO was functionally responsible for injecting reactance into the WEC to invoke resonance. Such a system configuration adhering to equation (8) is known as implementing optimal PTO force control. This representation is only a specific case represented by equation (6), which generically stated that the combined PTO reactance and intrinsic reactance of the remaining WEC must equal zero. This subtle difference has influenced WEC development to focus on PTO designs capable of invoking resonance in SBPAs [29,36–38].

As implied above, WEC control is not limited to only PTO force control. An alternative form of control is geometry control. As defined by Price [39], a geometry controlled SBPA WEC, represented by the mechanical circuit in Figure 3, is a device which possesses the ability to change the intrinsic impedance, $Z_i(\Lambda)$, and / or wave excitation force, $\hat{F}_{PTO_{Clamp}}(\Lambda)$ as a function of a geometric parameter (Λ). As such, geometry control can be realized through the implementation of features that include inertial modulation and / or physical changes to hull geometry. Based on this definition, a geometry controlled WEC could be utilized to invoke resonance through implementing equation (6) as in equation (9).

$$X_{PTO} + X_i(\Lambda) = 0 \tag{9}$$

In the special case for which a resistive only PTO is considered (i.e. $X_{PTO} = 0$), equation (9) leads to equation (10) for which the geometric parameter is solely utilized to invoke resonance. This control regime is known as optimal geometry control. In essence, for an SBPA, resonance can be invoked by either implementing: 1) optimal PTO force control, 2) optimal geometry control, or 3) some combination of both. For the special case of an SBPA in which the physical hull geometry remains constant, the theoretical power capture of all three cases will be the same.

$$X_i(\Lambda) = \Im m\{Z_i(\Lambda)\} = 0 \tag{10}$$

With more complex WEC architectures (e.g. SRPA with a geometry controlled spar), the choice of the WEC control strategy does influence the power capture potential. SRPAs are topologically represented as a PTO interfaced between two wave activated bodies. As discussed in Section 1.4.1, determining the resonant conditions for the SRPA requires first applying Thévenin's theorem to establish the canonical form followed by forming the impedance matching problem.

There is a catch however. Resonance is technically only defined for a single body system (i.e. SBPA). With a multibody system, such as the SRPA, an external sinusoidal force leads to a multibody response described via modal analysis. As such, it is not clear whether a resonant condition identified with impedance matching of the canonical form leads to a modal response for which power capture is maximized [2]. These conditions include a: 1) large relative motion between the SRPAs float and spar, and/or 2) large force transmitted through the PTO. As such, although the equivalent resonant conditions on the canonical form may be analytically established for more complex WEC architectures, selecting the most appropriate condition requires exploring each condition independently for its influence on power capture. As the complexity of WECs continues to grow, a formulaic method to establish these equivalent resonant conditions becomes more important.

2.2 Overview of WEC Power Capture Upper Bounds

To assess the analytical power capture potential of a WEC architecture it is prudent to present an overview of the existing bounds on power capture. In wave energy there are two predominant upper bounds derived based on different assumptions often described as: 1) Radiation Pattern Upper Bound, and 2) Budal's Upper Bound. Both bounds are described in the subsections below.

2.2.1 Radiation Pattern Upper Bound

In its most fundamental form, the wave energy conversion problem may be described in terms of a wave interference problem [33,34,40]. Since a planar surface wave is associated with a wave energy transport (J), conservation of energy dictates that the goal of a WEC is to generate a wave that deconstructively interferes with the incident wave such that energy in the wave resource is transferred to the WEC resulting in kinetic motion of the WEC [12]. For WECs in the point absorber class, the maximum power capture (per metre of wave front) due to deconstructive interference between the WEC's radiated pattern and the incident plane wave is expressed by equation (11), where λ is the wavelength of the incoming incident wave in metres, and α is an integer selected based on the WEC's radiation pattern as generated by a particular source type: $\alpha = 1$ for a monopole source, and $\alpha = 2$ for a dipole source.

$$P_a = J\alpha\left(\frac{\lambda}{2\pi}\right) \tag{11}$$

It is clear such an argument is based purely on wave mechanics and does not consider the dynamic response of the absorber to an excitation force. Although this expression serves to define upper bounds on the power capture capacity of a point absorber WEC, it is difficult to extract further guidance on how to design a WEC to approach the bound.

2.2.2 Budal's Upper Bound

An alternative upper bound was derived by Budal by considering volume stroke limitations of a WEC [41]. Beginning with a heaving SBPA WEC, Budal recognized such a device could maximize its power capture if the device was first operating under optimal phase control, hence enforcing equation (6). To further improve the power capture response of the SBPA WEC, Budal proposed maximizing the wave excitation force through enforcing the small body approximation to minimize the subtractive diffraction force, requiring the body cross section dimension to be significantly smaller than the wavelength of the incident wave. The final assumption was that the WEC was operating at its defined travel stroke limitation. In applying all of these conditions and assumptions, Budal's upper bound is defined as equation (12) [42][8] with ρ, g, A, T

---

[8] A mistake was identified in Falnes equation (A.6). The denominator should be $32\pi^3$ as in equation (12).

representing the density of water, the gravitational constant, the amplitude of the incoming wave field, and the period of the incoming wave field respectively.

$$P_b = \frac{\rho g^3 A^2 T^3}{32\pi^3} \tag{12}$$

To illustrate both upper bounds, an example plot of both the Radiation Pattern Upper Bound in red, Budal's Upper Bound in green, and a heaving sphere SBPA operating under complex-conjugate control in black is presented in Figure 6 [43]. Once again, it is difficult to design an SBPA, let alone a more complex WEC architecture, to approach these upper bounds based on the definitions of these limits.

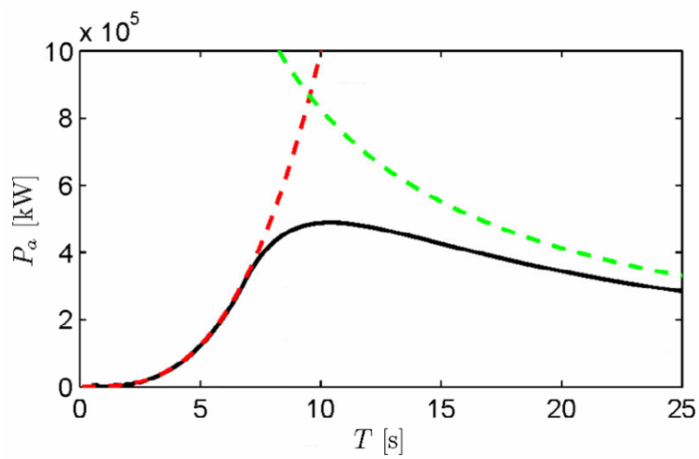

Figure 6: Example of WEC Power Capture Upper Bounds on a Spherical SBPA: Radiation (red), Budal (green), SBPA Operating Under Optimal Phase Control (black) [43]

2.3 Fundamental Research Gaps in Wave Energy Conversion

As detailed in Section 1, financial investments in designing and developing WEC devices must be derisked. To lower the development risk, a critical mass of developers must converge on promising architectures for rapid maturation. To identify promising architectures at an early stage of a development program, an analytical methodology to evaluate the power capture bound of an architecture based on dynamic response is required. In the absence of such a method, there exist challenges detailed in the following subsections.

2.3.1 Challenges with WEC Power Capture Limits

As specified in Section 2.2.1, the Radiation Pattern Upper Bound is derived based purely on a wave mechanics argument assuming deconstructive interference between the incoming and the outgoing radiated wave fields and thus, does not consider the device design whatsoever. Although the bound is consistent with the conservation of energy and presents developers with an absolute reference for comparing the performance of their designs against, it fails to provide guidance on specifically how to improve a WEC design to yield enhanced power capture. With the advent of more complex WEC architectures, the Radiation Pattern Upper Bound is still valid provided that the complex WEC architectures may be represented in canonical form.

In contrast, Budal's Upper Bound specified in Section 2.2.2, is based upon a series of cascaded assumptions. This first considers the dynamic response of a heaving SBPA WEC, while the subsequent assumptions do not. As such, these cascaded assumptions are likely to violate one another and are thus difficult to apply in the design of a WEC device. In addition, the assumption, which maximizes the excitation force in Budal's Upper Bound, assumes an SBPA architecture and has yet to be reconciled for more complex architectures in the point absorber class. For example, Beatty et al. [24] proposed an extension to Budal's Upper Bound for the SRPA architecture by defining a relative excitation force term, but later retracted the argument in his dissertation [40].

When comparing the two bounds, it is clear that neither the Radiation Pattern Upper Bound in equation (11), nor Budal's Upper Bound in equation (12) contain any reference to physical specifications of the WEC design, and thus do not supply guidance on how physical specification must be set to approach the bounds. In the absence of such a reference, a WEC designer must resort to trial and error methods, and is essentially designing blind. Finally, when comparing the assumptions that underpin both the Radiation Pattern Upper Bound with Budal's Upper Bound, it is clear they violate one another on a fundamental level [2], as the former requires a radiated wave to be generated by the WEC, while the latter assumes there is no wave radiation whatsoever. Even the point of intersection between the Radiation Patter and Budal's upper bound does not serve any direct significance as the underling conditions between each bound cannot be satisfied at this point.

2.3.2 Challenges of Deriving Analytical Power Capture Limits for Complex WEC Architectures

The complexity of WEC topologies continues to grow in the pursuit of further improvement in the overall power capture. This increased complexity requires the optimal selection of additional design parameters required to implement the more complex design features. These features include the implementation of both optimal PTO force control and optimal geometry control. The additional design parameters associated with these features lead to a more complex representation of the analytical power optimization problem yielding challenges.

For example, Korde introduced a complex point absorber WEC architecture as an SRPA with a reactive PTO and a geometry controlled force compensator [26]. In formulating the dynamic equations governing Korde's WEC, the analytical optimization problem required the selection of both the optimal PTO force parameters as well as the impedance of the force compensator to maximize the power capture. To set up such a multivariate analytical optimization problem, Korde formed an analytical constrained optimization problem with the governing dynamic equations of motion representing the constraint equations. In this formulation, solving for the conditions leading to optimal power capture required Korde to make a choice, setting the velocity of the compensated platform to zero, in order to proceed with the derivation. As demonstrated in Section 3.1, the enforcement of this constraint was unnecessary and led to the illusion of a single setting for the force compensator reactance to achieve the power capture bound when in fact there is an infinity of choices [17].

This example demonstrates the difficulty of analytically solving for the optimal power capture conditions of complex WEC architectures and the need for a formulaic method. The method presented in this dissertation is based on the seminal works of Falnes' impedance matching approach [12,44], but extended to include more complex WEC architectures with both PTO force control and geometry control features sets. As a reference, Figure 7 describes the formulaic methods of establishing the power capture upper bound for complex WEC architectures presented in this dissertation as a flow chart. The branches associated with ⓐ and ⓑ represent the choices of enforcing the master-slave relationship by enabling the PTO force control modes of complex-conjugate control and amplitude control respectively.

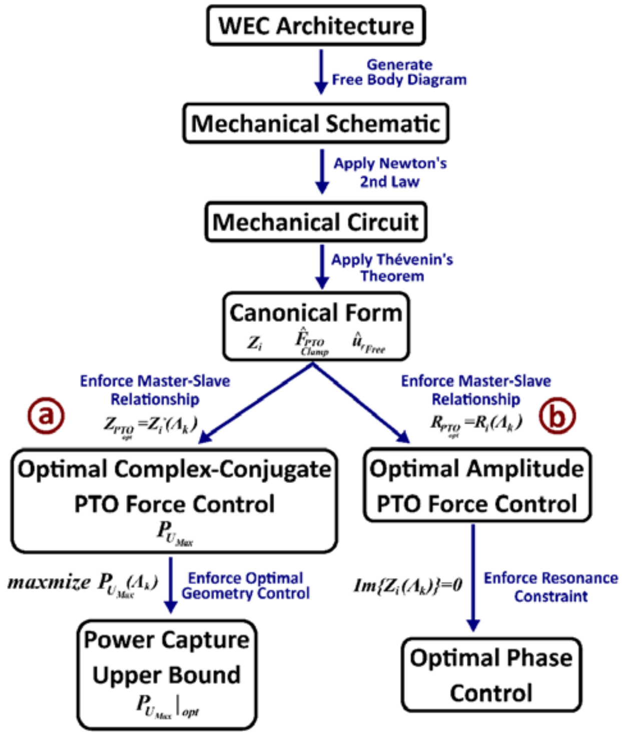

Figure 7: Flow Chart of the Formulaic Methods to Determine the Analytical Power Capture Limits Presented in this Dissertation with Λ_k Representing the k^{th} Geometry Parameter. Branches ⓐ and ⓑ represent the choices of enforcing the master-slave relationship by enabling complex-conjugate and amplitude control respectively via the PTO.

2.4 Overview of the Configurations Considered in this Dissertation

The methods presented in this dissertation to derive the maximum power capture conditions are generic and applicable to any WEC for which power capture is maximized when the canonical form representation of that WEC is in resonance. To validate the proposed methods and the accompanied equations, a choice was made to consider only SRPA heaving point absorbers as data for this configuration: 1) was available within my research group, and 2) had been published [24] and thus scrutinized via the peer review process.

To facilitate this process of outlining the case studies in this dissertation, a hierarchy is defined to categorize WEC designs comprising configuration, architecture, and class. A configuration is a design defined by a set of physical parameters governing the system characteristics (e.g. OPT Powerbuoy™). An architecture is the set of configurations that share the same device topology (e.g. SRPAs). A class is the set of architectures, which operate on the same physical principle (e.g. point absorbers). It is clear that a detailed performance analysis can only be performed on a configuration, however analytical equations defining optimal performance conditions can be derived at the architecture level. For example, Falnes' impedance matching criteria in equation (8) is an analytical constraint equation, which holds for all SBPAs regardless of the specific configuration, and is therefore derived at the architecture level.

Table II below establishes all of the configurations considered in this dissertation, classified by the article for which they appear. The configurations are linked back to an architecture for which the optimal equations were derived, along with a reference to a visual schematic of the architecture. For ease of reference, Figure 8 is a representation of both the Derived SRPA WEC Architecture and the Original SRPA WEC Architecture originally published in [18], and Arch1, Arch2, and Arch3 originally detailed in Article 3[9] currently under review respectively. It is important to note that the Original SRPA WEC Architecture and Arch1 represent the same architecture, and that the Derived SRPA WEC Architecture can be derived from Arch3.

[9] K. Bubbar, B. Buckham, On establishing generalized analytical phase control conditions in self-reacting point absorber wave energy converters, Renewable Energy. (2018); Under Review.

Manuscript is found in Appendix C.

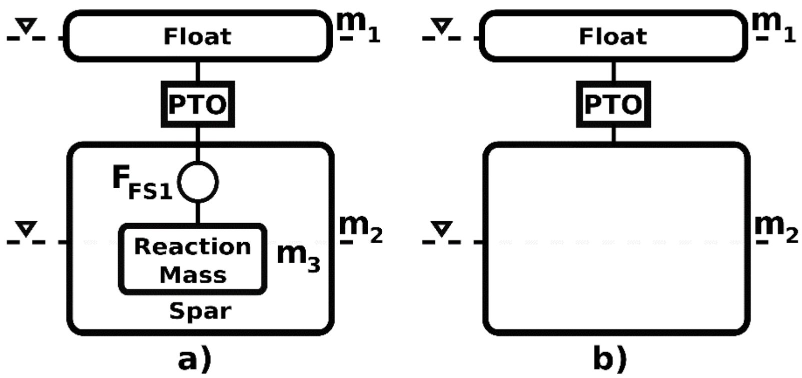

Figure 8: Mechanical schematics for the:

a) Derived SRPA WEC Architecture, b) Original SRPA WEC Architecture [18]

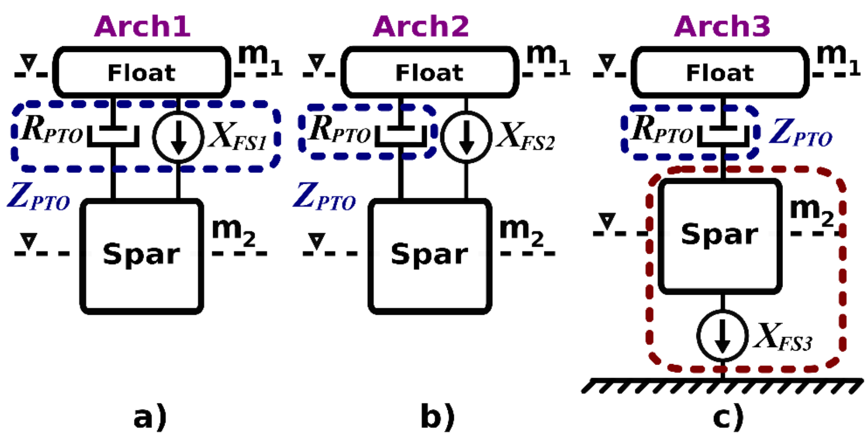

Figure 9: Mechanical schematics for architectures:

a) Arch1, b) Arch2, and c) Arch3[10]

To ensure equitable comparisons were conducted, the same hydrodynamic parameter set was applied verbatim to all configurations in this dissertation originating from Beatty et al. [24]. For the Derived SRPA WEC Configuration, Config3, and Config4, the mass of the original spar published by Beatty et al. [24] was equally divided between the spar

[10] Figure 2 from K. Bubbar, B. Buckham, *On establishing generalized analytical phase control conditions in self-reacting point absorber wave energy converters*, Renewable Energy. (2018); Submitted.

in these configurations and the internal reaction mass such that the mass of these configurations remained consistent with Beatty et al.'s original parameter definitions. Specific details of the hydrodynamic and inertial data used the build these configurations are found in both [13,24] and [17,18].

Table II: Definitions of Configurations Used as Case Studies in this Dissertation

Article #:	**Configuration:**	**Architecture:**	**Schematic:**
1	N/A	Falnes' SRPA	Figure 1b
1	N/A	SRPA + PTO Friction	Figure 1b
1	N/A	Korde's WEC	Figure 1c
2	Original SRPA WEC Configuration	Original SRPA WEC Architecture	Figure 3b
2	Derived SRPA WEC Configuration	Derived SRPA WEC Architecture	Figure 3a
3	Config1	Arch1	Figure 2a
3	Config2	Arch2	Figure 2b
3	Config3	Arch3	Figure 2c
3	Config4	Arch3	Figure 2c

3 Overview of Contributions

The motivation of the following section is to articulate each of the major contributions included in this dissertation organized by manuscript. Each subsequent subsection represents an overview of a manuscript and will briefly detail the research challenge encountered in that work followed by a summary of the contributions identified with the header CONT. The full manuscripts are included in Appendices A through C. A matrix mapping the contributions detailed in Sections 3.1-3.3 to the objectives listed in Section 1.6 can be found in Section 3.4 below.

3.1 Article 1 — A method to compare wave energy converter devices based on potential power capture[11]

The wave energy converter design space has been characterized as divergent resulting in a dispersion of resources slowing collective progress[12] [7,8,45]. The standard method for assessing WEC design performance requires specifying the device configuration, which inherently locks down the design. To facilitate the transition to a convergent design space, a technique capable of assessing the power capture potential of any WEC architecture at an analytical level is recommended by this work during the conceptual stage of a design program. The motivation of this article is to propose this technique, through building on the foundational mechanical impedance matching technique introduced into the wave energy community by Falnes [12]. The proposed method is based upon the hypothesis that maximizing power capture necessitates the selection of both the optimal geometric and PTO force parameters. Once the power capture upper bound is analytically determined for a WEC architecture, a WEC designer possesses a basis for establishing TPL at the conceptual stage of their development program.

A summary of the main contributions of this work follows:

3.1.1 Contribution 1 (CONT1)

Introduction of the mechanical circuit framework for extending the mechanical impedance matching technique originally introduced by Falnes [12] for WEC architectures of arbitrary complexity.

> The mechanical circuit framework presents a formulaic method to invoke Thévenin's theorem to represent a complex WEC architecture as a phenomenological single body WEC or canonical form. Once in canonical form, Falnes' impedance matching criteria is exercised to guarantee device resonance with the incoming wave excitation force independent of the device geometry.

3.1.2 Contribution 2 (CONT2)

Introduction of the *master-slave relationship* describing the relationship between the optimal geometry and PTO force parameters for achieving the power capture upper bound.

> The premise of this contribution is based on the notion that resonance between the WEC device and the incoming wave excitation force is only a sufficient condition for achieving the power capture upper bound. An equally important factor is the selection of the optimal WEC geometry. This work proposes the dependent master-slave relationship of the PTO force response (slave) on the WEC geometry (master). As such, to optimize the WEC system for power

capture, the WEC geometry must be optimized subject to enforcing device resonance via the master-slave relationship. This is a critical point for WEC developers seeking to discover an optimal design.

3.1.3 Contribution 3 (CONT3)

Proposed the phenomenological single body equivalent WEC, originally introduced by Falnes [44], as a canonical form (i.e. the simplest topology any WEC device may be represented by).

The WEC canonical form is obtained through applying the Thévenin equivalent circuit transformation on a complex WEC architecture resulting in an equivalent single body WEC architecture. Once the complex WEC architecture is represented in canonical form, apples to apples comparisons can be performed at the architectural level instead of the configuration level where design parameters must be specified.

3.1.4 Contribution 4 (CONT4)

A parallel representation of the mechanical circuit topology for the Thévenin equivalent phenomenological single body WEC architecture (i.e. canonical form) is proposed, which is in contrast to the series representation currently published in literature [3,21,22,46].

The proposed parallel representation is justified through applying accepted conservation principles [15] to the parallel circuit representation to rederive the governing equations of dynamic motion accepted by the wave energy community describing the conditions for optimal power capture.

3.1.5 Contribution 5 (CONT5)

Successfully applied the mechanical circuit framework to a case study of three different WEC architectures of increasing complexity.

> In these case studies each WEC architecture was represented by a mechanical circuit followed by application of Thévenin's theorem to transform the complex architecture into canonical form. Once in canonical form the master-slave relationship was enforced leading to the power capture upper bound.
>
> These WEC architectures included: 1) rederiving Falnes' analytical optimal power capture solutions to the SRPA architecture [44] and thus validating the mechanical circuit technique, 2) introducing linearized viscous damping into the PTO model of the SRPA architecture and demonstrating a counterintuitive result for which the PTO resistance must increase in unison of the viscous damping to ensure maximum power capture, and 3) deriving the generalized analytical optimal power capture solution to a complex point absorber introduced by Korde [26] and demonstrating new operational insight into this device — the reactive force compensator does not serve the WEC power capture as originally claimed by Korde [26,28].

The results of this study provide a formulaic method for the wave energy research community to establish the power capture upper bound for any WEC architecture along with the associated design insights (i.e. constraint equations) for approaching the bound. This work also establishes the importance of transforming a complex WEC architecture into the canonical form for enforcing resonant power capture conditions.

3.2 Article 2 — On establishing an analytical power capture limit for self-reacting point absorber wave energy converters based on dynamic response[13]

Having proposed a method for determining the analytical power capture upper bound for any WEC architecture in Article 1 of Section 3.1, attention is now placed on demonstrating this method by deriving this bound for a specific WEC architecture with a geometry controlled inertial modulation feature set.

It has been established that ocean wave energy conversion has yet to achieve economic viability when compared against alternative renewable sources such as solar photovoltaics or wind energy [7]. For wave energy to realize economic viability, the Cost of Energy (CoE) must be reduced by a factor of two. Such a drastic reduction cannot be realized solely from economics of scale and optimization of supply chain logistics. WEC device designs must be discovered that are capable of extracting more energy from ocean waves. To facilitate this process of discovery and ultimately design convergence, Weber introduced the Technology Performance Level (TPL) metric and emphasized its assessment early in a WEC development program to identify technologies with a strong predicted performance once in their commercial state. However, a robust assessment of TPL is challenging to determine at an early stage of a WEC development program. One method to define TPL at the conceptual stage is to assume a direct relationship of TPL with the "hydrodynamic wave power absorption" [8] potential of a WEC device. In doing so, the best possible TPL for a given WEC device is related to the power capture upper bound of that architecture. Such a TPL assessment is relative to the specific device configuration. To promote design convergence, an absolute analytical expression defining the power capture upper bound is preferred to facilitate comparisons of TPL across all configurations within an architecture. Such a process has been proposed in Article 1 [17] and the motivation of this article is to demonstrate this process using a SRPA WEC architecture with a variable inertial modulated spar in a case study. This case study targets establishing the power capture upper bound and the associated design insight required to achieve the upper bound, as well as implementing the design insight to formally introduce a new technology (i.e. the inerter) into the wave energy community.

A summary of the main contributions of this work follows:

3.2.1 Contribution 6 (CONT6)

Development and analysis of a frequency domain mathematical model using the mechanical circuit framework for the Derived SRPA WEC Architecture with an inertial modulation mechanism implemented internal to the spar.

> Upon proposing a mechanical circuit consistent with the Derived SRPA WEC Architecture, Thévenin’s theorem is applied to determine the canonical form. Once in canonical form Falnes’ mechanical impedance matching technique is applied to invoke complex-conjugate PTO force control resulting in a resonant state of the WEC at each frequency of the incoming wave excitation force. The relevance of this contribution to the wave energy community is the demonstration that Falnes’ impedance matching criteria may be invoked at the analytical level for more complex WEC architectures through applying the formulaic mechanical circuit framework. To my knowledge, this is the first

instance of an analytical model built for this complex WEC architecture using the mechanical circuit framework.

3.2.2 Contribution 7 (CONT7)

Proposed an analytical equation describing the power capture upper bound for the Derived SRPA WEC Architecture based on optimizing the geometric control variable (i.e. force source impedance).

The analytical upper bound is physically interpreted as the maximum power captured by the Derived SRPA WEC Architecture is equivalent to two single body point absorbers composed of the float and spar respectively, each independently operating under complex-conjugate PTO force control. WEC developers with devices based on this architecture may evaluate the power capture potential of their device by applying their design parameters into this equation. Such a calculation provides an absolute reference for WEC developers to compare their device performance. I believe this article to be the first to introduce this power capture upper bound.

3.2.3 Contribution 8 (CONT8)

Proposed an analytical constraint equation (i.e. design insight) relating the physical characteristics of various components in the Derived SRPA WEC Architecture, which must be enforced to achieve the power capture upper bound.

WEC developers with devices based on this architecture may use this constraint equation to evaluate the feasibility of implementing this design insight into their designs for optimizing the power capture potential of their device. I believe this article is the first to introduce this analytical constraint for achieving the power capture upper bound.

3.2.4 Contribution 9 (CONT9)

Mathematically established the inertial modulation regime proposed in this work has both the capability to decrease or increase the equivalent mass of the spar through intelligently modulating the force source reactance without requiring the removal or addition of physical mass.

This proof demonstrates the importance of inertial modulation schemes in the design of a geometry controlled SRPA WEC as an alternative to dynamic fluid ballasting technologies, which is energy intensive to pump fluid in/out of the spar tank, and changes the mean water level reference of the WEC.

3.2.5 Contribution 10 (CONT10)

Executed a numerical case study using hydrodynamics and inertial data from a previously published 1:25 scale model of a WaveBOB™ style SRPA [24] and validated the analytical equations proposed in this dissertation.

Analysis of the data (cf. Figure 8 [18]) demonstrates that the analytical expression of the power capture upper bound proposed in this work, along with the design insight in the form of a constraint equation is consistent with the numerical results generated using the hydrodynamics and inertial parameters from the SRPA configuration considered in this analysis (i.e. eq.(24) is consistent with eq.(3) with eq.(35) enforced [18]). Qualitative comparisons of the power capture upper bound against the capture width theoretical limit also exhibit consistency.

3.2.6 Contribution 11 (CONT11)

Demonstrated through numerical analysis that a significant power capture potential can still be realized even when enforcing displacement travel limits on the relative float to spar motion through modulating the PTO resistance.

> Although the power capture is significantly reduced when enforcing relative travel constraints, there is still a ten fold of power capture improvement observed in the numerical results over the baseline Original SRPA WEC Configuration at low wave excitation frequency. This power capture benefit should encourage WEC developers with devices based on this complex SRPA architecture to consider the control scheme proposed in this work.

3.2.7 Contribution 12 (CONT12)

Formally introduced inerters into the wave energy community as a geometry controllable technology capable of implementing the inertial modulation scheme proposed in this work.

> A feasible design configuration for an inerter subsystem capable of implementing optimal inertial modulation was proposed based on utilizing the design insight constraint equations derived in this work leading to achieving the power capture upper bound. Inerters are a proven technology having demonstrated significant performance improvements in the design of vehicle suspensions [47]. WEC developers should be exploring their use to widen the narrow bandwidth of operation of point absorbers.

3.2.8 Contribution 13 (CONT13)

Demonstrated that a significant power capture potential is still to be attained through implementing the design insights introduced in this work in comparison to data obtained from an existing SRPA WEC configuration published in literature.

> Experimental power capture data from the Original SRPA WEC Configuration operating under optimal amplitude control was qualitatively compared against numerical data generated from the Derived SRPA WEC Configuration operating at the upper bound demonstrating the potential for significant power capture improvement.

3.2.9 Contribution 14 (CONT14)

Proposed an analytical constraint equation (i.e. design insight) which eliminates relative travel between the float and spar and thus results in a null power capture scenario implemented entirely through geometry control.

> Ocean waves are a harsh environmental resource with the potential to damage SRPA devices when operating in storm conditions. As such, for WEC technology to gain market acceptance devices must be designed to survive storm conditions. This work introduces one such method for WEC developers to consider. I believe this article is the first to introduce this analytical constraint for achieving the null power capture condition while the PTO remains fully engaged in complex-conjugate control mode.

The results of this study not only introduce the successful application of the mechanical circuit framework to establish an analytical power capture upper bound for the Derived SRPA WEC Architecture, but numerically demonstrate using hydrodynamic parameters from a previously published physical SRPA model, how the upper bound can be achieved through the appropriate application of inerter technology. The goal of this work is to encourage WEC developers to evaluate both the power capture upper bound and the associated design insights for their architectures to explore both economic and design feasibility prior to locking into a design configuration and investing resources on computationally expensive non-linear time domain models and physical model testing.

3.3 Article 3 — On establishing generalized analytical phase control conditions in self-reacting point absorber wave energy converters[14]

For wave energy conversion to be an economical source of renewable energy, it is understood that step gains in power capture performance must be achieved [6]. However, increasing the power capture of a WEC device is often associated with increasing the device complexity. Article 2 in Section 3.2 demonstrated that the hydrodynamic power capture potential (i.e. the upper bound) of a WEC architecture can theoretically be achieved through simultaneous implementation of optimal geometry and optimal PTO force control via the master-slave relationship [17]. However, designing a WEC capable of approaching the upper bound may be prohibitive from both a design complexity and economical point of view. As such, there exists a balance between device power capture and design complexity. The goal of this work is to explore this complex balance. It is important to recognize that invoking resonance at each wave excitation frequency is a prerequisite to achieving the power capture upper bound [18]. As such, for an SBPA WEC with a given constant device geometry, the power capture is maximized when that device operates in resonance with the incoming wave excitation force. To achieve the objective of capturing more power from the wave resource, it is clear that invoking resonance is an important target for WEC design. This, however, yields the important questions: 1) What WEC topology would best serve our goal of maximizing power capture? 2) How should resonance be invoked? For the SBPA WEC architecture the former question is straightforward as there is only a single topological variant, however for more topologically complex WEC architectures such as the SRPA with multiple variants, the answer to this question is not clear.

Further complicating the argument, the concept of resonance is well defined for the heaving SBPA WEC architecture but not for more complex WEC architectures such as the SRPA. To bridge this gap Falnes [44] introduced and Bubbar et al. [17] later extended, the application of Thévenin's theorem to transform a complex WEC architecture into an equivalent SBPA (i.e. the canonical form). Once in canonical form, resonant conditions are then enforced. However, there is a catch. In transforming the complex WEC architecture into canonical form, parameters specific to the canonical form (i.e. the intrinsic impedance and equivalent excitation force) are now complicated functions of the physical parameters of the original complex WEC architecture. Hence, depending on the topology of the complex WEC architecture, there may exist multiple conditions for invoking resonance across the frequency spectrum, each with differing power capture characteristics.

In search for the required step gain in power capture potential, WEC developers are introducing more complex WEC designs to harness more of the available resource. There is, therefore, an acute need for a systematic method to both identify the analytical condition(s) for invoking resonance in complex WEC architectures, as well as exploring the conceptual design associated with the resonant states to determine which should be pursued further for potential commercial development. To fulfill this core need, the basis of this article is to introduce this process of identifying the analytical conditions for invoking resonance in the canonical form followed by implementing the process on an SRPA WEC configuration with an inertial modulation mechanism to explore the various topological variants and their resonance states in terms of power capture.

Through this work, I demonstrate how to generalize a geometry controlled feature set at the analytical level using a reactive force source. Design parameters are incorporated into this generalized representation, with numerical results detailing a target reactance profile used to propose a subsystem design incorporating an inerter device. In this work, the standard convention of implementing phase control via a reactive PTO is challenged in the SRPA architecture through a case study comparing the power capture potential of alternative topologies. The results of this study lead to proposing a preferred architecture for which the PTO is chosen to be a solely resistive device with the single function of capturing energy from the WEC, while the reactive geometry control feature set is implemented in the WEC spar.

A summary of the main contributions of this work follows:

3.3.1 Contribution 15 (CONT15)

Proposed a method to invoke resonance across the frequency spectrum based upon extending work previously published by Falnes.

> Falnes published an analytical constraint equation relating the intrinsic reactance of the canonical form to the natural frequency of the vibration system [12]. In this work, I propose that Falnes' constraint equation may be used to invoke resonance across the wave excitation frequency spectrum if a system

topology is selected for which a geometry control feature set capable of injecting a reactive force defined outside of the PTO boundary with the function of implementing the constraint equation. This method is generic and thus, all WEC development programs could implement the proposed method to determine the resonant conditions for their WEC devices at the conceptual design stage.

3.3.2 Contribution 16 (CONT16)

Successfully applied the proposed method on three different complex SRPA WEC architectures and identified analytical constraint equations for invoking resonance on each architecture.

This method first involves representing all three complex SRPA WEC architectures as mechanical circuits followed by systematically applying Thévenin's theorem to each architecture to determine their respective canonical form. Once in canonical form, Falnes constraint equation is enforced to identify the conditions on the geometric parameter (i.e. force source reactance) to invoke resonance of the respective complex SRPA WEC architecture. As these equations are generic in nature, any WEC development program represented by the complex SRPA WEC architecture proposed in this work could substitute design parameters into these equations to identify the optimal force source reactance to invoke the resonant conditions.

3.3.3 Contribution 17 (CONT17)

Executed a numerical case study using hydrodynamics and inertial data from a previously published 1:25 scale model of a WaveBOB™ style SRPA [24] to validate our analytical equations.

> Analysis of the data demonstrates: a) invoking the analytical constraint equations results in all the complex SRPA WEC configurations operating under resonant conditions based on their respective topology; b) the power capture performance varies significantly depending on the topology of the architecture and; c) Config5 based on Arch3, with a reactively tunable spar, exhibits a combination of a favourable power capture frequency response, along with a small float to spar relative displacement, rendering it the superior configuration.

3.3.4 Contribution 18 (CONT18)

Demonstrated how the mechanical circuit framework can be used to support technology innovation.

> In representing the topology of Arch3 via mechanical circuit, the geometry control parameter was intentionally signified as a generic force source reactance term interfaced between the spar and ground. This choice of avoiding a physical embodiment for the force source allowed for a generic mathematical representation of the optimal force source reactance to invoke resonance. Innovative subsystem designs are then proposed which, through substitution for the force source reactance with a feasible topology of linear mechanical components, implement the constraint equation. Several possible subsystems are proposed in this work, however an inertial modulation mechanism utilizing a reaction mass and semi-active inerter is chosen for further analysis. Using

> feasible design parameters for the inertial modulation mechanism, it is demonstrated that resonant conditions can be implemented for the majority of the wave excitation frequency band.

3.3.5 Contribution 19 (CONT19)

Demonstrated through comparison of numerical data from this work with previously published experimental data from the same WEC configuration, that a vast improvement in power capture potential is possible while implementing the resonant control method introduced in *Arch3*.

> Although the resonant control method introduced in Arch3 yields an order of a magnitude lower power capture then the upper bound published by Bubbar and Buckham [18], the control strategy is less complex and presumably less costly to develop. This result suggests that WEC developers should evaluate both the control schemes introduced in Article 2 and Article 3 to determine which power capture to design complexity is best suited for their development program.

The results of this study introduce a technique for WEC developers to explore alternative methods to implement resonant control at the conceptual stage of a WEC development program. In addition, through utilizing generic force sources in conjunction with the mechanical circuit framework, this work has introduced a new method to expose new technology innovations through establishing technical requirements on the force sources that must be replaced by some combination of mechanical components. The outcome of this work demonstrates how WEC topology selection has a strong influence on power capture potential, encouraging WEC developers to evaluate all the topological variants for resonant control at the conceptual design stage prior to investing resources on computationally expensive non-linear time domain models and physical model testing.

3.4 Mapping Objectives to Contributions

The following section highlights the relationships of the contributions (CONT) introduced in Section 3 to the research objectives (OBJ) identified in Section 1.6.

Table III: Linkages between Objectives (OBJ) and Contributions (CONT)

	OBJ1	**OBJ2**	**OBJ3**	**OBJ4**	**OBJ5**	**OBJ6**	**OBJ7**	**OBJ8**
CONT1	X	X						
CONT2	X	X						
CONT3	X	X						
CONT4	X							
CONT5			X	X				
CONT6								
CONT7	X	X	X					
CONT8		X		X				
CONT9				X	X			
CONT10				X				
CONT11				X				
CONT12				X	X	X		
CONT13				X				
CONT14								X
CONT15							X	
CONT16			X	X			X	
CONT17				X			X	
CONT18					X	X		
CONT19			X					

4 Limitations and Future Work:

Through application of the mechanical circuit framework, this dissertation has introduced a new method of determining the analytical power capture upper bound of a wave energy converter for WEC architectures. Despite the utility of the proposed method, there exists limitations detailed in Section 4.1. Moreover, this process has surfaced several interesting questions for further exploration. Three areas of future exploration are detailed below in Sections 4.2-4.4.

4.1 Limitations of the Mechanical Circuit Framework

With any framework that models the true physics of a system there exists limitations to the techniques presented. In this dissertation, the mechanical circuit framework is applied to the design of wave energy converter devices to extend the mechanical impedance matching technique originally presented by Falnes in the frequency domain [12]. As such, this framework is subject to the same limitations of frequency domain models. These limitations include: 1) Linearized hydrodynamics – development of the frequency domain model requires a linearized representation of the hydrodynamic forces as specified in Section 1.4.2; 2) Steady state analysis – the model assumes the system is operating under steady state conditions as specified in Section 1.4; 3) Monochromatic wave regime – the model assumes waves incident upon the WEC are represented by a single frequency only; 4) PTO load is limited to capturing power in a single Degree of Freedom (DoF) only – each DoF in the system must be represented via an independent mechanical circuit. Multiple DoFs may be represented in a single model through coupling the mechanical circuits via transducer elements [48], however in order to apply impedance matching conditions to maximize power capture at the PTO, the PTO must be limited to a single DoF.

4.2 Expansion of Null Power Capture Using Geometry Control

CONT14 in Section 3.2.9 proposes an analytical constraint equation, which results in a null power capture condition of the Derived SRPA WEC Architecture. This kinematic state is achieved as the relative travel between the float and spar is eliminated leading to both bodies moving in unison. This condition is enabled through geometry control alone, while the PTO is still technically engaged, by selecting a spar impedance that matches the float resulting in the exact same dynamic response to the external wave excitation force. Such a method is novel and could be beneficial control strategy for WEC devices operating in storm conditions.

4.3 Time Domain Modeling of the Master-Slave Relationship

This dissertation successfully developed and numerically validated a method to implement optimal geometry control and optimal PTO force control to maximize the power capture of a WEC device in the frequency domain. Where the frequency domain can supply developers with insights at the early stages of the development program, further feasibility analysis needs to be performed in the time domain to include both non-linear effects as well as model the true wave elevation time series of the ocean wave resource before investment is placed to fabricate experimental models. The nature of representing a complex WEC architecture as a canonical form allows for the application of control strategies already published in wave energy literature on SBPAs. For example Figure 10 below is an adapted block diagram of a control strategy originally proposed by Falnes (cf. Figure 6.9 [12]), but updated to include a canonical form representation of a generic complex WEC architecture with a geometry control feature set represented by the parameter Λ. A time-domain model for an SRPA without a geometry controllable feature set has been implemented by Olaya et al. [49] and is an excellent starting point for consideration in developing the control strategy outlined in Figure 10.

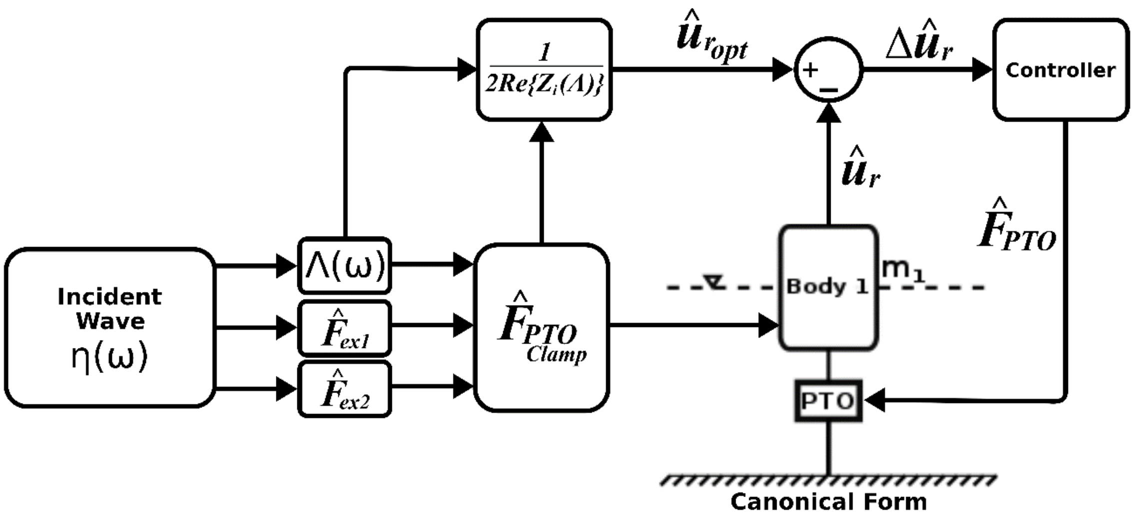

Figure 10: Control Block Diagram for an SBPA in Canonical Form Adapted from Falnes [12]

4.4 Experimental Testing of a Physical WEC Model Utilizing an Inerter

Finally, the analytical and numerical analysis in this dissertation have demonstrated results which suggest a vast improvement in power capture is possible through the implementation of an inerter subsystem internal to the spar. The next logical step is to validate the predicted performance through fabricating and testing a scaled model in a controlled wave tank. Such a model would support both the validation of the frequency domain results presented in this dissertation, along with providing a platform for testing future control strategies developed in the time domain as per Section 4.3.

5 Bibliography

[1] J. Cruz, ed., Ocean wave energy: current status and future prepectives [i.e. perspectives], Springer, Berlin, 2008.

[2] J. Falnes, A review of wave-energy extraction, Mar. Struct. 20 (2007) 185–201. doi:10.1016/j.marstruc.2007.09.001.

[3] J.V. Ringwood, G. Bacelli, F. Fusco, Energy-Maximizing Control of Wave-Energy Converters: The Development of Control System Technology to Optimize Their Operation, IEEE Control Syst. 34 (2014) 30–55. doi:10.1109/MCS.2014.2333253.

[4] G. Reikard, B. Robertson, J.-R. Bidlot, Combining wave energy with wind and solar: Short-term forecasting, Renew. Energy. 81 (2015) 442–456. doi:10.1016/j.renene.2015.03.032.

[5] S. Astariz, G. Iglesias, The economics of wave energy: A review, Renew. Sustain. Energy Rev. 45 (2015) 397–408. doi:10.1016/j.rser.2015.01.061.

[6] A. Babarit, Ocean Wave Energy Conversion: Resource, Technologies and Performance, Elsevier, 2017.

[7] J. Weber, WEC Technology Readiness and Performance Matrix–finding the best research technology development trajectory, in: Int. Conf. Ocean Energy, 2012.

[8] J. Weber, R. Costello, J. Ringwood, WEC technology performance levels (TPLs)-metric for successful development of economic WEC technology., in: Proc. EWTEC 2013, 2013.

[9] B.S. Blanchard, W.J. Fabrycky, W.J. Fabrycky, Systems engineering and analysis, Prentice Hall Englewood Cliffs, NJ, 1990.

[10] L.H. Holthuijsen, Waves in oceanic and coastal waters, Cambridge University Press, Cambridge, 2007. http://public.eblib.com/choice/publicfullrecord.aspx?p=288506 (accessed December 22, 2015).

[11] A. Babarit, A database of capture width ratio of wave energy converters, Renew. Energy. 80 (2015) 610–628. doi:10.1016/j.renene.2015.02.049.

[12] J. Falnes, Ocean waves and oscillating systems: linear interactions including wave-energy extraction, Cambridge University Press, Cambridge ; New York, 2002.

[13] S. Beatty, Self-Reacting Point Absorber Wave Energy Convertors, University of Victoria, 2015.

[14] A.P.L. Merigaud, J.V. Ringwood, A non-linear frequency-domain approach for numerical simulation of wave energy converters, IEEE Trans. Sustain. Energy. PP (2017) 1–1. doi:10.1109/TSTE.2017.2716826.

[15] C.M. Harris, C.E. Crede, H.M. Trent, Shock and Vibration Handbook Vol I, 1st ed., 1962. http://adsabs.harvard.edu/abs/1962PhT....15i..65H (accessed December 23, 2015).

[16] M.C. Smith, Synthesis of mechanical networks: the inerter, IEEE Trans. Autom. Control. 47 (2002) 1648–1662. doi:10.1109/TAC.2002.803532.

[17] K. Bubbar, B. Buckham, P. Wild, A method for comparing wave energy converter conceptual designs based on potential power capture, Renew. Energy. 115 (2018) 797–807. doi:10.1016/j.renene.2017.09.005.

[18] K. Bubbar, B. Buckham, On establishing an analytical power capture limit for self-reacting point absorber wave energy converters based on dynamic response, Appl. Energy. 228 (2018) 324–338. doi:10.1016/j.apenergy.2018.06.099.
[19] L. Thévenin, Extension de la loi d'Ohm aux circuits électromoteurs complexes [Extension of Ohm's law to complex electromotive circuits], in: Ann. Télégraphiques, 1883: pp. 222–224.
[20] J.N. Newman, Marine Hydrodynamics, MIT Press, 1977.
[21] M. Folley, Numerical modelling of wave energy converters: state-of-the-art techniques for single wec and converter arrays, 1st edition, Elsevier, Cambridge, MA, 2016.
[22] U.A. Korde, J. Ringwood, Hydrodynamic Control of Wave Energy Devices, Cambridge University Press, 2016. https://books.google.ca/books?hl=en&lr=&id=VcfxDAAAQBAJ&oi=fnd&pg=PR9&dq=Hydrodynamic+Control+of+Wave+Energy+Devices&ots=EMczOOvLIe&sig=lmUMP_tm_47nJBUdJPmlOcHbzQk (accessed October 18, 2016).
[23] S.J. Beatty, P. Wild, B.J. Buckham, Integration of a wave energy converter into the electricity supply of a remote Alaskan island, Renew. Energy. 35 (2010) 1203–1213.
[24] S.J. Beatty, M. Hall, B.J. Buckham, P. Wild, B. Bocking, Experimental and numerical comparisons of self-reacting point absorber wave energy converters in regular waves, Ocean Eng. 104 (2015) 370–386.
[25] J. Davidson, J.V. Ringwood, Mathematical Modelling of Mooring Systems for Wave Energy Converters—A Review, Energies. 10 (2017) 666. doi:10.3390/en10050666.
[26] U.A. Korde, On providing a reaction for efficient wave energy absorption by floating devices, Appl. Ocean Res. 21 (1999) 235–248.
[27] U.A. Korde, On Controlled Oscillating Bodies With Submerged Reaction Mass, in: OMAE 2003-37012, Cancun, Mexico, 2003: pp. 405–411. doi:10.1115/OMAE2003-37012.
[28] U.A. Korde, Systems of reactively loaded coupled oscillating bodies in wave energy conversion, Appl. Ocean Res. 25 (2003) 79–91. doi:10.1016/S0141-1187(03)00044-0.
[29] J. Hals, Modelling and phase control of wave-energy converters, Norwegian University of Science and Technology, 2010.
[30] A.F. de O. Falcão, Phase control through load control of oscillating-body wave energy converters with hydraulic PTO system, Ocean Eng. 35 (2008) 358–366. doi:10.1016/j.oceaneng.2007.10.005.
[31] R.G. Coe, G. Bacelli, D.G. Wilson, O. Abdelkhalik, U.A. Korde, R.D. Robinett III, A comparison of control strategies for wave energy converters, Int. J. Mar. Energy. (2017). doi:10.1016/j.ijome.2017.11.001.
[32] C.C. Mei, Power extraction from water waves, J. Ship Res. 20 (1976) 63–66.
[33] J.N. Newman, The interaction of stationary vessels with regular waves, in: Proc. 11th Symp. Nav. Hydrodyn. Lond., 1976: pp. 491–501.
[34] D.V. Evans, A theory for wave-power absorption by oscillating bodies, J. Fluid Mech. 77 (1976) 1–25. doi:10.1017/S0022112076001109.
[35] C.A. Desoer, E.S. Kuh, Basic circuit theory, Tata McGraw-Hill Education, 2009.

[36] C. Liang, J. Ai, L. Zuo, A Self-Reacting Point Absorber With a Novel Mechanical Motion Rectifier as Power Takeoff System, (2014) V002T32A004. doi:10.1115/DSCC2014-6292.
[37] W. Li, K.T. Chau, C.H.T. Lee, T.W. Ching, M. Chen, J.Z. Jiang, A new linear magnetic gear with adjustable gear ratios and its application for direct-drive wave energy extraction, Renew. Energy. 105 (2017) 199–208. doi:10.1016/j.renene.2016.12.026.
[38] A. Babarit, A.H. Clément, Optimal latching control of a wave energy device in regular and irregular waves, Appl. Ocean Res. 28 (2006) 77–91. doi:10.1016/j.apor.2006.05.002.
[39] A.A.E. Price, C.J. Dent, A.R. Wallace, On the capture width of wave energy converters, Appl. Ocean Res. 31 (2009) 251–259. doi:10.1016/j.apor.2010.04.001.
[40] K. Budal, J. Falnes, A resonant point absorber of ocean-wave power, Nature. 256 (1975) 478–479.
[41] K. Budal, J. Falnes, Interacting point absorbers with controlled motion, Power Sea Waves. (1980) 381–399.
[42] J. Falnes, Small is beautiful: How to make wave energy economic, in: 1993 Eur. Wave Energy Symp. Edinb. Scotl., 1994: pp. 367–372.
[43] J.H. Todalshaug, Practical limits to the power that can be captured from ocean waves by oscillating bodies, Int. J. Mar. Energy. 3–4 (2013) e70–e81. doi:10.1016/j.ijome.2013.11.012.
[44] J. Falnes, Wave-Energy Conversion Through Relative Motion Between Two Single-Mode Oscillating Bodies, J. Offshore Mech. Arct. Eng. 121 (1999) 32–38. doi:10.1115/1.2829552.
[45] A. Babarit, J. Hals, M.J. Muliawan, A. Kurniawan, T. Moan, J. Krokstad, Numerical benchmarking study of a selection of wave energy converters, Renew. Energy. 41 (2012) 44–63. doi:10.1016/j.renene.2011.10.002.
[46] R. Alcorn, D. O'Sullivan, Institution of Engineering and Technology, eds., Electrical design for ocean wave and tidal energy systems, Institution of Engineering and Technology, Stevenage, U.K, 2013.
[47] M.Z.Q. Chen, C. Papageorgiou, F. Scheibe, F. Wang, M.C. Smith, The missing mechanical circuit element, IEEE Circuits Syst. Mag. 9 (2009) 10–26. doi:10.1109/MCAS.2008.931738.
[48] D. Rowell, D.N. Wormley, System dynamics: an introduction, Prentice Hall, 1997.
[49] S. Olaya, J.-M. Bourgeot, M. Benbouzid, Optimal control for a self-reacting point absorber: A one-body equivalent model approach, in: Electron. Appl. Conf. Expo. PEAC 2014 Int., IEEE, 2014: pp. 332–337. http://ieeexplore.ieee.org/xpls/abs_all.jsp?arnumber=7037877 (accessed December 23, 2015).

6 Appendix A: A method for comparing wave energy converter conceptual designs based on potential power capture

K. Bubbar, B. Buckham, P. Wild, A method for comparing wave energy converter conceptual designs based on potential power capture, Renewable Energy. 115 (2018) 797–807. doi:10.1016/j.renene.2017.09.005.

Renewable Energy 115 (2018) 797–807

Contents lists available at ScienceDirect

Renewable Energy

journal homepage: www.elsevier.com/locate/renene

A method for comparing wave energy converter conceptual designs based on potential power capture

K. Bubbar*, B. Buckham, P. Wild

Department of Mechanical Engineering, West Coast Wave Initiative, Institute for Integrated Energy Systems, University of Victoria, 3800 Finnerty Rd, Victoria, B.C., V8W 3P6, Canada

ARTICLE INFO

Article history:
Received 16 March 2017
Received in revised form
11 July 2017
Accepted 3 September 2017
Available online 6 September 2017

Keywords:
Optimal power capture
Impedance matching
Thévenin's theorem
Optimal PTO force control
Mechanical circuits
Geometry control
Design convergence
WEC canonical form

ABSTRACT

The design space for ocean wave energy converters is notable for its divergence. To facilitate convergence, and thereby support commercialization, we present a new simple method for analysis and comparison of alternative device architectures at an early stage of the design process. Using Thévenin's theorem, Falnes crafted an ingenious solution for the monochromatic optimal power capture of heaving point absorber devices by forming a mechanical impedance matching problem between the device and the power take-off. However, his solutions are limited by device architecture complexity. In this paper, we use the mechanical circuit framework to extend Falnes' method to form and solve the impedance matching problem and calculate the optimal power capture for converter architectures of arbitrary complexity. The new technique is first applied to reprove Falnes' findings and then to assess a complex converter architecture, proposed by Korde. This work also provides insight into a master-slave relationship between the geometry and power take-off force control problems that are inherent to converter design, and it reveals a hierarchy of distinct design objectives unbeknownst to Korde for his device. Finally, we show how application of the master-slave principle leads to the reduction in the dimensionality of the associated design space.

1. Background

Ocean waves are a vast, high-density renewable energy resource. The IEA estimates annual global wave energy potential of 29,500 TWh [1], which represents approximately 150% of annual global electricity demand [2]. In spite of this tremendous potential, there is currently no commercial deployment of a Wave Energy Converter (WEC) and, as is typical of a pre-commercial sector, proposed WEC conceptual designs vary widely [3–5]. This divergent design space exists, in part, due to the absence of an adequate method for comparing the power capture potential of WEC *architectures* at an early stage of the design process. In the absence of such a comparative method, increasingly complex WEC designs are endlessly proposed which may not necessitate improved performance, thus dispersing focus and slowing collective progress. Current numerical modelling approaches are based on an assumed device *configuration* [6]. Results, therefore, cannot be extrapolated beyond that *configuration* precluding determination of an optimal solution from a design space that includes alternative *configurations*.

To promote rapid design convergence and stimulate commercial adoption, we propose a concise method founded in the fundamental principles of vibration theory, capable of assessing the power capture potential of any WEC *architecture*, regardless of complexity, and thus enabling WEC designers to identify promising concepts early in the development process. Our method uses a frequency domain methodology, which converts any linearized representation of a resonant WEC of a particular *class* into an equivalent and fundamental *architecture*, or *canonical form*, for comparison on an *apples-to-apples* basis. Operating within the confines of linear monochromatic theory, results can be compared across WEC device *classes*. The method analytically determines the linearized power capture ceiling ($P_{U_{Max}}|_{opt}$) for a given *architecture* and may be used as performance assessment criterion for coarsely estimating the Technology Performance Level (TPL) early in the conceptual design phase as recommended by Weber [3].

To frame our objective, we define a hierarchy to organize WEC designs comprising: *configuration*, *architecture*, and *class*. A *configuration* is a design defined by a set of physical parameters

* Corresponding author.
E-mail address: kbubbar@uvic.ca (K. Bubbar).

http://dx.doi.org/10.1016/j.renene.2017.09.005
0960-1481/

governing the system characteristics (e.g. WaveBOB™). An *architecture* is the set of *configurations*, which share the same device topology; for example, the Self-Reacting Point Absorber (SRPA) with the PTO load connected between two wave activated heaving bodies. A *class* comprises of all *architectures* which operate on the same physical principle (e.g. point absorbers, attenuators, terminators) [4,5]. To exemplify these definitions, the single body point absorber [7], SRPA [8], and Korde's WEC [9], shown in Fig. 1, all belong to the point absorber *class*, but represent distinct *architectures*. In addition, PowerBuoy™ and WaveBOB™ represent the same *architecture*, but possess different *configurations* and performances [10].

Through this hierarchical structure, the complexity of the *architecture* grows with the number of components in the embodied design. It is in part, the growth of components in modern WEC designs, as illustrated in Fig. 1, which is driving the divergence of the design space. There is thus an important choice of which *architecture* is most appropriate to the local environmental conditions of the design problem. The following section clarifies *architecture* complexity by classifying the parameters, which influence the various stages of the energy conversion process, to establish why the number of components is increasing in contemporary designs, and how this growth influences the overall power capture optimization problem.

1.1. Geometry control and WEC complexity

To illustrate the divergence of the conceptual design space, an overview of features common to emerging WEC designs, and discussion of how these design features influence the energy conversion pathway, is needed.

Wave energy conversion comprises the transmission of power: 1) from the ocean wave; 2) onto the device bodies; 3) into the device Power Take-Off (PTO). Each stage in the energy conversion process is governed by a set of physical parameters that influences the overall conversion efficiency [5,11].

Wave excitation forces do work on the WEC wetted hull(s) resulting in body motion and thus transmit power to the device. The body inertial and hydrodynamics properties, manifestations of the bodies' geometries, influence this conversion process. Providing a means to vary these geometric parameters during WEC operation leads to the possibility of increasing the power producing bandwidth of the system at the expense of a more complex system *architecture*. WEC complexity can, thus, arise as a physical manifestation of the geometric parameters. Price defined 'geometry control' as active variation of parameters that alter the intrinsic impedance or wave excitation forces in a WEC system [12]. A growing number of WEC designs are introduced into the wave energy community, which propose various features enacting geometry control, while further diluting the design space. For example, WaveSpring™ is a technology capable of varying the buoyancy stiffness, and thus, the natural frequency of a floating body, leading to an increase in the power transmitted between the ocean wave and WEC system [13].

To capture power in the PTO, the WEC body motion works against a PTO reaction force. For a linearized system, this force is usually modelled as a viscous dashpot. It is advantageous to manipulate the system into resonance to maximize power capture. This is achieved by shaping the PTO force response using the well-established optimal PTO amplitude and phase control conditions [14]. Optimal phase control ensures the body velocity is in phase with the incoming excitation force and may be achieved outside of the system natural frequency, through injection of reactive power via the PTO reaction force [14].

As these two stages in the energy conversion processes are linked serially, the PTO force control is inherently influenced by the upstream geometry control establishing a two tier power capture optimization problem. This problem is described as selecting the optimal: 1) geometry to maximize the power transferred from the ocean resulting in body motion; 2) PTO reaction force to maximize the power captured by the PTO subject to the optimal geometry control condition.

To isolate the influence of the geometric parameters on power capture, the WEC must always operate under optimal PTO force control, leading to a master-slave relationship in which the PTO force parameters (slave) follow the geometric parameters (master). Therefore, as the complexity of WEC designs enacting geometry control grows, so does the complexity of the associated master-slave relationship.

1.2. Power capture

To achieve our goal of conceptual design convergence, a unified approach to analytically optimize the power production potential for an *architecture* is key. In doing so, we use the following terms P_U, $P_{U_{Max}}$, and $P_{U_{Max}}|_{opt}$ to clarify the monochromatic time-average power capture in terms of our hierarchy. Each term is respectively defined as the power captured for a WEC *architecture* subject to: no constraints on the PTO and geometric parameters (P_U); constraints enforcing only optimal PTO parameters ($P_{U_{Max}}$); and constraints enforcing both optimal geometric and PTO parameters ($P_{U_{Max}}|_{opt}$). In the literature, $P_{U_{Max}}$ (or more frequently capture width [14]) is often reported and determined through execution of various numerical or experimental methods using an assumed *configuration* [4]. As *architectural* complexity grows, so does the number of design parameters. For numerical models of complex WEC *configurations*, parameter values are assumed to simplify optimization efforts, inhibiting comparisons across all *configurations* within an *architecture*. Hence, an analytical method impartial

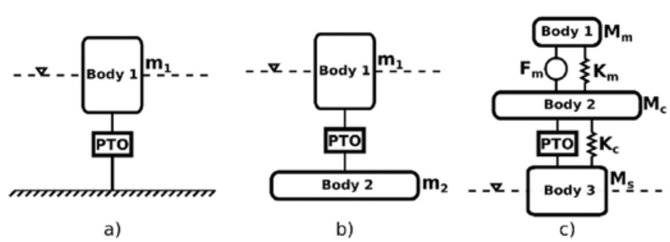

Fig. 1. WEC architectures of growing complexity in the point absorber class. a) Single-body; b) Self-Reacting Point Absorber; c) Korde's WEC [9].

to design complexity is preferred.

To promote convergence, we propose generating expressions of $P_{U_{Max}}|_{opt}$ for *architectures* and mining this expression for the optimal geometric conditions, instead of directly numerically calculating $P_{U_{Max}}$ for *configurations*. To determine the optimal *architecture* for power capture, we must: 1) determine an expression for $P_{U_{Max}}$ that is valid across the *architecture*, and that robustly enforces the master-slave relationship, 2) optimize $P_{U_{Max}}$ via the geometric parameters, leading to $P_{U_{Max}}|_{opt}$. To accomplish the former, we turn to Falnes for guidance.

Informed by electronic circuit theory, Falnes' morphed the linear power capture optimization problem for a single body point absorber (40) into an equivalent analytical mechanical impedance matching problem between the WEC and the PTO; optimal PTO power capture is realized when the PTO impedance is matched with the intrinsic impedance of the remaining system. This *elegant rule*, known as optimal PTO force control, is described by (1) and (2) for either Complex Conjugate (CC) or Amplitude Control (AC) regimes respectively, and can be used to define the optimal PTO parameters based on the system geometric parameters [14]. By applying the equality constraint, represented in (1) or (2), the required master-slave relationship is enforced for their respective regime, thereby reducing the dimensionality of the power capture optimization space solely to geometric parameters. With this new problem formulation, the challenge is to isolate and determine the intrinsic impedance (Z_i) of the WEC device.

$$Z_{PTO_{opt(CC)}} = Z_i^* \tag{1}$$

$$Z_{PTO_{opt(AC)}} = \left|Z_i\right| \tag{2}$$

For the single body point absorber *architecture*, Z_i can be isolated directly and used to calculate $P_{U_{Max}}$, as shown in (3) or (4) in both complex conjugate or amplitude control regimes respectively [14]. In this expression, $\widehat{F}_D$ represents the complex phasor for the wave excitation force. This result is profound for the wave energy community as it reveals an analytical power capture expression for the single body point absorber *architecture* subject to optimal PTO force control, which can be computed without knowledge of the system kinematics (i.e. complex body velocity). Further optimization of the power capture via the geometric parameters can be performed on these expressions to reveal $P_{U_{Max}}|_{opt}$ for this *architecture*.

$$P_{U_{Max(CC)}} = \frac{\left|\widehat{F}_D\right|^2}{8\Re e\{Z_i\}} \tag{3}$$

$$P_{U_{Max(AC)}} = \frac{\left|\widehat{F}_D\right|^2}{4[\Re e\{Z_i\} + |Z_i|]} \tag{4}$$

1.3. Phenomenological equivalent mechanical systems

Within the point absorber *class*, the limitation of a bottom fixed reference led to the evolution of the SRPA *architecture* [8] for which an analytical solution to $P_{U_{Max}}$ was required. However, application of the mechanical impedance matching method on the SRPA required isolation of the intrinsic impedance. Falnes recognized that the SRPA *architecture* could be creatively manipulated into an equivalent *architecture* through application of circuit equivalency theorems [15]. In particular, employing Thévenin's theorem [16] across the PTO, Falnes transformed the SRPA into an equivalent single body point absorber *architecture* excited by an equivalent excitation force ($\widehat{F}_{PTO_{Clamp}}$), and driven at the relative velocity ($\widehat{u}_r$) realized across the PTO of the original SRPA [17]. This simplification isolates the equivalent single body intrinsic impedance (Z_i) of the WEC from the PTO and permits the evaluation of $P_{U_{Max}}$ for the SRPA *architecture* by substituting the derived Z_i and $\widehat{F}_{PTO_{Clamp}}$ into (3) or (4).

It remains unclear how Falnes' *elegant rule* is extended to support current and emerging WEC designs which include additional mechanical bodies [18] and components [13], external force actuators [9], and variable wetted hull geometry [19].

There is, therefore, a need to extend Falnes' work to expose how his methodology can be used to analytically determine $P_{U_{Max}}$ for *architectures* of greater complexity, with the goal of determining where development efforts should be focused in order to identify optimal designs. Here, we use the mechanical circuit framework, Fig. 2, to develop this extension to Falnes' work, and we seek to introduce this framework into the wave energy community.

1.4. Mechanical circuits for extending phenomenological equivalence

Falnes' applied Thévenin's theorem to the SRPA *architecture* based on physical argument, but hinted at employing his results to more complex *architectures*, without revealing implementation details [17]. Mechanical circuits are a topological representation of a mechanical system capable of modelling the dynamics of an infinitely complex *architecture*. Linear systems are constructed from standard mechanical elements, characterized as impedances that act as the transfer functions between complex velocities and forces applied at reference points in the system [15] [20], (see Appendix B). Within the framework, a standard set of methods to simplify the *architecture* are available via both Kirchhoff's conservation laws, and equivalent circuit theorems already familiar to electrical engineers [15,21].

This framework presents the mechanical system designer with the ability to model more complex system *architectures* while allowing for methodical application of Thévenin's theorem to extract the equivalent: 1) single body intrinsic impedance, Z_i and 2) excitation force of the system, $\widehat{F}_{PTO_{Clamp}}$. As such the impedance matching problem may be formed, as shown in (1) and (2), leading to the desired extension of Falnes' *elegant rule* to infinitely complex WEC *architectures* [15].

In this paper, we introduce the salient features of the mechanical circuit framework that underpin the mechanical impedance matching problem, and then demonstrate how the mechanical circuit framework is implemented to methodically solve for Z_i, $\widehat{F}_{PTO_{Clamp}}$, and $P_{U_{Max}}$ for three different point absorber *architectures* of growing complexity. The three architectures considered are: 1) Falnes SRPA, for which we rederive Falnes' seminal work as a basis to validate the technique; 2) SRPA with coupled friction in parallel with the PTO which exposes a counterintuitive but physically important result on optimal PTO force control; 3) complex WEC *architecture* proposed by Korde [9], which uses a geometry controlled reactive force compensator, and we reveal new significant insight into the operation of this device.

2. Theory

Circuit methodologies originate from network theory in which physical systems are described in topological form as edges connected between nodes [22,23]. Mathematical representation comes by means of associating constitutive equations expressing the physics for each edge. Circuits in which the substitution,

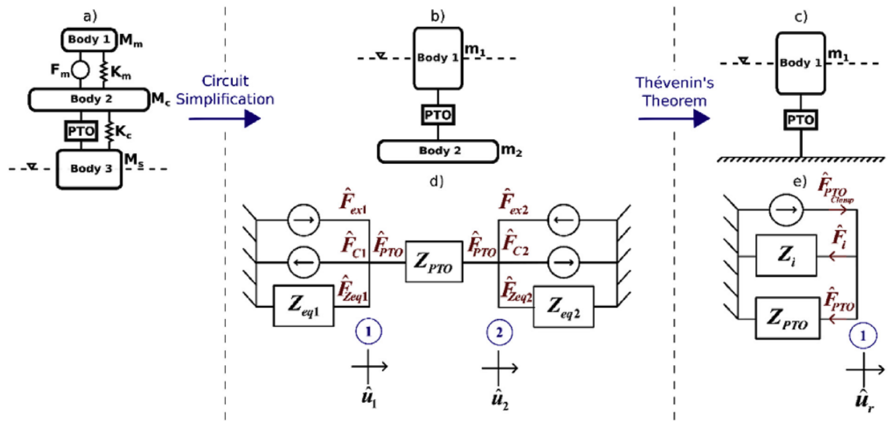

Fig. 2. Process of Generating a Phenomenological Equivalent System. a) Korde's WEC [9]; b) Falnes' SRPA WEC [17]; c) Single Body WEC [7]. d) SRPA Mechanical Circuit; e) Single Body WEC Mechanical Circuit.

superposition, and the reciprocity theorems hold are categorized as linear, satisfy the uniqueness criteria, and are suitable for simplification through application of Thévenin or Norton's theorems [15].

Application of the impedance matching principle first requires the representation of a physical system as a mechanical circuit. Accordingly, one method requires recognizing that Newton's Second Law in D'Alembert form can be expressed as a restatement of Kirchhoff's Node law with the orientation of the forces into and out of a node mathematically described by (5) [15].

$$\sum_i F_{in_i} = \sum_j F_{out_j} \tag{5}$$

Through analysis of a free body diagram, the forces on each body are represented as forces either entering or leaving each velocity node, as described in Appendix A. Frequency domain modelling of WEC systems assumes time-invariance of the system parameters for each wave frequency considered. Hence, the forces are converted to impedance format through application of the Fourier Transform on the time domain constitutive equations and standard linear mechanical elements are then placed between the velocity nodes.

It is standard practice to model surface wave hydrodynamic forces as linear functions of a body's position, velocity and acceleration with frequency dependent coefficients [24]. Such models lend naturally to representation as circuit elements [14]. Buoyancy, added mass and radiation damping effects are interpreted as linear spring, mass, and damper elements respectively. Wave excitation and coupled radiation forces are modelled as force sources as they are portrayed as external forces in the Newtonian free body diagram. The standard mechanical circuit elements and their constitutive impedance relations are listed in Table 1 of Appendix B. Mass elements require a single node connection to ground in order to satisfy Newton's 2nd Law as noted by the dashed line [15].

The PTO is the internal load responsible for harvesting energy and is signified as the Generic Mechanical Impedance element listed in Appendix B. Circuit simplification is completed through application of series and parallel circuit laws [15] to combine the mechanical impedance elements. However, the PTO element is always kept separate.

Thévenin's theorem is applied to the simplified circuit at the nodes of the PTO by solving for two physical characteristics of the dynamic system: 1) the relative velocity across the PTO when the PTO is removed ($\hat{u}_{r_{Free}}$), and 2) the force transmitted through the PTO when the PTO is locked ($\hat{F}_{PTO_{Clamp}}$). The equivalent phenomenological single body intrinsic impedance is then calculated as $Z_i = \hat{F}_{PTO_{Clamp}}/\hat{u}_{r_{Free}}$ with the equivalent excitation force equal to $\hat{F}_{PTO_{Clamp}}$ [15]. The mechanical circuit representation of the Thévenin equivalent circuit is $\hat{F}_{PTO_{Clamp}}$ in parallel with both Z_i and Z_{PTO} as seen in Fig. 2e and is consistent with the Shock and Vibration community [15]. This representation is in contrast to the Thévenin equivalent circuit layouts currently published in the wave energy community, for which Z_i and Z_{PTO} are series connected with velocity defined as the through variable [6,25–27]. We will show the validity of our claim in Section 4.1.

The mechanical circuit framework, combined with application of Thévenin's theorem transforms a complex WEC *architecture*, as shown in Fig. 2a, into an equivalent single body WEC *architecture* as in Fig. 2c. It can be concluded that Falnes' solution of $P_{U_{Max}}$ for the single body *architecture* is generic since all *architectures* can be reduced to this *canonical form*. In this generalization, the mechanical circuit framework plays the important role of determining both Z_i and $\hat{F}_{PTO_{Clamp}}$ in WEC *architectures* of growing complexity. Once the circuit is formed, arriving at this conclusion is the consequence of rote application of well-established concepts.

In Section 3, the mechanical circuit framework is applied to determine both Z_i and $\hat{F}_{PTO_{Clamp}}$ for WEC *architectures* of increasing complexity. Section 4 uses these expressions of Z_i and $\hat{F}_{PTO_{Clamp}}$ to determine $P_{U_{Max}}$ and to perform further analyses to reveal operating principles of these devices.

3. Methods

In this section we explore the potential of the mechanical circuit technique by progressively modelling more complex WEC *architectures* and determining the expressions for Z_i and $\widehat{F}_{PTO_{Clamp}}$ as a precursor to the power analyses of Section 4. We start with a rederivation of Falnes' result for the intrinsic impedance of a heaving SRPA device. The SRPA system topology is then perturbed through addition of a new damper element representing linear viscous friction in parallel with the PTO. A perturbed intrinsic impedance is calculated, and the physical consequence to power capture is discussed in Section 4.2. Finally, we employ the mechanical circuit technique to model and determine both Z_i and $\widehat{F}_{PTO_{Clamp}}$ for a complex WEC *architecture* in Korde's reaction mass, force compensated device. This leads to a significant new result, an analytical expression for the intrinsic impedance for this *architecture*, for which important insight is developed in the power analysis of Section 4.3.

3.1. Rederivation of optimal PTO force conditions for Falnes' SRPA

We begin by reproducing Falnes' result (20) for SRPA devices. The linear Newtonian dynamics are procedurally converted into a mechanical circuit through identification of the force components entering and leaving each velocity node followed by mechanical component placement between the nodes. The resulting mechanical circuit is represented by Fig. 3a.

Application of the parallel circuit law on Fig. 3a then compresses the mechanical impedances into equivalent quantities Z_{eq1} and Z_{eq2} defined in (6), with equivalent force inlets $\widehat{F}_{Zeq1}$ and $\widehat{F}_{Zeq2}$ to the velocity nodes as detailed in Fig. 3b.

$$
\begin{aligned}
Z_{eq1} &= Z_{m1} + Z_{A1} + Z_{B1} + Z_{K1} + Z_{D1} \\
Z_{eq2} &= Z_{m2} + Z_{A2} + Z_{B2} + Z_{K2} + Z_{D2}
\end{aligned} \tag{6}
$$

We seek to isolate the PTO from the rest of the system and apply Thévenin's theorem across the PTO nodes resulting in the *canonical form* of Fig. 2e. This entails solving for two properties of the dynamic system, the free relative velocity difference and the PTO clamped through-force as described in the following section.

3.1.1. Free velocity difference

The free relative velocity is the difference between the velocity of the float and velocity of the spar when the PTO impedance is eliminated. The circuit for the free velocity problem is described in Fig. 4a. Using Kirchhoff's Node Law on each velocity node results in:

$$\widehat{F}_{ex1} = \widehat{F}_{C1_{Free}} + \widehat{F}_{Zeq1_{Free}}|_{Node1} \tag{7}$$

$$\widehat{F}_{ex2} = \widehat{F}_{C2_{Free}} + \widehat{F}_{Zeq2_{Free}}|_{Node2} \tag{8}$$

Substituting the following impedance relations into (7) and (8).

$$
\begin{aligned}
\widehat{F}_{C1_{Free}} &= Z_C\widehat{u}_{2_{Free}} \;\&\; \widehat{F}_{Zeq1_{Free}} = Z_{eq1}\widehat{u}_{1_{Free}} \;\&\; \widehat{F}_{C2_{Free}} \\
&= Z_C\widehat{u}_{1_{Free}} \;\&\; \widehat{F}_{Zeq2_{Free}} = Z_{eq2}\widehat{u}_{2_{Free}}
\end{aligned} \tag{9}
$$

yields:

$$\widehat{F}_{ex1} = Z_C\widehat{u}_{2_{Free}} + Z_{eq1}\widehat{u}_{1_{Free}}|_{Node1} \tag{10}$$

$$\widehat{F}_{ex2} = Z_C\widehat{u}_{1_{Free}} + Z_{eq2}\widehat{u}_{2_{Free}}|_{Node2} \tag{11}$$

Using (10) and (11) to solve for $\widehat{u}_{r_{Free}} = \widehat{u}_{1_{Free}} - \widehat{u}_{2_{Free}}$ gives the free velocity difference as:

$$\widehat{u}_{r_{Free}} = \frac{\widehat{F}_{ex1}Z_{eq2} - \widehat{F}_{ex1}Z_{eq1} - Z_C\left(\widehat{F}_{ex1} + \widehat{F}_{ex2}\right)}{Z_{eq1}Z_{eq2} - Z_C^2} \tag{12}$$

3.1.2. PTO clamped through-force

The clamped through-force is the force developed through the PTO when the PTO is rigidly secured between the float and spar. The circuit for the case of a clamped PTO is described in Fig. 4b. Under the clamped condition, both the float and spar are constrained to move together and hence there is no relative motion across the PTO leading to:

$$\widehat{u}_1 = \widehat{u}_2 = \widehat{u}_{Clamp} \tag{13}$$

Applying Kirchhoff's Node Law on each velocity node results in:

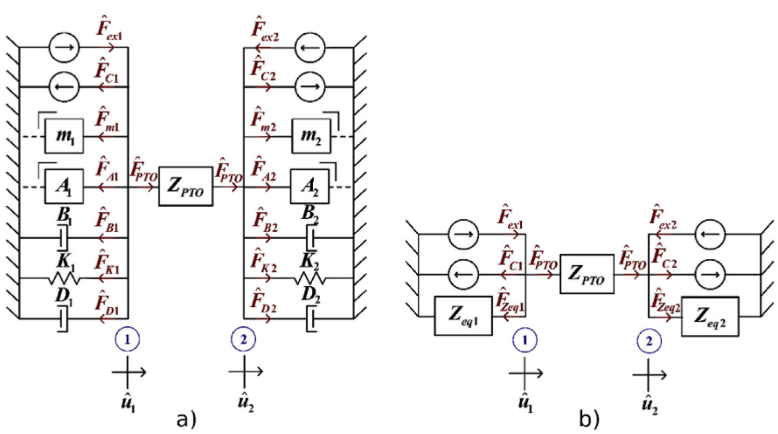

Fig. 3. Mechanical Circuits for Falnes' SRPA Device: a) Full Circuit; b) Simplified Circuit.

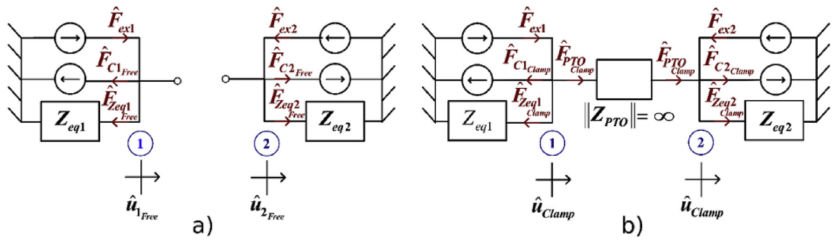

Fig. 4. Solving for the Thévenin Equivalent System. a) Free Relative Velocity; b) Clamped Through-Force.

$$\widehat{F}_{ex1} = \widehat{F}_{C1_{Clamp}} + \widehat{F}_{PTO_{Clamp}} + \widehat{F}_{Zeq1_{Clamp}}|_{Node_1} \tag{14}$$

$$\widehat{F}_{ex2} = \widehat{F}_{C2_{Clamp}} - \widehat{F}_{PTO_{Clamp}} + \widehat{F}_{Zeq2_{Clamp}}|_{Node_2} \tag{15}$$

Substituting the following impedance relations into (14) and (15).

$$\widehat{F}_{C1_{Clamp}} = Z_C \widehat{u}_{Clamp} \;\&\; \widehat{F}_{Zeq1_{Clamp}} = Z_{eq1}\widehat{u}_{Clamp} \;\&\; \widehat{F}_{C2_{Clamp}} = Z_C \widehat{u}_{Clamp} \;\&\; \widehat{F}_{Zeq2_{Clamp}} = Z_{eq2}\widehat{u}_{Clamp} \tag{16}$$

yields:

$$\widehat{F}_{ex1} = Z_C \widehat{u}_{Clamp} + \widehat{F}_{PTO_{Clamp}} + Z_{eq1}\widehat{u}_{Clamp}|_{Node_1} \tag{17}$$

$$\widehat{F}_{ex2} = Z_C \widehat{u}_{Clamp} - \widehat{F}_{PTO_{Clamp}} + Z_{eq2}\widehat{u}_{Clamp}|_{Node_2} \tag{18}$$

Using (17) and (18) to solve for $\widehat{F}_{PTO_{Clamp}}$ while eliminating $\widehat{u}_{Clamp}$ results in:

$$\widehat{F}_{PTO_{Clamp}} = \frac{\widehat{F}_{ex1}Z_{eq2} - \widehat{F}_{ex2}Z_{eq1} - Z_C\left(\widehat{F}_{ex1} + \widehat{F}_{ex2}\right)}{Z_{eq1} + 2Z_C + Z_{eq2}} \tag{19}$$

3.1.3. Phenomenological single body intrinsic impedance

The intrinsic impedance of the phenomenological single body system is calculated as:

$$Z_{i_{Falnes}} = \frac{\widehat{F}_{PTO_{Clamp}}}{\widehat{u}_{r_{Free}}} = \frac{Z_{eq1}Z_{eq2} - Z_C^2}{Z_{eq1} + Z_{eq2} + 2Z_C} \tag{20}$$

This result, along with $\widehat{F}_{PTO_{Clamp}}$ and $\widehat{u}_{r_{Free}}$ are in exact agreement with Falnes' original findings [17]. Fig. 2e depicts the ensuing circuit representation of the phenomenological single body WEC connected to the PTO load in parallel with the PTO clamped through force embodying the equivalent excitation force.

3.2. Perturbation of Falnes' SRPA with coupled PTO friction

Having shown that the technique is entirely consistent with Falnes' original derivations, we augment Falnes' original SRPA dynamic model with a term representing additional linearized friction in the PTO (e.g. bearing friction). The perturbation to the mechanical circuit consists of appending a damper element to nodes 1 and 2 in parallel with the original PTO impedance, as seen in Fig. 5.

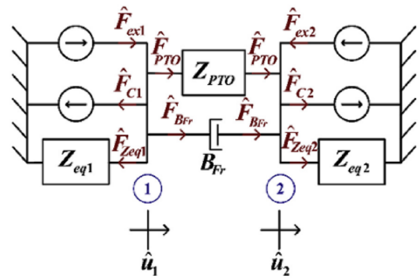

Fig. 5. Simplified SRPA circuit model with coupled PTO friction.

Thévenin's theorem is applied once again to the terminals of the PTO through solving for both the relative open circuit velocity difference and the PTO clamped through force.

3.2.1. Free velocity difference

The circuit for the free velocity problem is described in Fig. 6a. Using Kirchhoff's Node Law on each velocity node results in:

$$\widehat{F}_{ex1} = Z_C \widehat{u}_{2_{Free}} - Z_{eq1}\widehat{u}_{1_{Free}} + B_{Fr}\left(\widehat{u}_{1_{Free}} - \widehat{u}_{2_{Free}}\right)|_{Node_1} \tag{21}$$

$$\widehat{F}_{ex2} = Z_C \widehat{u}_{1_{Free}} - Z_{eq2}\widehat{u}_{2_{Free}} - B_{Fr}\left(\widehat{u}_{1_{Free}} - \widehat{u}_{2_{Free}}\right)|_{Node_2} \tag{22}$$

For which we can solve for $\widehat{u}_{r_{Free}}$ as:

$$\widehat{u}_{r_{Free}} = \widehat{u}_{1_{Free}} - \widehat{u}_{2_{Free}} = \frac{\widehat{F}_{ex1}Z_2 - \widehat{F}_{ex2}Z_{eq1} + Z_C\left(\widehat{F}_{ex1} - \widehat{F}_{ex2}\right)}{Z_C^2 - Z_{eq1}Z_{eq2} - B_{Fr}(Z_{eq1} + Z_{eq2} + 2Z_C)} \tag{23}$$

3.2.2. PTO clamped through-force

When solving for the clamped through-force ($\widehat{F}_{PTO_{Clamp}}$) we note that under the condition of $\|Z_{PTO}\| = \infty$ all the force between nodes 1 and 2 passes through the PTO. As such the clamped through-force mirrors the result in (19) from Section 3.1.2.

3.2.3. Phenomenological single body intrinsic impedance

The phenomenological single body intrinsic impedance is solved for in the standard manner. We note Z_i for this case (24) is perturbed relative to Falnes' solution (20) by the addition of B_{Fr}.

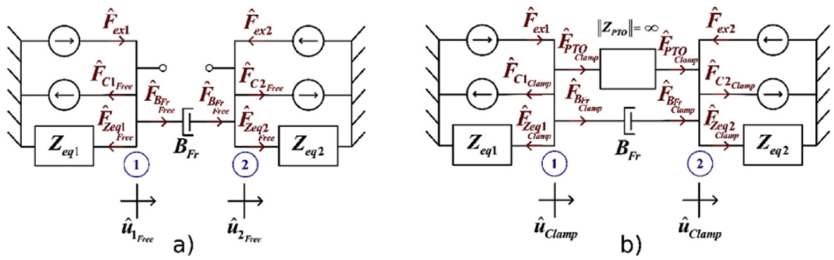

Fig. 6. Solving for the Thévenin Equivalent System of SRPA with PTO Friction. a) Free Velocity; b) Clamped Through Force.

$$Z_i = \frac{\widehat{F}_{PTO_{Clamp}}}{\widehat{u}_{r_{Free}}} = \frac{Z_{eq1}Z_{eq2} - Z_C^2}{Z_{eq1} + Z_{eq2} + 2Z_C} - B_{Fr} = Z_{i_{Falnes}} - B_{Fr} \tag{24}$$

3.3. Korde's force compensated WEC

Finally, we use of the mechanical circuit technique on a complex WEC architecture proposed by Korde, shown in Fig. 1c, which includes both a reaction mass and an external force compensator [9]. Applying the same methodology to generate the mechanical circuit from the free body diagram results in Fig. 7, using the parameter definitions proposed by Korde [9]. The mechanical circuit in Fig. 7a is simplified through application of parallel ($||$) and series ($^\circ-^\circ$) circuit laws to yield Fig. 7b with new lumpsum impedance terms (25) and (26). Λ is the complex impedance of the force compensator defined as $\Lambda = \Lambda_R + i\Lambda_C$.

$$Z_{eq1}(\Lambda) = Z_{MC}||[Z_{Mm}{}^\circ-{}^\circ(Z_{Km}||\Lambda)] = Z_{MC} + \frac{Z_{Mm}(Z_{Km}+\Lambda)}{Z_{Mm}+Z_{Km}+\Lambda} \tag{25}$$

$$Z_{eq2} = Z_{\mu\omega}||Z_{Bx}||Z_{M\omega}||Z_{MS} = Z_{\mu\omega} + Z_{Bx} + Z_{M\omega} + Z_{MS} \tag{26}$$

With this simplified mechanical circuit established, Thévenin's theorem is applied once again to the terminals of the PTO through solving for both the relative open circuit velocity difference and the clamped through-force shown in Fig. 8.

3.3.1. Free velocity difference

The circuit for the free velocity problem is described in Fig. 8a. Using Kirchhoff's Node Law on each velocity node results in:

$$\widehat{F}_{Zeq1_{Free}} = \widehat{F}_{KC_{Free}}|_{Node_2} \tag{27}$$

$$\widehat{F}_{KC_{Free}} + \widehat{F}_{Zeq2_{Free}} = \widehat{F}_D|_{Node_3} \tag{28}$$

Substituting the following impedance relations into (27) and (28),

$$\widehat{F}_{Zeq1_{Free}} = Z_{eq1}\widehat{u}_{C_{Free}} \;\&\; \widehat{F}_{KC_{Free}} = Z_{KC}(\widehat{u}_{Free} - \widehat{u}_{C_{Free}}) \;\&\; \widehat{F}_{Zeq2} = Z_{eq2}\widehat{u}_{Free} \tag{29}$$

yields:

$$Z_{eq1}\widehat{u}_{C_{Free}} = Z_{KC}(\widehat{u}_{Free} - \widehat{u}_{C_{Free}})|_{Node_2} \tag{30}$$

$$Z_{KC}(\widehat{u}_{Free} - \widehat{u}_{C_{Free}}) + Z_{eq2}\widehat{u}_{Free} = \widehat{F}_D|_{Node_3} \tag{31}$$

For which we can solve for $\widehat{u}_{r_{Free}}$ as:

$$\widehat{u}_{r_{Free}} = \widehat{u}_{Free} - \widehat{u}_{C_{Free}} = \frac{\widehat{F}_D Z_{eq1}}{Z_{KC}(Z_{eq1} + Z_{eq2}) + Z_{eq1}Z_{eq2}} \tag{32}$$

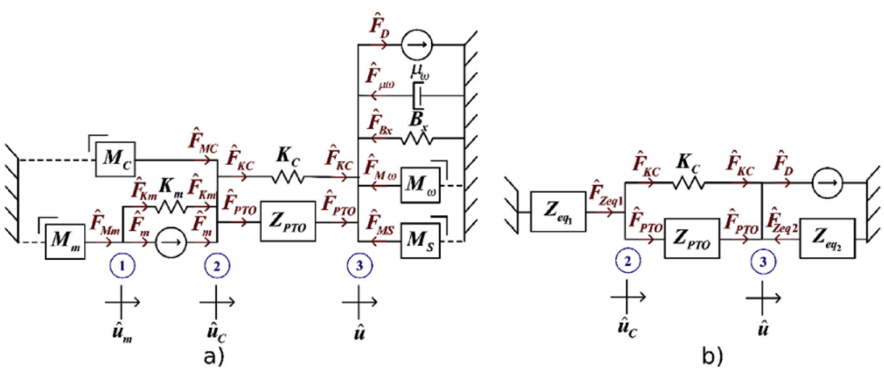

Fig. 7. Mechanical Circuits for Korde's Device: a) Full Circuit; b) Simplified Circuit.

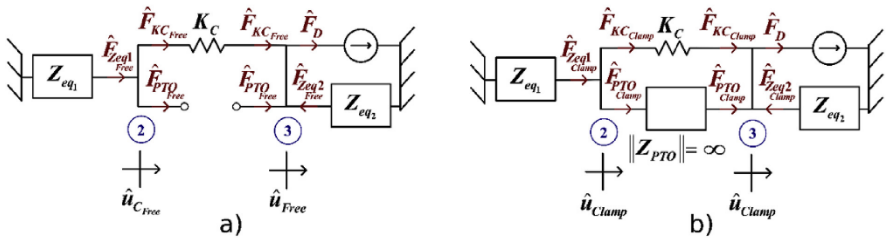

Fig. 8. Solving for the Thévenin Equivalent System for Korde's WEC. a) Free Relative Velocity; b) Clamped Through-Force.

3.3.2. PTO clamped through-force

When solving for $\widehat{F}_{PTO_{Clamp}}$ we note that, under the condition of $\|Z_{PTO}\| = \infty$, all the force between nodes 2 and 3 in Fig. 8 again travels through the PTO. Applying Kirchhoff's Node Law at each velocity node results in:

$$\widehat{F}_{Zeq1_{Clamp}} = \widehat{F}_{PTO_{Clamp}}|_{Node_2} \tag{33}$$

$$\widehat{F}_{PTO_{Clamp}} + \widehat{F}_{Zeq2_{Clamp}} = \widehat{F}_D|_{Node_3} \tag{34}$$

Substituting the following impedance relations into (33) and (34),

$$\widehat{F}_{Zeq1_{Clamp}} = Z_{eq1}\widehat{u}_{Clamp} \,\&\, \widehat{F}_{Zeq2_{Clamp}} = Z_{eq2}\widehat{u}_{Clamp} \tag{35}$$

yields:

$$Z_{eq1}\widehat{u}_{Clamp} = \widehat{F}_{PTO_{Clamp}}|_{Node_2} \tag{36}$$

$$\widehat{F}_{PTO_{Clamp}} + Z_{eq2}\widehat{u}_{Clamp} = \widehat{F}_D|_{Node_3} \tag{37}$$

Using (36) and (37), $\widehat{F}_{PTO_{Clamp}}$ is isolated:

$$\widehat{F}_{PTO_{Clamp}} = \frac{\widehat{F}_D Z_{eq1}}{Z_{eq1} + Z_{eq2}} \tag{38}$$

3.3.3. Phenomenological single body intrinsic impedance

The solution for $Z_i(\Lambda)$ is independent of constraints on the force compensator and is derived as:

$$Z_i(\Lambda) = \frac{\widehat{F}_{PTO_{Clamp}}}{\widehat{u}_{r_{Free}}} = \frac{Z_{eq1}(\Lambda)Z_{eq2}}{Z_{eq1}(\Lambda) + Z_{eq2}} + Z_{KC} \tag{39}$$

Through rote application of the mechanical circuit methodology, Korde's advanced WEC has been represented in the *canonical form* of Fig. 2e as the previous examples.

4. Discussion

To generalize our findings, we explicitly note Thévenin's theorem was successfully applied to all three WEC *architectures* described in Section 3 regardless of topological complexity, yielding the *canonical form* represented by Fig. 2e. In the following section, we now use these algebraic equations for Z_i and $\widehat{F}_{PTO_{Clamp}}$ from Section 3 to build analytical expressions for $P_{U_{Max}}$ that can be mined to establish important design principles applicable to linear WEC *architectures*. In the case of Falnes' perturbed SRPA we analyse the influence of introducing linear viscous friction in the PTO, leading to a counterintuitive condition on the optimal PTO force response. We then examine our generalized solution of $P_{U_{Max}}$ for Korde's WEC and expose an important technical trade off in implementing a force compensated platform [9].

4.1. Phenomenological equivalence

In Section 3.1 we used the mechanical circuit framework to reproduce Falnes' results for Z_i $\widehat{F}_{PTO_{Clamp}}$, and $\widehat{u}_{r_{Free}}$ for the SRPA *architecture*, thus validating the methodology. In Section 2 we proposed a Thévenin equivalent single body mechanical circuit as viewed in Fig. 2e, but noted discrepancies with what is currently published in the wave energy literature [6] [25],– [27]. We show here how our Thévenin circuit topology is consistent with Falnes' formulations based on his original choice in defining mechanical impedance as the ratio of force to velocity [14], [15].

The time average power captured by a SRPA WEC per excitation frequency is described by (40) [17].

$$P_U = \frac{1}{2}\Re e\{Z_{PTO}\}|\widehat{u}_r|^2 \tag{40}$$

We note that $P_{U_{Max}}$ is determined from (40) when Falnes' *elegant rule* is enforced. This requires determining the optimal relative velocity ($\widehat{u}_{r_{opt}}$) that results when imposing (1). To validate our claim, we will reproduce (3) using (40), (1), and the mechanical circuit framework on our proposed Thévenin equivalent circuit, shown in Fig. 2e, for the case of complex conjugate PTO force control.

Applying Kirchhoff's Node Law at Node 1 of Fig. 2e yields.

$$\widehat{F}_{PTO_{Clamp}} = \widehat{F}_i + \widehat{F}_{PTO} \tag{41}$$

Substitution of the following impedance relations into (41):

$$\widehat{F}_i = Z_i\widehat{u}_r \,\&\, \widehat{F}_{PTO} = Z_{PTO}\widehat{u}_r \tag{42}$$

yields:

$$\widehat{F}_{PTO_{Clamp}} = Z_i\widehat{u}_r + Z_{PTO}\widehat{u}_r \tag{43}$$

and rearranging (43) to solve for $\widehat{u}_r$:

$$\widehat{u}_r = \frac{\widehat{F}_{PTO_{Clamp}}}{Z_i + Z_{PTO}} \tag{44}$$

By enforcing (1) on (44), the optimal relationship between the relative body velocity and the equivalent excitation force described by (45) is achieved [17].

$$\hat{u}_{r_{opt}} = \frac{\hat{F}_{PTO_{Clamp}}}{2\Re e\{Z_i\}} \tag{45}$$

Substitution of (45) and (1) into (40) leads to (46) the maximum power captured under optimal complex conjugate PTO force control.

$$P_{U_{Max(CC)}} = \frac{\left|\hat{F}_{PTO_{Clamp}}\right|^2}{8\Re e\{Z_i\}} \tag{46}$$

This matches (3) and is in alignment with Falnes result for the SRPA *architecture*, and thus validates our claim on the *canonical form* shown in Fig. 2e [17]. Using the same argument for the optimal amplitude condition by enforcing (2) on (44) while substituting into (40), the same conclusion can be analytically derived for an optimal passive PTO in (4).

To optimize a WEC *architecture* for evaluating the power capture performance ceiling $P_{U_{Max}}|_{opt}$, a mechanical designer can: 1) build the associated mechanical circuit; 2) determine both Z_i and $\hat{F}_{PTO_{Clamp}}$ through application of Thévenin's theorem; 3) use (3) or (4) to calculate $P_{U_{Max}}$ for this *architecture*; and 4) form and solve the geometry control optimization problem using $P_{U_{Max}}$ to search for $P_{U_{Max}}|_{opt}$ via the geometric parameters.

4.2. Perturbed SRPA with coupled PTO friction

In Section 3.2 we modified Falnes SRPA *architecture* by adding a linearized friction component in parallel with the PTO, because any mechanism providing coupling between wave activated bodies and the PTO will be subject to friction. We compare (20) with (24), to investigate what implications neglecting friction has on optimal PTO force control.

The impedance for a linearized PTO may be represented mathematically as the generic complex quantity in (47).

$$Z_{PTO} = R_{PTO} + iX_{PTO} \tag{47}$$

The application of complex conjugate control to this *architecture* requires enforcing (1) on (24) yielding:

$$Z_{PTO_{opt}} = Z_i^* = Z_{i_{Falnes}}^* + B_{Fr}^* \tag{48}$$

Since the linear viscous friction is real valued, the complex conjugate and the original are the same ($B_{Fr}^* = B_{Fr}$) hence:

$$R_{PTO_{opt}} = \Re e\{Z_{i_{Falnes}}\} + B_{Fr} \tag{49}$$

In pragmatic language, in order to apply the complex conjugate impedance matching constraint (1), $R_{PTO_{opt}}$ must increase, rather than decrease, with the increasing resistance offered by friction B_{Fr}. This is not a physically intuitive result, but is necessary for application of optimal PTO force control in frequency domain models.

In performing experimental trials on a physical SRPA device, it is inadequate to apply Falnes' original result (20) verbatim. As the friction in the PTO increases, so must $R_{PTO_{opt}}$ to maintain the optimal condition. If the linearized viscous friction is ignored, the result leads to an unmatched power transfer condition and ultimately yields to power loss at the WEC-PTO interface.

4.3. Korde's force compensated WEC

In Section 3.3, we modelled a complex WEC *architecture* proposed by Korde, built the *canonical form*, and determined both Z_i and $\hat{F}_{PTO_{Clamp}}$. A simplified expression for $P_{U_{Max(CC)}}$ in (50) is generated by substituting (38) and (39) into (46) along with rudimentary algebraic manipulation.

$$P_{U_{Max(CC)}}(\Lambda) = \frac{\left|\hat{F}_D\right|^2 \left|Z_{eq1}\right|^2}{8\left[\frac{\Lambda_R \left|Z_{Mm}\right|^2 \left|Z_{eq2}\right|^2}{\left|Z_{Mm}+Z_{Km}+\Lambda\right|^2} + Z_{\mu\omega}\left|Z_{eq1}\right|^2\right]} \tag{50}$$

In (50) the geometry control optimization problem only has a single degree of freedom: the force compensator impedance (Λ). Assuming the force compensator does not inject real power into the system (i.e. $\Lambda_R \geq 0$ is satisfied), it is clear by observation that $P_{U_{Max(CC)}}$ is optimized when $\Lambda_R = 0$. Subsequently, $P_{U_{Max(CC)}}$ becomes (51) which is consistent with Korde [9].

$$P_{U_{Max(CC)}}|_{opt} = \frac{\left|\hat{F}_D\right|^2}{8Z_{\mu\omega}} \tag{51}$$

This means that $P_{U_{Max(CC)}}|_{opt}$ is independent of Λ_C; the power capture ceiling given in (51) does not depend on the reactive power injected by Korde's force compensator, and the force compensator is seen to not produce any performance improvement. Thus $Z_{PTO_{opt}}$ is not unique, but is dependent on Λ_C, whereas $P_{U_{Max(CC)}}|_{opt}$ is independent of the presence of the force compensator.

In Korde's work, the nature of the simultaneous analytical optimization of both the PTO and geometric parameters masked this independence. Korde imposed a secondary objective (holding the platform stationary: $\hat{u}_C = 0$) that constrained his solution space to a particular point in this infinite set (51) [9]. This constraint created the illusion of an optimal setting of $Z_{PTO_{opt}}$, when in reality (51) could be achieved through an infinity of possible cases. Hence, the mechanical circuit framework has simplified the optimization procedure by enforcing the master-slave relationship, and revealed the true relationship between Λ_C and $P_{U_{Max(CC)}}|_{opt}$, without requiring either numerical specification of the system parameters, or the use of numerical optimization techniques.

Further, the generality of (25) allows us to determine and apply Korde's secondary objective through mere observation and, unlike Korde, without calculating the complex body velocities. Applying insight from Falnes [17], the platform remains stationary subject to a finite external force excitation $\hat{F}_{eq1}$ only if $Z_{eq1} = \infty$, therefore from (25), this requires $\Lambda|_{\hat{u}_C=0} = -Z_{Mm} - Z_{Km}$ (cf. (29) [9]). Through substitution of this condition into both (38)–(39) and application of (1), our solutions collapse to the results predicted by Korde (cf. (41) [9]).

$$\hat{F}_{PTO_{Clamp}} = \hat{F}_D \;\&\; Z_{PTO_{opt}} = Z_{HH}^* \tag{52}$$

A physical explanation of the independence of $P_{U_{Max(CC)}}|_{opt}$ and Λ_C follows. Korde's force compensator only injects reactive power into the system. With the PTO operating in optimal complex conjugate control mode, the PTO is able to adapt to the conditions imposed by the force compensator to guarantee resonance, through enforcing the master-slave relationship, always ensuring maximum power capture. Thus, as noted in (51), Λ_C is not serving $P_{U_{Max(CC)}}|_{opt}$, but rather responsible for keeping the platform stationary while optimal power is being captured. In employing a constrained multivariate analytical optimization methodology, Korde was unable to recognize that the stationary platform was not a prerequisite to achieving optimal power capture.

Insight into these dynamics are only uncovered through explicit separation of the optimal PTO force and geometry control problems offered by the mechanical circuit framework.

5. Conclusions

To be a competitive form of renewable energy, WEC conceptual design convergence must be achieved and further research efforts need to focus on areas with promising performance. To encourage the identification of WEC *architectures* which support this goal, a systematic methodology using the mechanical circuit framework has been proposed which builds on the fundamental contributions of Falnes to optimal PTO force control already widely accepted in the wave energy community. Through generalizing the application of Thévenin's theorem to WEC *architectures* of infinite complexity, a method to establishing the power capture ceiling for any *architecture* has been identified, thus enabling objective comparisons and promoting convergence.

In this paper, we have used the mechanical circuit framework to reproduce Falnes' seminal results on the SRPA *architecture*, and successfully applied the framework on both a perturbed SRPA *architecture* with viscous friction, and a complex WEC *architecture* proposed by Korde. Important insights into the WEC system dynamics have been exposed through enforcing the master-slave relationship between the geometry and PTO force parameters, thus reducing the degrees of freedom of the optimization and shrinking the solution space. Our application of mechanical circuits has been to provide analytical insight at the WEC *architecture* level. However, once $P_{U_{Max}}|_{opt}$ is established for an *architecture*, substitution of device parameters into the canonical form, provides a means of comparing the performance of a device *configuration* against the absolute metric $P_{U_{Max}}|_{opt}$, and will be the subject of future work.

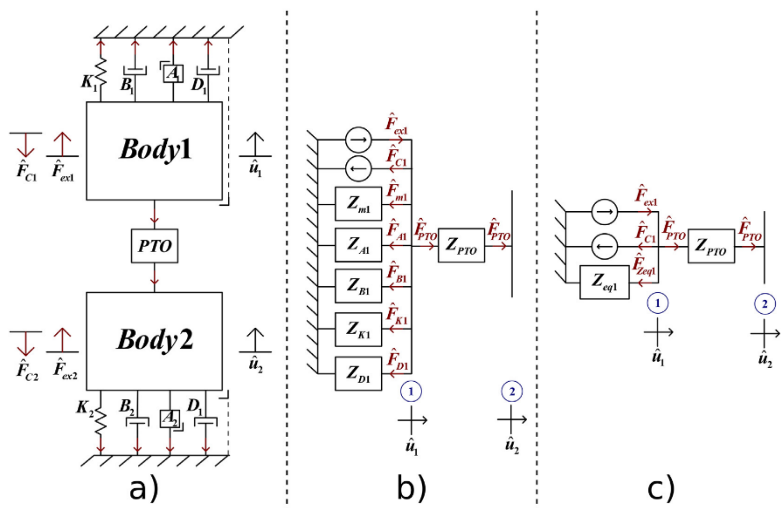

Fig. 9. Generating a Mechanical Circuit. a) Free Body Diagram of SRPA WEC; b) Full Mechanical Circuit of Body 1; c) Reduced Mechanical Circuit of Body 1.

The methodology presented in this work, has been applied to heaving WEC *architectures* only, however the technique can be readily employed to a variety of WEC designs and, thus, is an inexpensive means to coarsely evaluate, optimize, and compare the performances of competing concepts, early in the development phase of a WEC device. In particular, linearized pitching WEC *architectures* may be modelled using the same formulations, where force, velocity, and linear translational components are replaced with their rotational counterparts [22,28]. In WEC *architectures*, designed using multi-physical domains (e.g. mechanical translation and rotation), transducer components are required to interface the domains [22].

Ultimately, the objective of this work is to present a methodology used to determine the optimum device *configuration* in a *class* for a specific wave climate, by evaluating and comparing $P_{U_{Max}}|_{opt}$ for all feasible *architectures* within a *class*. Such a universal methodology does not currently exist.

Acknowledgments

We would like to acknowledge the support of the Natural Sciences and Engineering Research Council of Canada, Natural Resources Canada, and the Pacific Institute for Climate Solutions in funding this research. Personal gratitude goes to Dr. Helen Bailey, Dr. Scott Beatty, and Mr. Alexandros Dimopoulos for various helpful discussions in formalizing the theoretical basis for this work.

Appendix A. Generating a mechanical circuit from a free body diagram

The motivation of this Appendix is to describe the detailed process of generating the mechanical circuit representation of a WEC from a Newtonian Free Body Diagram. We use Falnes' well-established two body SRPA WEC as our example along with his associated hydrodynamic and external force definitions [17].

From FBD for Body 1:

$$\sum \widehat{F}_{Body1} = -\widehat{F}_{A1} - \widehat{F}_{B1} - \widehat{F}_{K1} - \widehat{F}_{C1} - \widehat{F}_{D1} - \widehat{F}_{PTO} + \widehat{F}_{ex1} = \widehat{F}_{m1} \tag{53}$$

Substitute impedance form for each force into (53) and rearrange so all terms are positive.

$$\widehat{F}_{ex1} = Z_{m1}\widehat{u}_1 + Z_{A1}\widehat{u}_1 + Z_{B1}\widehat{u}_1 + Z_{K1}\widehat{u}_1 + Z_{D1}\widehat{u}_1 + \widehat{F}_{C1} + Z_{PTO}(\widehat{u}_1 - \widehat{u}_2) \tag{54}$$

Noting Kirchhoff's Node Law (5), on the left side of (54), $\widehat{F}_{ex1}$ points into the $\widehat{u}_1$ velocity node while all the forces on the right side point out of $\widehat{u}_1$. $\widehat{F}_{PTO}$ also points into the $\widehat{u}_2$ velocity node. Using this information, we sketch the mechanical circuit and place the impedance blocks as in Fig. 9b. We explicitly note mass elements require one node connected to ground and results with the mass elements in parallel with the remaining impedance network.

Utilizing the parallel law for combining impedance elements, we achieve our simplified mechanical circuit in Fig. 9c. The same approach is repeated for Body 2 and the circuit is appended with additional impedance blocks yielding the final mechanical circuit displayed in Fig. 3b.

Appendix B. Table of mechanical circuit elements

The following table contains a description and pictorial representation of the mechanical circuit elements considered in this body of work alongside the mathematical constitutive impedance equations.

Table 1
Mechanical circuit elements.

Element Description:	Circuit Element	Constitutive Equation
Generic Mechanical Impedance	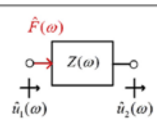	$Z(\omega) = \frac{\widehat{F}(\omega)}{\widehat{u}_1(\omega) - \widehat{u}_2(\omega)}$
External Force Source	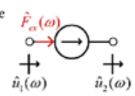	$\widehat{F}_{ex}(\omega) = Z_{F_{ex}}(\omega)[\widehat{u}_1(\omega) - \widehat{u}_2(\omega)]$
Ideal Mechanical Spring	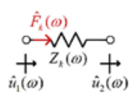	$Z_k(\omega) = -\frac{ik}{\omega}$ $\widehat{F}_k(\omega) = Z_k(\omega)[\widehat{u}_1(\omega) - \widehat{u}_2(\omega)]$
Ideal Mechanical Damper	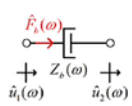	$Z_b(\omega) = b$ $\widehat{F}_b(\omega) = Z_b(\omega)[\widehat{u}_1(\omega) - \widehat{u}_2(\omega)]$
Ideal Mechanical Mass	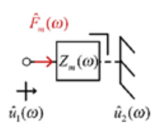	$Z_m(\omega) = i\omega m$ $\widehat{F}_m(\omega) = Z_m(\omega)[\widehat{u}_1(\omega)]$

References

[1] OES, Ocean Energy Systems: Annual Report 2015, 2015.
[2] Key World Energy Statistics (KWES): 2016, International Energy Agency, 2016.
[3] J. Weber, WEC technology readiness and performance Matrix–finding the best research technology development trajectory, in: International Conference on Ocean Energy, 2012.
[4] A. Babarit, A database of capture width ratio of wave energy converters, Renew. Energy 80 (Aug. 2015) 610–628.
[5] A.F. de, O. Falcão, Wave energy utilization: a review of the technologies, Renew. Sustain. Energy Rev. 14 (no. 3) (Apr. 2010) 899–918.
[6] M. Folley, Numerical Modelling of Wave Energy Converters: State-of-the-art Techniques for Single Wec and Converter Arrays, first ed., Elsevier, Cambridge, MA, 2016.
[7] K. Budal, J. Falnes, A resonant point absorber of ocean-wave power, Nature 256 (no. 5517) (1975) 478–479.
[8] K. Budal, "Floating structure with heave motion reduced by force compensation, in: Proceedings, Fourth International Offshore Mechanics and Arctic Engineering Symposium, 1985, pp. 92–101.
[9] U.A. Korde, "On providing a reaction for efficient wave energy absorption by floating devices, Appl. Ocean. Res. 21 (no. 5) (1999) 235–248.
[10] S.J. Beatty, M. Hall, B.J. Buckham, P. Wild, B. Bocking, Experimental and numerical comparisons of self-reacting point absorber wave energy converters in regular waves, Ocean. Eng. 104 (2015) 370–386.
[11] M. Penalba, J.V. Ringwood, A review of wave-to-wire models for wave energy converters, Energies 9 (no. 7) (Jun. 2016) 506.
[12] A.A.E. Price, C.J. Dent, A.R. Wallace, On the capture width of wave energy converters, Appl. Ocean. Res. 31 (no. 4) (Oct. 2009) 251–259.
[13] J.H. Todalshaug, G.S. Asgeirsson, E. Hjálmarsson, J. Maillet, P. Möller, P. Pires, …, M. Lopes, Tank testing of an inherently phase-controlled wave energy converter, Int. J. Mar. Energy 15 (2016) 68–84.
[14] J. Falnes, Ocean Waves and Oscillating Systems: Linear Interactions Including Wave-energy Extraction, Cambridge University Press, Cambridge ; New York, 2002.
[15] C.M. Harris, C.E. Crede, H.M. Trent, Shock and Vibration Handbook, first ed., vol. 1, 1962 vol. 15.
[16] L. Thévenin, Extension de la loi d'Ohm aux circuits électromoteurs complexes [Extension of Ohm's law to complex electromotive circuits], in: Annales Télégraphiques, vol. 10, 1883, pp. 222–224.
[17] J. Falnes, Wave-energy conversion through relative motion between two single-mode oscillating bodies, J. Offshore Mech. Arct. Eng. 121 (no. 1) (Feb. 1999) 32–38.
[18] M.J. French, R. Bracewell, Heaving point absorbers reacting against an internal mass, in: D.D.V. Evans, P.A.F.O. de Falcão (Eds.), Hydrodynamics of Ocean Wave-energy UtilizationSpringer Berlin Heidelberg, 1986, pp. 247–255.
[19] C.A. Diamond, C.Q. Judge, B. Orazov, Ö. Savaş, O.M. O'Reilly, Mass-modulation schemes for a class of wave energy converters: experiments, models, and efficacy, Ocean. Eng. 104 (2015) 452–468. Aug. 2015.
[20] P. Gardonio, M.J. Brennan, ON the origins and development of mobility and impedance methods in structural dynamics, J. Sound. Vib. 249 (no. 3) (Jan. 2002) 557–573.
[21] G. Kirchhoff, Ueber die Auflösung der Gleichungen, auf welche man bei der Untersuchung der linearen Vertheilung galvanischer Ströme geführt wird, Ann. Phys. 148 (no. 12) (Jan. 1847) 497–508.
[22] D. Rowell, D.N. Wormley, System Dynamics: an Introduction, Prentice Hall, 1997.
[23] P.H. Roe, Networks and Systems, Addison-Wesley, 1966.
[24] J.N. Newman, The interaction of stationary vessels with regular waves, in: Proceedings of the 11th Symposium on Naval Hydrodynamics, 1976, pp. 491–501. London.
[25] Institution of engineering and technology R. Alcorn, D. O'Sullivan, Electrical Design for Ocean Wave and Tidal Energy Systems, Institution of Engineering and Technology, Stevenage, U.K, 2013.
[26] J.V. Ringwood, G. Bacelli, F. Fusco, Energy-maximizing control of wave-energy converters: the development of control system technology to optimize their operation, IEEE Control Syst. 34 (no. 5) (Oct. 2014) 30–55.
[27] U.A. Korde, J. Ringwood, Hydrodynamic Control of Wave Energy Devices, Cambridge University Press, 2016.
[28] R.P.F. Gomes, M.F.P. Lopes, J.C.C. Henriques, L.M.C. Gato, A.F.O. Falcão, The dynamics and power extraction of bottom-hinged plate wave energy converters in regular and irregular waves, Ocean. Eng. 96 (Mar. 2015) 86–99.

7 Appendix B: On establishing an analytical power capture limit for self-reacting point absorber wave energy converters based on dynamic response

K. Bubbar, B. Buckham, On establishing an analytical power capture limit for self-reacting point absorber wave energy converters based on dynamic response, Applied Energy. 228 (2018) 324–338. doi:10.1016/j.apenergy.2018.06.099.

Applied Energy 228 (2018) 324–338

Contents lists available at ScienceDirect

Applied Energy

journal homepage: www.elsevier.com/locate/apenergy

On establishing an analytical power capture limit for self-reacting point absorber wave energy converters based on dynamic response

K. Bubbar*, B. Buckham

Department of Mechanical Engineering, West Coast Wave Initiative, Institute for Integrated Energy Systems, University of Victoria, 3800 Finnerty Rd, Victoria, B.C V8W 3P6, Canada

HIGHLIGHTS

- Proposed a new analytical power capture bound for SRPAs based on dynamic response.
- Proposed a new constraint equation relating the optimal float to spar impedance.
- Numerically demonstrated how the bound can be approached.
- Introduced inerters to wave energy community to implement optimal geometry control.
- Proposed a new condition for null power capture of SRPAs based on geometry control.

ARTICLE INFO

Keywords:
Self-reacting point absorbers
Power capture limit
Geometry control
Mechanical circuits
WEC canonical form
Impedance matching
Thévenin's theorem
Inerter technology

ABSTRACT

To be a competitive supply of renewable energy, the power capture performance of ocean wave energy converters must improve. This requires that wave energy converter designers identify and invest resources to develop devices that exhibit a strong Technology Performance Level early in the development process. We contend that completing this identification process at the conceptual design stage requires a generalized method to establish the power capture upper bound for any given wave energy converter architecture. This upper bound must reflect simultaneous implementation of both optimal geometry control and power take-off force control – components known to be essential to optimizing performance but difficult to envision for complex WEC architectures.

In this work, we develop and demonstrate a procedure, built on the mechanical circuit framework, to identify this upper bound for a self-reacting point absorber with an inertial modulation mechanism performing the geometry control. We illustrate how the analytical procedure generates generic design guidance, required to achieve the bound, without committing to a specific technology. We follow by formally introducing a new technology into the wave energy community, the inerter, capable of implementing the design guidance to enact the required geometry control. Finally, we apply the analytics within a numerical case study of a previously published wave energy converter configuration, and compare the power capture production of that device to one with equivalent hydrodynamics, but with the new geometry control feature set suggested by the new analytical procedure. Our analysis reveals the potential for a ten-fold increase in power capture even under stringent relative displacement constraints.

1. Introduction

Per unit area of ocean surface, the energy density of the conventional wave energy transport is understood to be ten times greater than the equivalent solar energy flux [1]. The annual offshore global wave energy resource is estimated to yield 16,000 TWh of energy, and this abundant availability has sparked further detailed resource forecasting studies [2–6]. However, the path to commercialization of Wave Energy Converter (WEC) devices is challenged by a dispersion of finite resources developing conceptually diverse WEC designs, thus impeding convergence on a single design architecture as witnessed in the wind energy sector [7–10]. To promote design convergence, Weber introduced the Technology Performance Level (TPL) metric [11] and emphasized the importance of assessing TPL early in a development program to identify technologies with a strong predicted performance once in their commercial state [12]. Robust TPL assessments are needed

* Corresponding author.
E-mail address: kbubbar@uvic.ca (K. Bubbar).

https://doi.org/10.1016/j.apenergy.2018.06.099
Received 28 January 2018; Received in revised form 14 May 2018; Accepted 20 June 2018

Nomenclature

Acronyms

PTO	Power Take-Off
SRPA	Self-Reacting Point Absorber
TPL	Technology Performance Level
TRL	Technology Readiness Level
WEC	Wave Energy Converter
COE	Cost of Energy

Parameters

β	transmission ratio
δ	ratio of bounded to unbounded displacement amplitude
ω	excitation angular frequency of the incoming wave elevation time series (rad/s)
$\hat{F}_{ex1}$, $\hat{F}_{ex2}$	complex amplitude of hydrodynamic excitation force on float, spar (N)
$\hat{F}_{FS1}$	complex force amplitude exerted by Force Source 1 (N)
$\hat{F}_{i}$	complex force amplitude exerted on the intrinsic mechanical impedance of the WEC (N)
$\hat{F}_{meff}$	complex reaction force amplitude exerted by the inerter (N)
$\hat{F}_{PTO}$	complex force amplitude exerted on the PTO (N)
$\hat{F}_{PTO_{Clamp}}$	complex force amplitude exerted on the PTO when the magnitude of the PTO impedance is infinite (N)
$\hat{F}_{Zeq1}$, $\hat{F}_{Zeq2}$	complex force amplitude exerted on the equivalent float, spar (N)
$\hat{F}_{Zeq1_{free}}$, $\hat{F}_{Zeq2_{free}}$	complex force amplitude exerted on the equivalent float, spar when the PTO impedance is zero (N)
$\hat{F}_{Zeq1_{Clamp}}$, $\hat{F}_{Zeq2_{Clamp}}$	complex force amplitude exerted on the equivalent float, spar when the magnitude of the PTO impedance is infinite (N)
J	moment of inertia of the inerter flywheel (kg·m^2)
k_3	linear spring stiffness coefficient coupled between the spar and reaction mass (N/m)
m_1, m_2, m_3	mass of the float, spar, and reaction mass (kg)
m_{eff}	inertance of the inerter (kg)
$m_{eff_{opt}}$	optimal inertance to maximize power capture (kg)
P_U	average useful power capture per excitation angular frequency (W)
$P_{U_{Max}}$	average useful power capture per excitation angular frequency under complex conjugate PTO force control (W)
$P_{U_{Max(AC)}}$	average useful power capture per excitation angular frequency under amplitude PTO force control (W)
$P_{U_{Max}}\rvert_{opt}$	average useful power capture per excitation angular frequency under complex conjugate PTO force control and optimal geometry control (W)
P_U^C	stroke limit constrained average useful power capture per excitation angular frequency (W)
$R_{eq2_{\min}}$	resistance of equivalent spar required for null power capture (Ns/m)
$R_{FS1_{opt}}$	optimal resistance of Force Source 1 to achieve the power capture limit (Ns/m)
$\hat{u}_1$, $\hat{u}_2$, $\hat{u}_3$	complex velocity amplitude of float, spar, and reaction mass (m/s)
$\hat{u}_{1_{free}}$, $\hat{u}_{2_{free}}$	complex velocity amplitude of float, spar, when the PTO impedance is zero (m/s)
$\hat{u}_{Clamp}$	complex velocity amplitude of float and spar, when the magnitude of the PTO impedance is infinite (m/s)
$\hat{u}_r$	complex relative velocity amplitude between the float and spar (m/s)
$\hat{u}_{r_{Free}}$	complex relative velocity amplitude between the float and spar when the PTO impedance is set to zero (m/s)
$\hat{u}_{r_{opt}}$	complex optimal relative velocity amplitude between the float and spar when the complex conjugate impedance matching conditions are satisfied (m/s)
X_{EM}	reactance of the Equivalent Mass of the spar (Ns/m)
$X_{eq2_{\min}}$	reactance of the equivalent spar required for null power capture (Ns/m)
$X_{FS1_{opt}}$	optimal reactance of Force Source 1 required to achieve the power capture limit (Ns/m)
Z, R, X	generic mechanical impedance, resistance, and reactance (Ns/m)
Z_{A11}, Z_{A22}	hydrodynamic added mass impedance of float, spar (Ns/m)
Z_{B11}, Z_{B22}	hydrodynamic radiation damping impedance of float, spar (Ns/m)
Z_C	coupled radiation impedance between float and spar (Ns/m)
Z_{eq1}, Z_{eq2}	equivalent impedance of float, spar (Ns/m)
$Z_{eq2_{opt}}$	optimal equivalent impedance of the spar required to achieve the power capture limit (Ns/m)
Z_{FS1}, X_{FS1}	impedance, reactance of force source 1 (Ns/m)
Z_i	intrinsic mechanical impedance of the WEC (Ns/m)
Z_{K1}, Z_{K2}	hydrostatic buoyancy stiffness impedance of float, spar (Ns/m)
Z_{m1}, Z_{m2}, Z_{m3}	mass impedance of float, spar, reaction mass (Ns/m)
Z_{meff}	inerter mechanical impedance (Ns/m)
Z_{mH2}	impedance of combined spar mass and spar hydrodynamics (Ns/m)
Z_{PTO}	PTO mechanical impedance (Ns/m)

to focus resources on developing complex WEC innovations with strong predicted power capture that, while challenging to perfect, are essential to long term techno-economic viability.

We contend that the importance of identifying these innovations cannot be understated. At present, for ocean wave energy to be a cost competitive source of renewable energy, the current cost of energy (COE) must be reduced by a factor of two [13]. Such drastic cuts in COE will not come solely from economies of scale in the manufacturing process – disruptive changes in WEC *architectures* (i.e. design topologies) that induce step changes in performance need to be discovered. The search for these new WEC *architectures* requires casting a wide net over the conceptual design space. Thus, a fast, accurate and sufficiently general method to establish the best possible TPL (i.e. the *power capture upper-bound*) of a new WEC *architecture* during the conceptual design stage (e.g. at low Technology Readiness Level) [11] is needed to steer WEC developers to converge towards promising innovations.

The goal of this work is to demonstrate the process of determining this *power capture upper bound* through a case study using the well-known Self-Reacting Point Absorber (SRPA) WEC architecture. In this case study, we will: (1) establish an analytical method to determine a new analytical upper bound for the "hydrodynamic wave power absorption" [12], (2) create generic design guidance in the form of an analytical expression detailing the constraints between hydrodynamic and inertial properties of the WEC that are essential to achieving the upper bound, (3) use this design guidance to propose a new technology, the *inerter*, to implement the predicted power capture improvements, and (4) examine how this generic design guidance can steer the discovery of new technology innovations for wave energy converter design.

1.1. Analytical methods

The typical design process for WECs follows by selecting: (1) a WEC device *class* based on operating principle (e.g. oscillating surging flaps),

(2) an appropriate WEC *architecture* (e.g. bottom mounted oscillating surging flap), (3) a set of physical specifications leading to a specific WEC *configuration* (e.g. Oyster™ or Wave$_2$O™). To ensure that the decisions made in the progression from *architecture* to *configuration* do not unnecessarily erode TPL, the analytical upper bound on power capture specific to a single *architecture* should be determined. This upper bound is used to both expose key relationships between features (e.g. Which *configuration* will realize the best possible performance?) and to numerically assess the consequences of logistical and heuristic constraints (e.g. How does the best possible performance degrade if we compromise a certain physical specification?). In short, establishing analytical upper bounds on power capture should initiate the climb up the TPL ladder.

To be relevant, the analytical bound must be based on realistic hydrodynamics and the implementation of optimal PTO force control. Falnes derived the analytical expressions for the optimal power capture of the single body point absorber *architecture* based on dynamic response, through forming a mechanical impedance matching problem between the power take-off (PTO) and remaining WEC [14]. He later extended his results to the SRPA *architecture* through application of Thévenin's theorem and transformed the SRPA into a phenomenological equivalent single body point absorber [15]. Bubbar et al. [10] extended Falnes' solutions by introducing the mechanical circuit framework as a means to represent and apply Thévenin's theorem to WEC *architectures* of greater complexity. The process proposed by Bubbar et al. was comprised of: (1) reducing the complex WEC *architecture* in question (e.g. a WEC comprised of several articulated bodies) into a *canonical form* – a phenomenological equivalent single body WEC, (2) using that *canonical form* to automatically enforce well understood constraints between the PTO parameters and the WEC's physical features (i.e. the *master–slave relationship* described in Section 1.2) and determining analytical expressions for the complex *architecture's* power capture when these constraints are satisfied (i.e. $P_{U_{Max}}$ defined in Section 2.1), and (3) analytically optimizing these power capture expressions over the WEC physical design space to yield a power capture upper bound (i.e. $P_{U_{Max}}|_{opt}$ also defined in Section 2.1) that can be achieved by a subset of *configurations* within the complex *architecture* [10].

However, while the process outlined by Bubbar et al. in [10] can identify the power capture upper bound for a WEC *architecture*, it remains to illustrate how the process: (1) yields insight on how the WEC physical parameters must be changed, or tuned, across wave frequencies to achieve the upper bound, and (2) identifies technologies that can enact such tuning, also referred to as *geometry control* – a term formally introduced by Price [16].

1.2. Geometry control, PTO force control and WEC resonance

WEC devices modelled in the frequency domain are linear underdamped vibration systems comprising the linear mechanical elements of masses, springs, and dampers. These mechanical elements are defined by their mechanical impedance relations, and system topologies (i.e. arrangements of these mechanical elements) may be developed and analyzed using network synthesis methods [17]. In this way, the PTO is represented as a generalized complex impedance element. For the simplest form of a WEC, a single body point absorber, the maximum power capture occurs when the complex-conjugate PTO force control constraints are enforced [14,18,19]. Under complex-conjugate PTO force control, the single body point absorber enters into a resonant state with respect to the incoming wave excitation force. However, for an underdamped system, resonance alone does not guarantee that the global power capture upper bound is achieved. The resonant condition is rather a prerequisite: a WEC operating in a resonant state reveals a local optimal power production for a given set of WEC physical, or geometric, parameters. To attain the global upper bound on power capture, one must implement a feature set in the design that permits active WEC geometry control, and then ensure that the PTO parameters follow the geometric parameters according to the complex-conjugate constraints. This intrinsic rule was coined as the *master-slave relationship* by Bubbar et al. [10]. We note that discrete control methods such as latching [20–22] and declutching [23] may be used to perform the required intervention at the PTO, but are not considered in this work. A concise overview of these PTO force control methods can be found in Ringwood et al. [24].

As an example, consider a heave constrained single body point absorber with a PTO operating under complex-conjugate control. By definition, the PTO mechanical impedance is conjugately matched to the resistance and reactance of the floating body in heave. If a *geometry control* feature set is implemented that influences the heave mechanical impedance of the floating body, the PTO (slave) must adapt to the changes exhibited in the floating body (master) to maintain the complex-conjugate control conditions and maximize power capture [10]. Similar observations have been expressed by Garcia-Rosa and Ringwood through numerical simulation of WEC configurations [25]. To summarize, achieving the power capture upper bound requires that: (1) a WEC architecture contains a feature set implementing geometry control, (2) the PTO impedance is set according to the master-slave relationship at all frequencies of operation, and (3) the geometric parameters are selected to maximize power capture whilst the master-slave relationship is enforced, resulting in optimal geometry control.

1.3. Objectives

In this work, we use the power capture upper bound to build the rationale for a *Derived SRPA WEC Architecture* shown in Fig. 3a. The *Derived SRPA Architecture* is similar to a standard two-body SRPA in Fig. 3b, but includes a generic force source internal to the spar that provides the means to enact the required *geometry control*. This feature is similar to that used by Korde [26–28] and injects reactive power into the system to alter the velocity phase profile of the SRPA's two rigid bodies. This force source is one of a variety of schemes for enacting *geometry control* that have been proposed in literature, which include reaction masses [26–29], variable wetted geometry [30–34], variable fluid ballast [35], and negative spring technology [36,37]. The goal is to establish conditions on the geometric parameter, the generic force source reactance, that ensure optimal *geometry control*, demonstrate how a specific *Inertial Modulation* mechanism satisfies these conditions, and assess how that mechanism improves performance by expanding the otherwise narrow response bandwidth of the conventional SRPA [8]. *Inertia Modulation* schemes in SRPAs are not new, but have been restricted to methods that alter the physical [26,29,35] and/or added mass [30] of the device spar. For this work, we expand this definition to include mechanisms capable of manipulating the mechanical reactance of the spar.

To these ends, the manuscript is organized as follows. Section 2.1 briefly reviews the mechanical circuit framework and how the *master-slave relationship* is robustly enforced by exploiting the *canonical form*. Section 2.2 describes the mechanical element that will be core to the *Inertial Modulation* mechanism – the *inerter*. Section 3 presents the *Derived SRPA WEC Architecture* and the reduction of that *architecture* into the *canonical form*. Section 4 outlines the construction of the power capture upper bound for the *Derived SRPA WEC Architecture*, the identification of the necessary conditions on the force source reactance to achieve the upper bound, and concludes with a discussion of how the force source manipulates the *Effective Mass* of the spar. Section 5 provides the results of a numerical case study; the physical parameters of a 1:25 scaled two-body SRPA device first reported in [38] are adopted and the analytical predictions on performance are compared to tank test data. Then, the analytical developments are used to determine the performance improvements that can be realized through the implementation of an *inerter* based *Inertial Modulation* mechanism as applied to that specific SRPA design in a manner first proposed by Beatty et al. [39] using a flywheel mechanism internal to the spar. Finally, Section 6 will focus on discussions based on observations in the numerical case study of Section 5.

2. Theory

This section focuses on an overview of the mechanical circuit framework as applied to representing the dynamics of a WEC *architecture*, followed by exploiting the *canonical form* to enforce the *master-slave relationship* between the PTO force parameters and geometric parameters; and concludes with formally introducing *inerter* technology and its application to WEC converter design.

2.1. Mechanical circuit framework

The mechanical circuit framework allows WEC *architectures* of arbitrary complexity to be represented as a topology of linear mechanical impedance elements with terminals connected at common nodes. For a mathematical model of the heaving single body point absorber WEC *architecture* in Fig. 1, Falnes [14] identified that complex conjugate PTO force control is enabled when Eq. (1) is enforced on the PTO mechanical impedance, leading to optimal device motion described by Eq. (2), resulting in $P_{U_{Max}}$ in Eq. (3), for which the *master-slave relationship* is enforced giving the optimal power capture at a given wave frequency for a given set of geometric parameters [15,40]. Optimal *geometry control* is determined by further optimizing Eq. (3) via the geometric parameters defined in the excitation force ($\hat{F}_{PTO_{Clamp}}$) and the intrinsic impedance (Z_i)[15], yielding the power capture upper bound $P_{U_{Max}}|_{opt}$ [10].

$$Z_{PTO_{opt}} = Z_i^*, * \equiv \text{complex conjugate} \tag{1}$$

$$\hat{u}_{r_{opt}} = \frac{\hat{F}_{PTO_{Clamp}}}{2\Re e\{Z_i\}} \tag{2}$$

$$P_{U_{Max}} = \frac{|\hat{F}_{PTO_{Clamp}}|^2}{8\Re e\{Z_i\}} \tag{3}$$

For more complex heaving WEC architectures, once the mechanical circuit representation is established, application of Kirchhoff's [17,41] conservation laws and Thévenin's [17,42] equivalent circuit theorem can transform the circuit representation into a *canonical form* that is common to all WEC architectures. The technique is limited to linear frequency domain representations of the WEC dynamics, but within this limit it allows Falnes' impedance matching technique [15,40], which is based on the *canonical form*, to be applied to WECs of infinite topological complexity [10].

In this work, we use the mechanical circuit framework to determine the *canonical form* for the complex *Derived SRPA WEC Architecture* (defined in Section 3), for the basis of imposing the *master-slave relationship*, and analytically determining the power capture upper bound ($P_{U_{Max}}|_{opt}$) [10]. We note, alternative network based methods have also been proposed in literature with the goal of representing multi-physical WEC models [43–46].

2.2. The missing mechanical element — Inerter

In the analogous electrical domain, Bott and Duffin [47,48] proved that any arbitrary driving point impedance could be synthesized using a combination of inductors, capacitors, and resistors, as there are no topological limitations on how these elements are connected. The same conclusion does not hold for systems in the mechanical domain when only considering mass, spring, and damper elements as, fundamentally, mass elements require one terminal referenced to ground to ensure an inertial reference frame for Newton's Second Law to hold [17,48].WECs modeled with these standard mechanical elements establish the intrinsic impedance (Z_i), while the PTO impedance (Z_{PTO}) is set from Eq. (1) to ensure device resonance. Now, add in *geometry control*, which maximizes the power capture by altering Z_i at each frequency, and we can appreciate the complexity of the *master-slave relationship*. Further, since Z_i and Z_{PTO} are both driving point impedances, their operating ranges are limited when only considering the mechanical mass, spring, and damper elements, yielding additional complexity.

This limitation was resolved with the introduction of the *inerter* by Smith [48], as the true mechanical analog to the electronic capacitor, and subsequently labelled as "the missing mechanical circuit element" [49]. Ideal *inerters* are described as a linear two terminal mechanical impedance element that apply an opposing reaction force proportional to the difference in acceleration as measured at the device terminals. The proportionality constant, known as the *inertance*, has SI units of kilograms, and is denoted as m_{eff} in this work. *Inerters* physically operate by converting the relative translating motion measured at the device terminals into rotating motion of a flywheel using an appropriate power transmission mechanism as seen in Fig. 2.

Fig. 2 illustrates the function of an *inerter*. The pinion and flywheel are constrained to move with terminal 1, while the rack is secured to terminal 2. The flywheel only rotates when there is relative motion between terminal 1 and terminal 2. Assuming there is relative motion between the terminals, the rack drives the pinion gear, which drives the flywheel. The reaction force exerted by the *inerter* is proportional to both the gear ratio between the pinion and flywheel, and the moment of inertia of the flywheel. If we consider terminal 1 and terminal 2 oscillating out of phase at the same frequency, the flywheel acts as a temporary storage device for mechanical energy, and thus is capable of influencing the relative phase of motion measured between the terminals.

In general, the *inertance* of a device can be calculated as the product of the transmission ratio squared (β^2) with the moment of inertia of the flywheel (J) as described in Eq. (4) below [50]. Devices which manipulate the *inertance* online do so by either varying the transmission ratio (β) or the moment of inertia (J) of the flywheel, and are collectively known as semi-active *inerters* [51].

$$m_{eff} = \beta^2 J \tag{4}$$

For an underdamped, sinusoidally excited vibration system, the *inerter* induces a phase delay between the reaction force and the relative translational velocity as measured through and across its terminals respectively, similar to a mass element. Currently three *inerter* concepts exist: (1) rack-and-pinion [48], (2) reverse-driven ball screw [49], and (3) hydraulic [52], for which the physical embodiment of β varies with each design. The *inerter* is represented in the mechanical circuit framework as a flywheel with the frequency domain constitutive equation described in Table 1 below [48].

By introducing the *inerter* element in partnership with spring and damping elements into the spar design, then any sinusoidal reaction force source signal can be replicated by this passive mechanical network. In this work, we will configure the *Derived SRPA WEC Architecture* with an *inerter* device to approximate the force source reactance

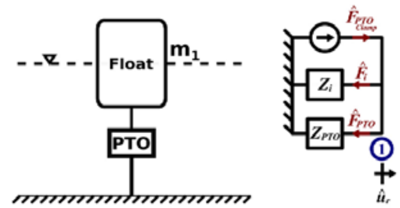

Fig. 1. Single body point absorber. (a) Mechanical schematic; (b) mechanical circuit.

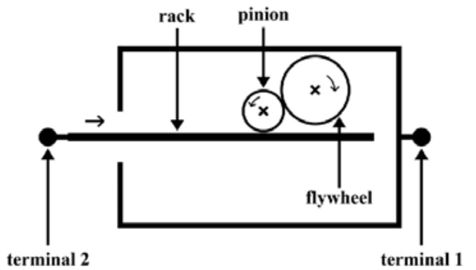

Fig. 2. Schematic of a Rack-and-Pinon Mechanical Inerter. Adapted from Smith [48].

Table 1
Mechanical circuit element for the inerter.

Element description	Circuit element	Constitutive equation
Inerter	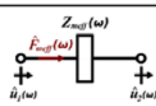	$Z_{meff}(\omega, m_{eff}) = i\omega m_{eff}(\omega)$ $\hat{F}_{meff}(\omega) = Z_{meff}(\omega)[\hat{u}_1(\omega) - \hat{u}_2(\omega)]$

required for enacting *geometry control*. If the *inertance* is selected optimally, we will achieve the power capture upper bound ($P_{U_{Max}}|_{opt}$).

3. Derived SRPA WEC Architecture

We explore the influence of *geometry control* on the *Derived SRPA WEC Architecture* in Fig. 3a, through establishing a power capture expression ($P_{U_{Max}}$) subject to enforcing the *master-slave relationship*. Both *architectures* in Fig. 3 contain tunable reactive PTOs and, thus, are capable of operating in complex conjugate mode [15], while the spar in Fig. 3a contains, in addition, an internal suspended reaction mass. To compare the *Derived SRPA WEC Architecture* against an SRPA architecture without a geometry controllable feature set, we define Fig. 3b as the *Original SRPA WEC Architecture*.

We initially consider a reactive force source ($\hat{F}_{FS1}$), interfaced in between the reaction mass (m_3) and spar (m_2) in Fig. 3a, that can exert a: (1) constant force capable of suspending the reaction mass at the equilibrium travel position of the slider joint when the WEC is stationary; (2) superimposed unbounded monochromatic sinusoidal force at the excitation frequency of the ocean wave. This sinusoidal force is proportional to the relative complex amplitude velocity difference ($\hat{u}_2 - \hat{u}_3$) measured between the spar and reaction mass, as described mathematically by Eq. (5).

$$\hat{F}_{FS1} = Z_{FS1}(\hat{u}_2 - \hat{u}_3) \tag{5}$$

Using the method proposed by Korde [26], the resulting force may be characterized by the following generalized impedance in Eq. (6), which is controlled by the reactive parameter X_{FS1}.

$$Z_{FS1} = iX_{FS1} \tag{6}$$

The role of the force source is to maximize the power captured by the PTO through influencing the dynamics of the spar, leading to $P_{U_{Max}}|_{opt}$. In achieving this state, we are interested in both the power capture response, as well as the requirements on the force source.

We choose an SRPA design for which the coupled radiation forces are known to be negligible (cf. Appendix E [53]). This WEC *architecture* may be considered a hybrid of Falnes' SRPA [15] combined with a reaction mass system similar to Korde [26,28], and French [29] contained within the semi-submerged spar.

The procedure for analytically determining $P_{U_{Max}}$ follows by: (1) generating the mechanical circuit for the WEC *architecture* as in Fig. 4a; (2) simplifying this *architecture* through application of parallel || and series ($\multimap$) circuit operations [17] resulting in Fig. 4b; (3) Determining $\hat{u}_{r_{Free}}$, $\hat{F}_{PTO_{Clamp}}$, and deriving Z_i for this *architecture* using the circuits from Fig. 5 and, thus, morphing the system into the *canonical form*, of Fig. 4c that is analogous to the single body point absorber represented in Fig. 1a; (4) Enforcing the *master-slave relationship* to analytically determine $P_{U_{Max}}$ by substituting Z_i and $\hat{F}_{PTO_{Clamp}}$ into Eq. (3).

Execution of steps (1) and (2) on the *Derived SRPA WEC Architecture* serves to generate the mechanical circuit and simplify it by defining two new lumped impedance terms Eqs. (7) and (8), representing the equivalent float (Z_{eq1}) and spar (Z_{eq2}) impedances respectively.

$$Z_{eq1} = Z_{m1} || Z_{A11} || Z_{B11} || Z_{K1} = Z_{m1} + Z_{A11} + Z_{B11} + Z_{K1} \tag{7}$$

$$\begin{aligned} Z_{eq2} &= (Z_{m2} \,||\, Z_{A22} \,||\, Z_{B22} \,||\, Z_{K2}) \,||\, (Z_{FS1} \multimap Z_{m3}) \\ &= Z_{m2} + Z_{A22} + Z_{B22} + Z_{K2} + \frac{Z_{m3} Z_{FS1}}{Z_{m3} + Z_{FS1}} \end{aligned} \tag{8}$$

We execute step (3) by first augmenting the mechanical circuit of Fig. 4b with two new circuits: (1) a case of free relative velocity between the float and spar developed when the PTO impedance is eliminated, and (2) a case of a PTO clamped through force developed when the PTO rigidly secures the float to the spar as seen in Fig. 5 [10,17].

We note the simplified circuits of Fig. 5 are the same topology as previously derived by Bubbar et al. [10] with the coupled radiation impedance set to zero ($Z_C = 0$). As such, equations representing both $\hat{F}_{PTO_{Clamp}}$, and Z_i can be supplied from that original work as Eqs. (9) and (10) [cf. Eqs. (19) and (20) [10]].

$$\hat{F}_{PTO_{Clamp}} = \frac{\hat{F}_{ex1} Z_{eq2} - \hat{F}_{ex2} Z_{eq1}}{Z_{eq1} + Z_{eq2}} \tag{9}$$

$$Z_i = \frac{Z_{eq1} Z_{eq2}}{Z_{eq1} + Z_{eq2}} \tag{10}$$

Fig. 4c depicts the ensuing circuit representation of the *canonical form* with the single body WEC connected in parallel with the PTO load and the PTO clamped through force embodying the equivalent excitation force.

To determine an expression for $P_{U_{Max}}$, we substitute Eqs. (9) and (10) into Eq. (3) yielding Eq. (11).

$$P_{U_{Max}} = \frac{|\hat{F}_{ex1} Z_{eq2} - \hat{F}_{ex2} Z_{eq1}|^2}{8[Z_{B11}|Z_{eq2}|^2 + Z_{B22}|Z_{eq1}|^2]} \tag{11}$$

It is important to emphasize that in forming Eq. (11) we have explicitly assumed in Eq. (6) that Z_{FS1} is a purely reactive impedance (i.e. $\Re e$ {Eq. (8)} $= Z_{B22}$) as this will be important in the power capture analysis of Section 4. We now utilize expressions Eqs. (8) and (11) to explore the conditions for optimal *geometry control* and, thus, search for the power capture upper bound $P_{U_{Max}}|_{opt}$ for this *Derived SRPA WEC*

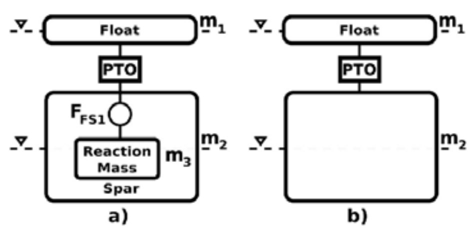

Fig. 3. Mechanical schematics for the: (a) Derived SRPA WEC architecture, (b) original SRPA WEC architecture.

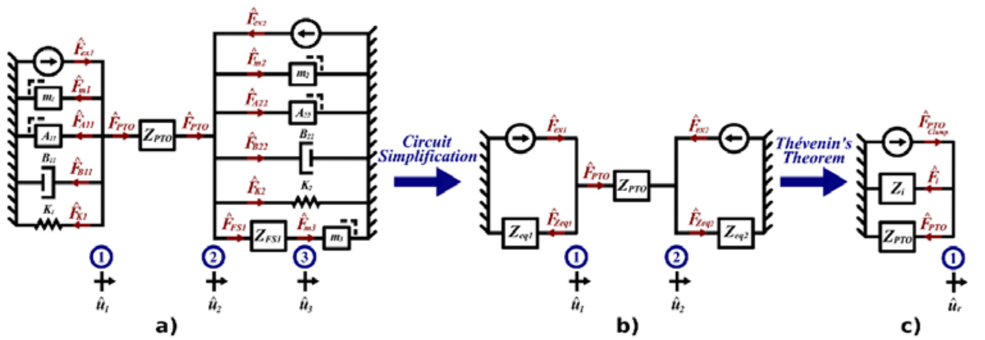

Fig. 4. Mechanical circuits for derived SRPA device: (a) Full circuit; (b) simplified circuit; (c) WEC canonical form.

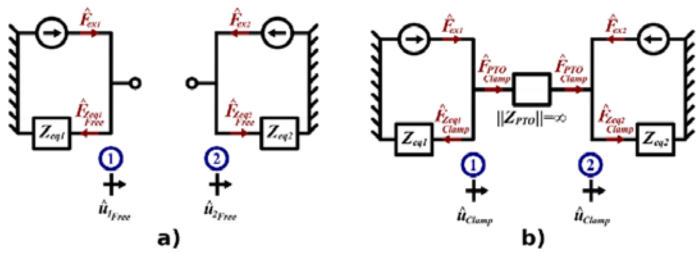

Fig. 5. Solving for the Thévenin equivalent system. (a) Free relative velocity; (b) clamped through force.

Architecture.

4. Analysis of power capture performance

Having established a power capture expression in Eq. (11), which robustly enforces the *master–slave relationship*, the focus of this section is on: (1) determining an analytical expression of the power capture upper bound ($P_{U_{Max}}|_{opt}$) for this *architecture* subject to enforcing the *master-slave relationship*, while concurrently enacting optimal *geometry control*; (2) establishing the force source impedance necessary for optimal *geometry control* ($Z_{FS1_{opt}}$); (3) exploring how *Inertial Modulation* is enacted on the spar via the force source reactance (X_{FS1}).

4.1. Establishing the power capture upper bound ($P_{U_{Max}}|_{opt}$)

From Eq. (11), the power captured by the *Derived SRPA WEC Architecture* has an implicit dependency on Z_{eq2}. As such, we may search for $P_{U_{Max}}|_{opt}$ for this *architecture* through applying standard multivariate calculus optimization techniques on Eq. (11) to identify extrema, while recognizing that Z_{eq2} is directly influenced by X_{FS1} in Eq. (8). Focusing on the form of Z_{eq2} in Eq. (8), we note that choosing to enclose the reaction mass and reactive force source subsystems internal to the spar yields no direct interaction between these components and the surrounding fluid (see Fig. 3a). Thus, no mathematical correlation between the force source or the reaction mass and the spar hydrodynamic forces exist. Hence, the extrema of Eq. (11) with respect to Z_{FS1} may be located by satisfying Eq. (12), generated using the multivariate chain rule. Clearly, extrema conditions will exist if either partial differential in Eq. (12) is zero, while the other remains finite.

$$\frac{dP_{U_{Max}}}{dZ_{FS1}} = \left(\frac{\partial P_{U_{Max}}}{\partial Z_{eq2}}\right)\left(\frac{\partial Z_{eq2}}{\partial Z_{FS1}}\right) = 0 \tag{12}$$

We note that Eqs. (11) and (8) are functions of complex variables, and evaluating Eq. (12) will require the application of methods from the field of complex analysis. Rather, we choose to form a proxy real-valued optimization problem whose solution will provide insight into the optimal solution of the original problem in the complex domain.

In forming our proxy real-valued problem, we substitute: (1) real variables for all complex variables in equations Eqs. (8), (11), and (12); (2) parenthesis for all modulus operators in Eq. (11); yielding equations Eqs. (13)–(15), where the real-valued variables are represented in lower-case.

$$p_{U_{Max}} = \frac{(f_{ex1} z_{eq2} - f_{ex2} z_{eq1})^2}{8[z_{B11}(z_{eq2})^2 + z_{B22}(z_{eq1})^2]} \tag{13}$$

$$z_{eq2} = z_{m2} + z_{A22} + z_{B22} + z_{K2} + \frac{z_{m3} z_{FS1}}{z_{m3} + z_{FS1}} \tag{14}$$

$$\frac{dp_{U_{Max}}}{dz_{FS1}} = \left(\frac{\partial p_{U_{Max}}}{\partial z_{eq2}}\right)\left(\frac{\partial z_{eq2}}{\partial z_{FS1}}\right) = 0 \tag{15}$$

Our proxy real-valued optimization problem focuses on maximizing Eq. (13) subject to z_{FS1} in Eq. (14) and thus requires expanding the partial derivatives in Eq. (15). Exploring the latter partial differential in Eq. (15), we determine Eq. (16) using Eq. (14), and acknowledge that Eq. (16) is only satisfied when $z_{m3} = 0$, which requires $Z_{m3} = 0$ in our original problem in Eq. (8), and, therefore, invalidates the SRPA design.

$$\frac{\partial z_{eq2}}{\partial z_{FS1}} = \frac{z_{m3}}{z_{FS1} + z_{m3}} - \frac{z_{FS1} z_{m3}}{(z_{FS1} + z_{m3})^2} = 0 \tag{16}$$

Hence, we conclude the extrema of Eq. (13) must satisfy the former partial differential in Eq. (15) identified by computing Eq. (17).

$$\frac{\partial p_{U_{Max}}}{\partial z_{eq2}} = 0 \tag{17}$$

We substitute Eq. (13) into Eq. (17), and analytically solve for the values of z_{eq2} satisfying this equation. Two solutions are revealed, and we now consider these solutions Eqs. (18) and (19) independently.

$$^{(1)}z_{eq2} = \frac{f_{ex2}\, z_{eq1}}{f_{ex1}} \tag{18}$$

$$^{(2)}z_{eq2} = -\frac{f_{ex1}\, z_{B22}\, z_{eq1}}{f_{ex2}\, z_{B11}} \tag{19}$$

To identify which condition results in a maxima, we back substitute each into Eq. (13). Substituting Eq. (18) into Eq. (13) results in $p_{U_{Max}}(^{(1)}z_{eq2}) = 0$ and, thus, we note Eq. (18) is the condition for a local minima. Since Eq. (13) is a continuous function, we can conclude Eq. (19) represents the optimal condition $(z_{eq2_{opt}} = {}^{(2)}z_{eq2})$ for maximizing Eq. (13). By substituting Eq. (19) into Eq. (13), the global optimum of Eq. (13) is analytically determined as Eq. (20).

$$p_{U_{Max}}(z_{eq2_{opt}}) = \frac{(f_{ex1})^2}{8z_{B11}} + \frac{(f_{ex2})^2}{8z_{B22}} \tag{20}$$

To replicate the results of our proxy real-valued problem in the original complex-valued problem we: (1) replace all real-valued variables back with their complex-valued counterparts; (2) replace the complex phasors $\widehat{F}_{ex1}$ and $\widehat{F}_{ex2}$ with their complex conjugates $\widehat{F}^*_{ex1}$ and $\widehat{F}^*_{ex2}$. These substitutions result in Eqs. (21)–(24) below, where Eq. (21) represents the equivalent spar impedance for null power capture and will be revisited in Section 6.2. Eq. (24) is the analytical power capture upper bound for the *Derived SRPA WEC Architecture* transpiring when both complex conjugate PTO force control is enabled via enforcing the *master-slave relationship*, and optimal *geometry control* is simultaneously enabled via satisfying Eq. (22).

$$Z_{eq2_{min}} = \frac{\widehat{F}^*_{ex2} Z_{eq1}}{\widehat{F}^*_{ex1}} \tag{21}$$

$$Z_{eq2_{opt}} = -\frac{\widehat{F}^*_{ex1} Z_{B22} Z_{eq1}}{\widehat{F}^*_{ex2} Z_{B11}} \tag{22}$$

$$P_{U_{Max}}(Z_{eq2_{min}}) = 0 \tag{23}$$

$$P_{U_{Max}}(Z_{eq2_{opt}}) = P_{U_{Max}}|_{opt} = \frac{|\widehat{F}_{ex1}|^2}{8Z_{B11}} + \frac{|\widehat{F}_{ex2}|^2}{8Z_{B22}} \tag{24}$$

In comparing Eq. (24) with Falnes' seminal result on optimal power capture of single body heaving point absorbers [40], we can deduce the upper bound on power capture for the *Derived SRPA WEC Architecture* is equivalent to the sum of two single body heaving point absorbers comprising the float and spar respectively, operating in the presence of one another, with each absorber independently enacting optimal complex conjugate PTO force control, as depicted in Fig. 6 below. Such a result makes intuitive sense, and to the authors' knowledge, this is the first instance of its publication.

With the upper bound established for the *Derived SPRA WEC Architecture*, we also identify that Eq. (22) represents generic design insight relating the optimal impedance ratio of the equivalent float and spar required to achieve Eq. (24). In Section 4.2 we explore the feasibility in achieving Eq. (22) via the force source.

4.2. Determining the optimal force source impedance ($Z_{FS1_{opt}}$)

To achieve the power capture upper bound in Eq. (24) with the *Derived SRPA WEC Architecture*, we have proposed that Eq. (22) must be satisfied. As noted in Section 3, Z_{FS1} is our control variable used to satisfy Eq. (22). We note that Eq. (8) is a constraint equation expressing the relationship between Z_{eq2} and Z_{FS1} for the *Derived SRPA WEC Architecture*, thus, applying Eq. (22) into Eq. (8) yields Eq. (25).

$$Z_{m2} + Z_{A22} + Z_{B22} + Z_{K2} + \frac{Z_{m3} Z_{FS1}}{Z_{m3} + Z_{FS1}} - Z_{eq2_{opt}} = 0 \tag{25}$$

To simplify the resulting expression, we lump the mass and all the hydrodynamics impedances of the spar into a single term defined by Eq. (26), and solve for $Z_{FS1_{opt}}$ as in Eq. (27).

$$Z_{mH2} = Z_{m2} + Z_{A22} + Z_{B22} + Z_{K2} \tag{26}$$

$$Z_{FS1_{opt}} = \frac{Z_{m3}(Z_{eq2_{opt}} - Z_{mH2})}{Z_{m3} + Z_{mH2} - Z_{eq2_{opt}}} = R_{FS1_{opt}} + iX_{FS1_{opt}} \tag{27}$$

We note that Eq. (27) is in fact decomposed into two different equalities through equating both the real and imaginary terms, as expressed in Eq. (28) and Eq. (29). In pragmatic language, both Eqs. (28) and (29) must be satisfied simultaneously by our force source to achieve Eq. (24).

$$R_{FS1_{opt}} = \Re e\left\{\frac{Z_{m3}(Z_{eq2_{opt}} - Z_{mH2})}{Z_{m3} + Z_{mH2} - Z_{eq2_{opt}}}\right\} \tag{28}$$

$$X_{FS1_{opt}} = \Im m\left\{\frac{Z_{m3}(Z_{eq2_{opt}} - Z_{mH2})}{Z_{m3} + Z_{mH2} - Z_{eq2_{opt}}}\right\} \tag{29}$$

In Section 3, we made a conscious decision in Eq. (6) to assume Z_{FS1} is a reactive impedance. This choice necessitates that Eq. (28) is only satisfied at wave excitation frequencies for which $R_{FS1_{opt}} = 0$ in Eq. (28), as there is no means to adjust the optimal force source resistance in the *Derived SRPA WEC Architecture*. This clearly introduces a challenge in achieving Eq. (24) using the *Derived SRPA WEC Architecture*. We, therefore, require a SRPA WEC *configuration* that is insensitive to satisfying Eq. (28), while still capturing $P_{U_{Max}}|_{opt}$ for a target wave frequency bandwidth. We demonstrate one WEC *configuration* satisfying this criteria using numerical analysis in Section 5.1.

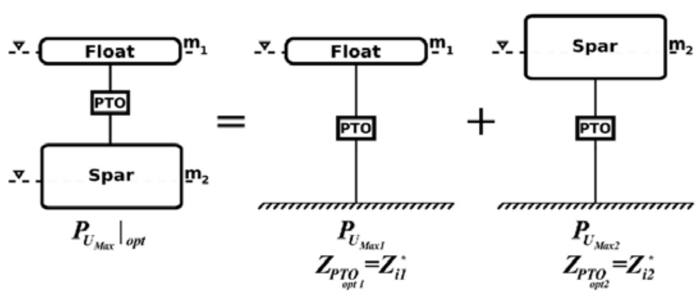

Fig. 6. Conceptual representation of the optimal power capture expression Eq. (24) for the *Derived SRPA Architecture*.

We also explicitly note, in deriving Eq. (29), we have not specified how this optimal force source reactance is realized in physical form. Thus, Eq. (29) represents a constraint equation for the design of the reactive force source, which is realized through substitution of an appropriate network of linear mechanical components. In Section 5, we propose and perform an analysis on one possible network that satisfies Eq. (29) using *inerter* technology.

4.3. Inertial modulation of the spar

The focus of this section is to establish how the force source reactance (X_{FS1}) manipulates the *Effective Mass* of the spar, and, thus, prove that the *Derived SRPA WEC Architecture* satisfying Eq. (29) enacts *Inertial Modulation*. From Eq. (8), we observe Z_{eq2} is manipulated by the unbounded force source reactance via X_{FS1}. This force source can only influence the last term in Eq. (8), which is purely reactive. We assign this term plus the mechanical impedance contributed by the spar's actual mass as a new lump sum reactance, X_{EM}, representing the spar *Effective Mass* (EM) in Eq. (30), and focus our attention on determining its operating range.

$$X_{EM} = X_{m2} + \frac{X_{m3}X_{FS1}}{X_{m3} + X_{FS1}} \tag{30}$$

As the reactance of the force source is unbounded, the resulting operational range of X_{EM} may be established by analyzing the following analytical limits in Eqs. (31) and (32).

$$\lim_{X_{FS1}\to+\infty} X_{EM} = \lim_{X_{FS1}\to-\infty} X_{EM} = X_{m2} + X_{m3} \tag{31}$$

$$\lim_{X_{FS1}\to-X_{m3}^-} X_{EM} = +\infty \text{and} \lim_{X_{FS1}\to-X_{m3}^+} X_{EM} = -\infty \tag{32}$$

The limits in Eq. (31) establish a horizontal asymptote for which $X_{EM} \to X_{m2} + X_{m3}$ and, thus, the physical effect on the *Effective Mass* is to fuse the reaction mass with the mass of the spar resulting in a single body spar. The limits in Eq. (32) establish a vertical asymptote at $X_{FS1} = -X_{m3}$ for which the right and left approaching limits tend to positive and negative infinity respectively. Fig. 7 describes the relationship between X_{EM} and X_{FS1}, which must be satisfied at any given frequency ω, and highlights two distinct regions of operation discussed in further detail below.

Region 1:

In Region 1, the *Effective Mass* of the spar ranges from the fused condition to infinity as $X_{FS1} \to -X_{m3}^-$ leading to the operating range in this region as described by Eq. (33) below.

$$(X_{m2} + X_{m3}) < X_{EM} < +\infty \text{for} -\infty < X_{FS1} < -X_{m3} \tag{33}$$

Region 2:

In Region 2, the *Effective Mass* of the spar ranges from negative infinity, as $X_{FS1} \to -X_{m3}^+$ to the fused condition as $X_{FS1} \to +\infty$, leading to the operating range in this region described by Eq. (34) below.

$$-\infty < X_{EM} < (X_{m2} + X_{m3}) \text{for} -X_{m3} < X_{FS1} < +\infty \tag{34}$$

Hence, from the analysis of both Region 1 and Region 2, the reactive force source, through adjusting X_{FS1}, has the physical effect of modulating the *Effective Mass* of the equivalent spar and, thus, enacts *Inertial Modulation*. This is significant as the spar dynamics are manipulated as if the spar mass changes, all the while, the physical mass of the spar remains constant.

5. Numerical examples of SRPA configurations

Having derived both the power capture upper bound, $(P_{U_{Max}}|_{opt})$ in Eq. (24), and the optimal force source impedance, $(Z_{FS1_{opt}})$ in Eq. (27), to enact the upper bound, the following section focuses on exemplifying these design insights using both numerical and experimental examples; while concurrently demonstrating how the reactive force source can be replaced by a parallel combination of a spring and a semi-active *inerter*. In particular, we utilize parameters from a SRPA physical 1/25th Froude-scaled model published by Beatty et al. (cf. WEC A [38,53]). This physical model may be classified as the *Original SRPA WEC Architecture* of Fig. 3b and resembles a WaveBOB™ device detailed in Fig. 12 of Appendix A. We note Beatty et al.'s SRPA model was not designed to satisfy Eq. (28) in the target wave excitation frequency range. We substitute the physical parameters of Beatty's device verbatim into Eqs. (3), (7)–(10) and thus create the *Original SRPA WEC Configuration*. We note that the last term in Eq. (8) is eliminated as there is no *Inertial Modulation* feature set in this architecture.Using the same process we create a second configuration, the *Derived SRPA WEC Configuration*, based on the *Derived SRPA WEC Architecture* of Fig. 3a by substituting all of these model parameters verbatim into Eqs. (3), (7)–(10). As this *architecture* does contain a reaction mass feature set, the last term in Eq. (8) remains, requiring us to define a value for the reaction mass (m_3). To ensure the total mass contained within the *Original SRPA WEC Configuration* and the *Derived SRPA WEC Configuration* are equal, we choose to set the sum of the masses m_2 and m_3 in the *Derived SRPA WEC Configuration* equal to the spar mass in the *Original SRPA WEC Configuration* following $m_2 = m_3 = 57.5$ kg. For simplicity, we assume m_3 is a point mass, and interface it in series with our force source, which provides a gravity offsetting constant force, to place m_3 at approximately the centre of travel inside the spar canister. We note the *Original SRPA WEC Configuration* and the *Derived SRPA WEC Configuration* exhibit the exact same linear hydrodynamic frequency response and contain the same total mass.

Numerical models are developed for both the *Original SRPA WEC Configuration* and the *Derived SRPA WEC Configuration*. We generate numerical results for the power capture, the associated optimal force source reactance, or *inertance*, and the optimal PTO impedance for the *Derived SRPA WEC Configuration*, and explore the inclusion of motion constraints between the float and spar for both the *Original SRPA WEC Configuration* and the *Derived SRPA WEC Configuration*. Finally, we compare these numerical results against data obtained from experimental trials. Discussion on these results will follow in Section 6.

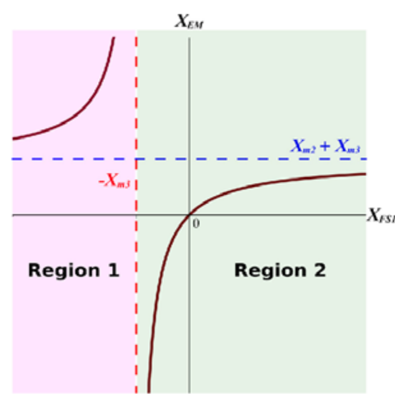

Fig. 7. Plot describing the relationship between X_{EM} and X_{FS1} at a singular angular frequency ω.

5.1. Power capture example

We generate power capture data using the *Derived SRPA WEC Configuration* displayed in Figs. 8 and 9 with power capture normalized to a unit wave amplitude squared. To illustrate the insensitivity of R_{FS1} on power capture on the current SRPA *configuration*, in Fig. 8a, we plot useful power capture via Eq. (11) as a function of excitation frequency parametrized by $R_{FS1} = [0, 0.5R_{FS1_{opt}}, R_{FS1_{opt}}]$ while concurrently satisfying $X_{FS1_{opt}}$ via Eq. (29). We observe that the useful power capture under all three conditions of R_{FS1} are coincident. We further explore the influence of R_{FS1}, through Fig. 8b, by plotting the optimal PTO resistance $(R_{PTO_{opt}})$ and reactance $(X_{PTO_{opt}})$, via substitution of Eq. (10) into Eq. (1), under the same parameterizations of R_{FS1}. We observe that $R_{PTO_{opt}}$ varies with each setting of R_{FS1}, while $X_{PTO_{opt}}$ remains unchanged. This insensitivity of $X_{PTO_{opt}}$ to R_{FS1} is a natural property of this SRPA *configuration*, within this operating frequency range, and is not discernable when exploring the complexity of Eq. (8) substituted into Eq. (10). Finally, we plot $P_{U_{Max}}|_{opt}$ via Eq. (24) in Fig. 8a, and observe that $P_{U_{Max}}|_{opt}$ is coincident with the useful power plots generated under varying R_{FS1}. Hence, this *Derived SRPA WEC Configuration* is theoretically capable of operating at $P_{U_{Max}}|_{opt}$ for the frequency range of $\omega = [1.5, 4] rad/s$ while $R_{FS1} = 0$ as in Eq. (35), and is therefore neglected.

$$Z_{FS1_{opt}} = iX_{FS1_{opt}} \tag{35}$$

Thus, we implement Eq. (35) on the force source impedance in all subsequent analyses.

5.2. Stroke limit constraints

An inherent weakness of Section 5.1 is the exclusion of stroke limitations on the relative motion of the rigid bodies. Stroke limitations between the float and spar may be included in the power capture analysis through application of Eq. (36), originally derived by Evans [54]. Eq. (36) enforces the stroke constraint when the ratio of the bounded to unbounded relative displacement amplitude (δ) between the float and spar is less than one; implemented by detuning the PTO resistance.

$$P_U^C(\omega, \delta) = P_U(\omega)[1-(1-\delta)^2 Heaviside(1-\delta)] \tag{36}$$

We note Evans derived Eq. (36) for a single mode heaving point absorber. However, Eq. (36) may also be applied to a multi-mode WEC, as these devices can be topologically represented in a *canonical form* [10]. Falnes used the same argument to derive an equivalent equation for SRPA devices (cf. Eq. (40) [15]). Here, the *Derived SRPA WEC Architecture* is a device with two relative displacements between the: (1) float and spar, and (2) spar and reaction mass. Both methods (Evans or Falnes) are unable to consider the relative displacement amplitude constraint between the spar and reaction mass, as this would require reformulating the optimization problem. In using Eq. (36), we acknowledge that this is a limitation in our study.

To assess the performance of the *Derived SRPA WEC Configuration* under motion constraints, we choose to compare power capture performance against the *Original SRPA WEC Configuration* under the same conditions. Using Eq. (36), the power capture plots in Fig. 9 are generated as follows: (a) *Original SRPA WEC Configuration* operating under optimal complex conjugate PTO force control with unbounded, 2.5 and 1 m relative displacement amplitude stroke limitations enforced respectively between the float and spar; (b) *Derived SRPA WEC Configuration* operating under simultaneous optimal complex conjugate PTO force control and geometry control.

As expected, results for the *Original SRPA WEC Configuration* mirror the work published by Beatty et al. [38,53]. For the *Derived SRPA WEC Configuration*, optimal PTO force control is enforced through application of equations Eqs. (1) and (10), and optimal *geometry control* is imposed though application of Eq. (35). For the *Original SRPA WEC Configuration*, optimal PTO force control is enforced through application of equations Eqs. (1) and (10) while eliminating the last term in Eq. (8) as discussed in Section 5. As a reference, we include a plot of the theoretical maximum (P_{rad}) representing the maximum power which may be absorbed by a heaving axisymmetric body in deep water [20,55,56].For both configurations, we observe a decimation of the useful power capture when stroke constraints are enforced. The magnitude of the decimation is larger in the *Derived SRPA WEC Configuration* relative to the *Original SRPA WEC Configuration*; however, the power capture performance of the *Derived SRPA WEC Configuration* at low excitation frequency is still an order of magnitude larger under the same constraints. The power capture of the *Original SRPA WEC Configuration* is only superior to the *Derived SRPA WEC Configuration* under the specific case of a 1 m stroke limitation in the excitation frequency range above 3.5 rad/s. Finally, in Fig. 9b we observe that $P_{U_{Max}}|_{opt}$ and P_{rad} are relatively consistent, however, $P_{U_{Max}}|_{opt}$ does slightly exceed the theoretical maximum above 2 rad/s. Technical discussion on these

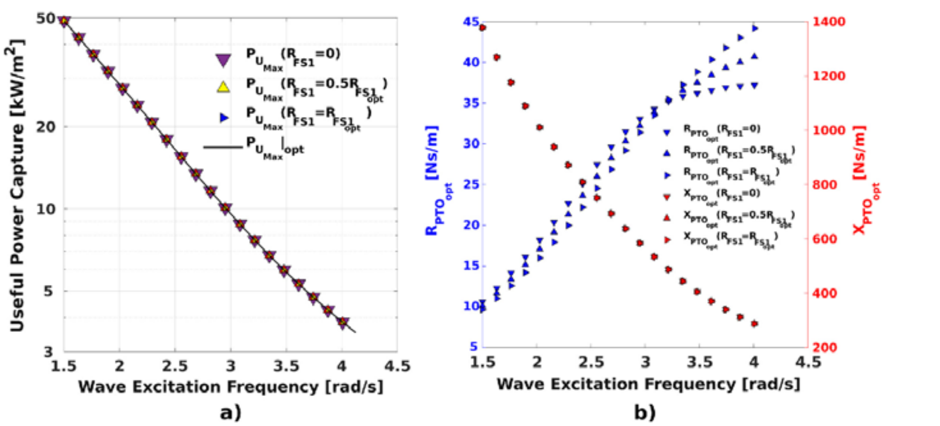

Fig. 8. (a) Semi-log plot of wave amplitude normalized power versus wave excitation frequency. (b) Dual axis plot of $R_{PTO_{opt}}$ (left) and $X_{PTO_{opt}}$ (right) both parameterized by R_{FS1}.

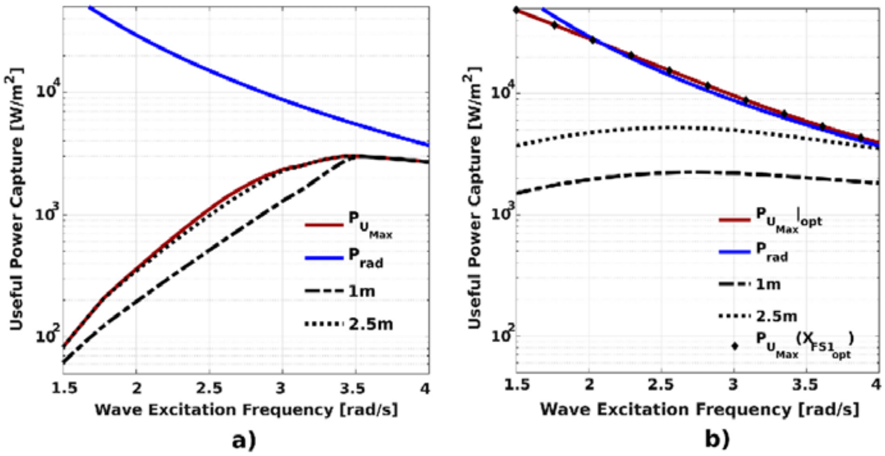

Fig. 9. Semi-log plot of normalized power versus wave excitation frequency. (a) Original SRPA WEC configuration, (b) derived SRPA WEC configuration.

observations are addressed in Section 6.1.2.

5.3. Comparison of numerical results with experimental data

This section focuses on quantifying how the power capture performance may be improved through the implementation of an *Inertial Modulation* mechanism. We compare the numerical results of the *Derived SRPA WEC Configuration*, the *Original SRPA WEC Configuration*, and data obtained from experimental trials of a physical 1/25 scaled model [38] for which these *configurations* are based. Our goal is to present the reader with an overview of the trade-offs a WEC designer may consider when attempting to leap up the power capture performance curves.

In Fig. 10, we observe four overlaid datasets classified in Table 2, based on the: (1) data source, (2) PTO control regime, and (3) *geometry control* regime. Dataset 1 is based upon experimental trials conducted by Beatty et al. [38] in a monochromatic wave regime utilizing a PTO simulator to generate the required linear PTO force response [57]. In these trials, the PTO force response is established by enforcing the amplitude control conditions [14] in Eq. (37), derived by Falnes [14], without a *geometry control* feature set implemented. Dataset 2 represents a numerical model of the *Original SRPA WEC Configuration* operating under the same PTO and *geometry control* regimes as the experimental trials. Dataset 3 represents a numerical model of the *Original SRPA WEC Configuration*, with the PTO set to operate under complex conjugate control based on Eq. (1), without a *geometry control* feature set implemented. Finally, Dataset 4 represents a numerical model of the *Derived SRPA WEC Configuration*, with both an optimal *geometry control* feature set implemented via *Inertial Modulation* based on Eq. (35), and a complex conjugate controlled PTO following the *master-slave relationship*.

As presented by Beatty et al. [38], there is good alignment of Dataset 1 and Dataset 2, and thus confidence in the linearized hydrodynamic and inertial parameters used in the numerical model. In all of these datasets, the hydrodynamic performance and total mass are the same; however, there are clear differences in predicted power capture. Discussion on these datasets are addressed in Section 6.1.3.

$$Z_{PTO} = |Z_i| \tag{37}$$

5.4. Implementing optimal geometry control using inerters

In developing the conditions for optimal *geometry control*, we had chosen to specify the *Derived SRPA WEC Architecture* with a reactive force source capable of adjusting its internal mechanical reactance (X_{FS1}) to an optimal value per excitation frequency. In reality, we used a reactive force source in the analysis as a generic means to derive the optimal force source reactance ($X_{FS1_{opt}}$). Having established $X_{FS1_{opt}}$, we now use Eq. (29) as a constraint equation to represent the target mechanical reactance for technology design. In Section 2.2, we introduced the *inerter* as a mechanical element capable of injecting positive mechanical reactance into a system, and we now choose to replace our reactive force source with a parallel combination of an *inerter* and spring. In performing this substitution, we note Eq. (38) represents the combined reactance of an *inerter* and spring in parallel, which must satisfy $X_{FS1_{opt}}$.

$$X_{FS1_{opt}} = \omega m_{eff} - \frac{k_s}{\omega} \tag{38}$$

By rearranging Eq. (38), we are able to solve for the inertance $m_{eff_{opt}}$ required to enact optimal geometry control as Eq. (39).

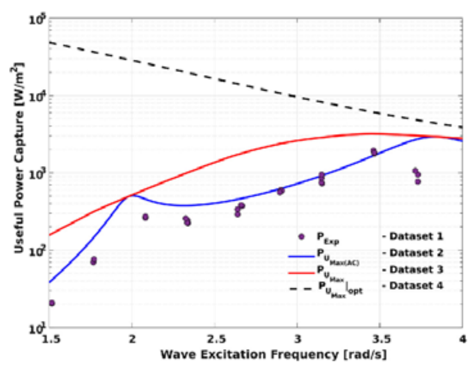

Fig. 10. Power capture of SRPA models under various control regimes [38].

Table 2
Overview of power capture datasets presented in Fig. 10.

Dataset	Identifier	Data source	PTO control regime	Geometry control regime
1	P_{Exp}	Experimental Trials	Linear Amplitude Control	None
2	$P_{U_{Max(AC)}}$	Numerical Model	Linear Amplitude Control	None
3	$P_{U_{Max}}$	Numerical Model	Linear Complex Conjugate Control	None
4	$P_{U_{Max}}\|_{opt}$	Numerical Model	Linear Complex Conjugate Control	Optimal Inertial Modulation

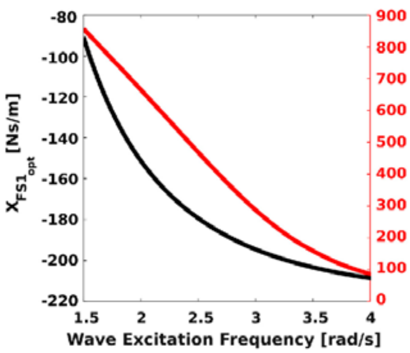

Fig. 11. Dual axis plot of left: $X_{FS1_{opt}}$, right: $m_{eff_{opt}}$ versus wave excitation frequency.

$$m_{eff_{opt}} = \frac{X_{FS1_{opt}}}{\omega} + \frac{k_3}{\omega^2} \tag{39}$$

For our model, we specify a spring stiffness of $k_3 = 2000$ N/m, to offset the gravitational force and maintain m_3 at approximately the centre of travel inside the spar canister. With k_3 specified, Fig. 11 is generated as a dual axis plot of $X_{FS1_{opt}}$ and $m_{eff_{opt}}$ versus wave excitation frequency. Observation of Fig. 11 informs us a semi-active *inerter* with an operating range of $m_{eff} = [75, 850]$ kg would suffice. Such parameter constraints are well within a feasible range for physical design [50].

6. Discussion

This section examines a few major implications of the results presented in Sections 4 and 5, including important observations stemming from Figs. 8–11. Section 6.1 reviews the observations from numerical and experimental plots in Section 5, Section 6.2 reviews the consequence of the null power capture result derived in Eq. (21), and finally Section 6.3 assesses the generic approach of using the mechanical circuit framework in conjunction with unbounded force sources for exploring innovative technologies to enact optimal *geometry control*.

6.1. Power capture analysis

6.1.1. Numerical validation of the power capture bound $P_{U_{Max}}|_{opt}$

We begin by reviewing observations from Fig. 8. As discussed in Section 5.1, both the useful power capture and $X_{PTO_{opt}}$ are invariant to R_{FS1}. In addition, our plot of $P_{U_{Max}}|_{opt}$ is coincident with the power capture plots generated under varying R_{FS1}. This leads to three important conclusions for this *Derived SRPA configuration*: (1) $P_{U_{Max}}|_{opt}$ is insensitive to R_{FS1}, provided X_{FS1} is set optimally and the *master-slave relationship* is enforced and, thus, we are permitted to omit R_{FS1} from our model of this *configuration* without consequence to the power capture. This insensitivity to R_{FS1} eliminates the need to inject real power into the WEC to achieve $P_{U_{Max}}|_{opt}$ and, therefore, does not implicitly erode the net power capture performance. There is, however, a caveat: in Fig. 8b, $R_{PTO_{opt}}$ varies with R_{FS1}, as $R_{PTO_{opt}}$ was required to compensate for the varying spar resistance due to enforcing the *master-slave relationship*. Theoretically, this is only acceptable provided $R_{PTO_{opt}} > 0$, or else real power must be injected into the WEC through the PTO, deteriorating the net power capture performance. This is not the case in Fig. 8b within our chosen wave excitation frequency range. (2) The focus in attaining $P_{U_{Max}}|_{opt}$ turns to selecting a technology that can achieve the required force source reactance ($X_{FS1_{opt}}$) in Eq. (29). In essence, $X_{FS1_{opt}}$ becomes an objective metric to evaluate technology choices, and thus provides invaluable generic design guidance. (3) Our proposed method for analytically deriving $P_{U_{Max}}|_{opt}$ for this *Derived SRPA WEC Architecture* via the proxy real-valued formulation is consistent with numerical observations of the true optimization problem in the complex domain. Numerical validation is demonstrated as $P_{U_{Max}}|_{opt}$ in Eq. (24) and P_U operating under optimal PTO force control via Eq. (1) and optimal geometry control via Eq. (35) are coincident. Our result for $P_{U_{Max}}|_{opt}$ is also observed to be generally consistent with the theoretical maximum (P_{rad}) [20,55,56].

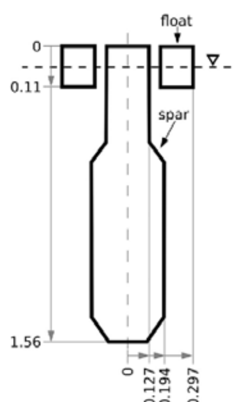

Fig. 12. Simplified cross-sectional drawing of the original SRPA WEC configuration. Adapted from Beatty et al. [38] Callouts in Metres.

Table 3
Overview of inertial and hydrodynamic parameters of the 1/25 WEC model. Adapted from Beatty et al. [38].

Parameter	Value	Units
Float		
Outer diameter	0.595	m
Inner diameter	0.317	m
Hydrostatic stiffness	2000	N/m
Physical mass	12	kg
Radiation damping (min, max)	8.90, 59.6	Ns/m
Added mass (min, max)	27.6, 32.7	kg
Excitation force (min, max)	1290, 1850	N/m
Spar		
Hydrostatic stiffness	509.5	N/m
Physical mass	115	kg
Total damping (min, max)	39.74, 69.13	Ns/m
Added mass (min, max)	64.22, 67.81	kg
Excitation force (min, max)	16.00, 337.5	N/m

6.1.2. Power capture analysis under stroke constraints

Next, we explore the influence of motion constraints on power capture by reviewing observations from Fig. 9 detailed in Section 5.2: (1) Enforcing relative travel constraints reduces the power capture limits at low wave excitation frequencies by several orders of magnitude, however, a substantial power capture improvement is still observed for the *Derived SRPA WEC Configuration* over the *Original SRPA WEC Configuration*. This power capture improvement provides a strong argument that significant power capture potential exists with the inclusion of an optimally set *Inertial Modulation* mechanism even under stroke limitations. (2) Situations arise for which the *Original SRPA WEC Configuration* exhibits improved power capture over the *Derived SRPA WEC Configuration* explained by the following two considerations. First, the *master-slave relationship* is broken when engaging travel constraints as R_{PTO} is set to enforce the motion amplitude. Second, the optimal geometry control setting in Eq. (27) is derived under the assumption of no motion constraints and, thus, $X_{FS1_{opt}}$ determined using Eq. (29) is presumably suboptimal under motion constraints. Analytically determining $X_{FS1_{opt}}$ under motion constraints between both the float and spar, and the spar and reaction mass would require: (i) reformulating the optimization problem described in Section 1.3, (ii) including a resistive force source term R_{FS1} to modulate the spar and reaction mass travel. (3) $P_{U_{Max}}|_{opt}$ for the *Derived SRPA WEC Configuration* exceeds P_{rad} at certain wave excitation frequencies. Theoretically this is not feasible, and is likely due to the integrity of the hydrodynamic coefficients as also experienced by Korde [27].

6.1.3. Comparing the power capture upper bound with experimental data

The curves in Fig. 10 present an overview of: (1) the relationship between design complexity and improved power capture potential, and (2) an example of the current state of SRPA WEC power capture performance (P_{Exp}) in relation to the power capture potential in $P_{U_{Max}}|_{opt}$. Fig. 10 demonstrates to a WEC developer, the significant power capture improvements which may be realized as an SRPA design transits between the *configurations* corresponding to Datasets 2–4. This substantial gap, if even partially achieved through the implementation of simultaneous optimal PTO force control and optimal geometry control, will contribute towards viable techno-economics of wave energy conversion. However, we also recognize that closing this gap is accompanied by introducing sequential design complexity. The difference between Datasets 2 and 3 represent the added complexity of transitioning from a single function and purely resistive amplitude controlled PTO, to a dual function, resistive and reactively complex conjugate controlled PTO – a feature that has garnered much attention from wave energy researchers [14,36,43,58–60].

In contrast, the larger gap observed between Datasets 3 and 4 has received far less focus as it requires even further design complexity. Implementing the required control regime into the *Derived SRPA WEC Configuration* not only involves developing an adjustable *Inertial Modulation* mechanism, but requires first setting that *Inertial Modulation* mechanism according to Eq. (35) to achieve optimal *geometry control* based on the sea conditions. Once the optimal *geometry control* condition is realized, the intrinsic impedance of the WEC must be calculated via Eq. (10) to enforce complex conjugate PTO force control via Eq. (1). Although Dataset 4 is evaluated using $P_{U_{Max}}|_{opt}$ in Eq. (24), which is idealized due to both assumptions in linear theory, and the significant challenges of implementing true complex-conjugate control in a WEC device [24], the potential for improvement over Dataset 3 is vast and thus cannot be overlooked. In our opinion, based on the minute resource allocations required to explore this power capture versus complexity trade off at the conceptual development stage, we recommend considering this analysis on all early stage SRPA WEC designs as an input to establishing the TPL metric.

6.1.4. Using inerters to implement optimal geometry control

We discuss the choice made in Section 5.4 of a parallel combination of a semi-active *inerter* and a constant linear spring to deliver the reactance $X_{FS1_{opt}}$ required for optimal geometry control. Fig. 11 presents both $X_{FS1_{opt}}$ and $m_{eff_{opt}}$ as a function of wave excitation frequency for the *Derived SRPA WEC Configuration*. Although the range of $m_{eff_{opt}}$ appears large, Eq. (4) informs us the *inertance* is a quadratic function of the transmission ratio (β) and a linear function of the Moment of Inertia (J), which itself is a quadratic function of the radius of gyration of the rotating flywheel. We conclude that a large range of *inertance* is achievable through relatively small adjustments in either/both β or/and J. We contend that an *inerter*, with a large *inertance* range, is a feasible choice as a physical device used to implement optimal geometry control as also demonstrated by Hu et al. [50].

6.1.5. Limitations of the power capture upper bound

A major benefit of linear monochromatic WEC models is the low computation resources required to perform both dynamic analysis and design optimization. However, linear models present limitations, as they cannot account for non-linear physics and transient physical behaviour, both of which are attributes of a real physical WEC device operating in real seas. Two examples specific to the *Derived SRPA WEC Configuration* follow when considering the PTO and inerter systems.

To this point, we have assumed the PTO is a linear unbounded device capable of delivering the required force response to maintain the master-slave relationship and thus maximize power capture. Such a PTO serves to enact a dual function by: (1) injecting the appropriate reactive power to ensure resonance of the canonical form, and (2) providing a resistive force to act against the relative motion of the float and spar resulting in captured power. Simultaneous implementation of both of these PTO functions with a coupled inerter mechanism requires careful consideration of the ensuing consequences.

The WEC response resulting from the reactive forces of the inerter and PTO serve to maximize the power transferred from the ocean waves onto the WEC rigid bodies by increasing the relative displacement amplitudes between the float and spar. This kinetic power is captured as the relative motion of the float and spar do work against the PTO resistive force. With the increase in relative motion between the float and spar, combined with finite stroke limitations as presented in Section 5.2, the PTO compensates by increasing its internal resistance to both capture this additional available power and to prevent end stop collisions. This increase to the PTO force response must be considered a design requirement in the selection of a physical device to embody the PTO. Further, increases in the force response are also associated with non-linear power loss. As such true complex-conjugate control is often infeasible to achieve but does provide important information for establishing performance limits.

Second, linear monochromatic WEC models are based on steady state operation at each frequency considered in the analysis. As such, the power consumed to transition the inerter and PTO systems between operating frequencies to enable the power capture upper bound conditions across the frequency spectrum cannot be accounted for in the presented model. To account for these physical phenomena, a non-linear time domain model must be utilized, yielding a trade-off between model fidelity and the associated computational resources.

In this sense, the output from the power capture upper bound in Eq. (24), and the associated generic design guidance in Eq. (35), presented in this work, serves SRPA WEC developers to make early design decisions founded on physics rather than heuristics. These early optimally performing conceptual designs then behave as an input to more complex non-linear time domain models, where the design may be further refined at the expense of added computational resources.

6.2. *Null power capture via geometry control*

In Section 4.1, we proved Eq. (21) represents the spar impedance for a null power capture. We now explore this further to comprehend the associated dynamics using the *canonical form*. We substitute Eq. (21) into Eq. (9) to yield $\widehat{F}_{PTO_{Clamp}}(Z_{eq2_{min}}) = 0$, and then substitute this result into Eq. (2) to yield $\hat{u}_{r_{opt}}(\widehat{F}_{PTO_{Clamp}} = 0) = 0$. We conclude that the null power capture is the result of the float and spar moving together at the same relative amplitude and phase. This result is fascinating, as it does not require clamping nor disengaging the PTO between the float and spar, but rather continuously enforcing the *master-slave relationship*, while adjusting the spar impedance to eliminate any relative motion with the float. This outcome proves that *geometry control* can render the *WEC canonical form* transparent to the incoming wave. Such a circumstance may be desirable in storm conditions. We acknowledge that attaining this null power capture condition requires a means to adjust the spar resistance to $R_{eq2_{min}}$ for which the *Derived SRPA WEC Architecture* does not support. However, similar to our analysis in Section 6.1, there may exist an analogous insensitivity to $R_{eq2_{min}}$ in our operating excitation frequency range of choice, thus allowing for a null power capture through only achieving $X_{eq2_{min}}$ via adjustments in X_{FS1}.

6.3. *A Generalized method for identifying and optimizing technology innovations*

In Section 4.2, we derived the optimal force source impedance ($X_{FS1_{opt}}$) to enact optimal *geometry control*, but explicitly stated that Eq. (29) represents a performance constraint for technology design. The generic nature of this method allows designers to consider alternative *configurations* capable of achieving the same performance with various levels of design complexity. For example, instead of utilizing a parallel combination of a semi-active *inerter* and constant spring, a WEC designer could substitute both of these components with a single WaveSpring™ device [36] provided Eq. (29) is satisfied. Thus, the application of generic force sources within the mechanical circuit framework can assist designers with identifying alternative feasible technologies early in the design process through employing a functional analysis.

The method proposed in this work can also be used to optimize existing WEC architectures proposed in literature. For example, the frequency domain representation of Gradowski et al.'s [37] Hydrodynamic Negative Spring SRPA architecture can be depicted as a mechanical circuit, Thévenin's theorem may be applied to determine the *canonical form*, optimal amplitude PTO force control can be enforced through the master-slave relationship, and the geometric parameter (α) can be optimized directly without the use of a parametric analysis as presented in their work.

7. Conclusions

WEC designs are currently in the pre-commercial stage, and Weber has provided an important metric (TPL) for supporting good design decisions throughout the development process, founded on technology performance. We assert that establishing both the power capture upper bound, and the conditions for approaching the limit for each WEC *architecture*, will support the prediction of strong TPL performers early in the design process. Critical to establishing the power capture limit is enforcing the *master-slave relationship* between the PTO force control and the *geometry control* parameters regardless of the WEC topological complexity, and the mechanical circuit framework inherently provides such capability.

In this work, we successfully applied these techniques and principles to a *Derived SRPA WEC Architecture* with a tunable spar impedance via *Inertial Modulation*, and mathematically showed the maximum power this SRPA *architecture* could capture is equivalent to two single body heaving point absorbers each operating under independent complex conjugate control. In addition, we derived the optimal spar impedance required for implementing optimal geometry control and established how this optimal condition infers design guidance. We followed by comparing our numerical performance results with data from experimental trials, revealing a performance gap attributed to the added design complexity in enabling simultaneous optimal geometry and complex conjugate PTO force control in our the *Derived SRPA WEC Configuration*. Finally, we introduced *inerter* technology into the wave energy community, and demonstrated how the design guidance gained in deriving the optimal spar impedance steered us to select a parallel coupling of a semi-active *inerter* and constant spring between the spar and reaction mass. With the *inertance* adjustments based on this design guidance, we verified within the confines of linear theory that the power capture upper bound is achievable thus closing the performance gap.

Having established the feasibility of the *Derived SRPA WEC Configuration* at the conceptual stage of development, our future goal is to build a time-domain model to solicit further design guidance for operating in polychromatic wave regimes. Finally, we plan to build a scaled prototype incorporating a semi-active inerter device and perform experimental tests in a wave tank in both monochromatic and polychromatic wave regimes. The experimental data will serve to validate both the frequency and time-domain models.

We contend that this work will serve the wave energy community to identify WEC *architectures* with strong TPL early in the development cycle and, thus, unify efforts to mature designs with strong power capture potential. Furthermore, for narrow-banded power producing WECs (e.g. point absorbers), *inerter* technology presents a strong potential to enlarge their operating band through implementing optimal *geometry control*.

Acknowledgments

We would like to acknowledge the support of the Natural Sciences and Engineering Research Council of Canada (NSERC) in funding this research.

Appendix A. Original SRPA WEC Configuration

The motivation of Appendix A is to describe the physical design parameters associated with the Original SRPA WEC Configuration used in the numerical analysis of Section 5. We highlight key dimensions in Fig. 12. An overview of the model parameters are found in Table 3. Detailed frequency response plots of the linear hydrodynamic coefficients can be found in Beatty et al. [38].

References

[1] Falnes J. A review of wave-energy extraction. Mar Struct 2007;20:185–201. http://dx.doi.org/10.1016/j.marstruc.2007.09.001.
[2] Appendini CM, Urbano-Latorre CP, Figueroa B, Dagua-Paz CJ, Torres-Freyermuth A, Salles P. Wave energy potential assessment in the Caribbean Low Level Jet using wave hindcast information. Appl Energy 2015;137:375–84. http://dx.doi.org/10.1016/j.apenergy.2014.10.038.
[3] Morim J, Cartwright N, Etemad-Shahidi A, Strauss D, Hemer M. Wave energy resource assessment along the Southeast coast of Australia on the basis of a 31-year hindcast. Appl Energy 2016;184:276–97. http://dx.doi.org/10.1016/j.apenergy.2016.09.064.
[4] Atan R, Goggins J, Nash S. A detailed assessment of the wave energy resource at the atlantic marine energy test site. Energies 2016;9:967. http://dx.doi.org/10.3390/en9110967.
[5] Pinson P, Reikard G, Bidlot J-R. Probabilistic forecasting of the wave energy flux. Appl Energy 2012;93:364–70. http://dx.doi.org/10.1016/j.apenergy.2011.12.040.
[6] Robertson BRD, Hiles CE, Buckham BJ. Characterizing the near shore wave energy resource on the west coast of Vancouver Island, Canada. Renew Energy 2014;71:665–78. http://dx.doi.org/10.1016/j.renene.2014.06.006.
[7] Babarit A. A database of capture width ratio of wave energy converters. Renew Energy 2015;80:610–28. http://dx.doi.org/10.1016/j.renene.2015.02.049.
[8] Falcão AF de O. Wave energy utilization: a review of the technologies. Renew Sustain Energy Rev 2010;14:899–918. http://dx.doi.org/10.1016/j.rser.2009.11.003.
[9] Astariz S, Iglesias G. The economics of wave energy: a review. Renew Sustain Energy Rev 2015;45:397–408. http://dx.doi.org/10.1016/j.rser.2015.01.061.
[10] Bubbar K, Buckham B, Wild P. A method for comparing wave energy converter conceptual designs based on potential power capture. Renew Energy (n.d.). http://doi.org/10.1016/j.renene.2017.09.005.
[11] Weber J. WEC Technology Readiness and Performance Matrix–finding the best research technology development trajectory. In: Int. Conf. Ocean Energy; 2012.
[12] Weber J, Costello R, Ringwood J. WEC technology performance levels (TPLs)-metric for successful development of economic WEC technology. In: Proc. EWTEC 2013; 2013.
[13] Babarit A. Ocean wave energy conversion: resource, technologies and performance. Elsevier; 2017.
[14] Falnes J. Ocean waves and oscillating systems: linear interactions including wave-energy extraction. Cambridge; New York: Cambridge University Press; 2002.
[15] Falnes J. Wave-energy conversion through relative motion between two single-mode oscillating bodies. J Offshore Mech Arct Eng 1999;121:32–8. http://dx.doi.org/10.1115/1.2829552.
[16] Price AAE, Dent CJ, Wallace AR. On the capture width of wave energy converters. Appl Ocean Res 2009;31:251–9. http://dx.doi.org/10.1016/j.apor.2010.04.001.
[17] Harris CM, Crede CE, Trent HM. Shock and vibration handbook, vol. I, 1st ed.; 1962. http://adsabs.harvard.edu/abs/1962PhT....15i..65H [accessed December 23, 2015].
[18] Nebel P. Maximizing the efficiency of wave-energy plant using complex-conjugate control. Proc Inst Mech Eng Part J Syst Control Eng 1992;206:225–36.
[19] Hals J, Falnes J, Moan T. A comparison of selected strategies for adaptive control of wave energy converters. J Offshore Mech Arct Eng 2011;133:031101.
[20] Budal K, Falnes J. A resonant point absorber of ocean-wave power. Nature 1975;256:478–9.
[21] French MJ. A generalized view of resonant energy transfer. J Mech Eng Sci 1979;21:299–300.
[22] Guenther DA, Jones D, Brown DG. An investigative study of a wave-energy device. Energy 1979;4:299–306. http://dx.doi.org/10.1016/0360-5442(79)90129-4.
[23] Wright A, Beattie WC, Thompson A, Mavrakos SA, Lemonis G, Nielsen K, et al. Performance considerations in a power take-off unit based on a non-linear load. In: Proc 5th Eur. Wave Energy Conf. Cork; 2003.
[24] Ringwood JV, Bacelli G, Fusco F. Energy-maximizing control of wave-energy converters: the development of control system technology to optimize their operation. IEEE Control Syst 2014;34:30–55. http://dx.doi.org/10.1109/MCS.2014.2333253.
[25] Garcia-Rosa PB, Bacelli G, Ringwood JV. Control-informed geometric optimization of wave energy converters: the impact of device motion and force constraints. Energies 2015;8:13672–87. http://dx.doi.org/10.3390/en81212386.
[26] Korde UA. On providing a reaction for efficient wave energy absorption by floating devices. Appl Ocean Res 1999;21:235–48.
[27] Korde UA. On controlled oscillating bodies with submerged reaction mass. In: OMAE 2003-37012, Cancun, Mexico; 2003. p. 405–11. http://doi.org/10.1115/OMAE2003-37012.
[28] Korde UA. Systems of reactively loaded coupled oscillating bodies in wave energy conversion. Appl Ocean Res 2003;25:79–91. http://dx.doi.org/10.1016/S0141-1187(03)00044-0.
[29] French MJ, Bracewell R. Heaving point absorbers reacting against an internal mass. In: Evans DDV, de Falcão PAFO, editors. Hydrodyn. Ocean Wave-Energy Util., Springer Berlin Heidelberg; 1986. p. 247–55. http://doi.org/10.1007/978-3-642-82666-5_21.
[30] Diamond CA, Judge CQ, Orazov B, Savaş Ö. O.M. O'Reilly, Mass-modulation schemes for a class of wave energy converters: experiments, models, and efficacy. Ocean Eng 2015;104:452–68. http://dx.doi.org/10.1016/j.oceaneng.2015.05.018.
[31] Tom NM, Lawson MJ, Yu YH, Wright AD. Development of a nearshore oscillating surge wave energy converter with variable geometry. Part A Renew Energy 2016;96:410–24. http://dx.doi.org/10.1016/j.renene.2016.04.016.
[32] Kurniawan A, Moan T. Characteristics of a pitching wave absorber with rotatable flap. Energy Proc 2012;20:134–47.
[33] Victor L, Troch P, Kofoed JP. On the effects of geometry control on the performance of overtopping wave energy converters. Energies 2011;4:1574–600. http://dx.doi.org/10.3390/en4101574.
[34] Liu C. A tunable resonant oscillating water column wave energy converter. Ocean Eng 2016;116:82–9. http://dx.doi.org/10.1016/j.oceaneng.2016.02.004.
[35] Dick W. Wave energy converter, US7909536 B2; 2011. http://www.google.com/patents/US7909536.
[36] Todalshaug JH, Ásgeirsson GS, Hjálmarsson E, Maillet J, Möller P, Pires P, et al. Tank testing of an inherently phase-controlled wave energy converter. Int J Mar Energy 2016;15:68–84. http://dx.doi.org/10.1016/j.ijome.2016.04.007.
[37] Gradowski M, Alves M, Gomes RP, Henriques JC. Integration of a hydrodynamic negative spring concept into the OWC Spar Buoy, Cork, Ireland; 2017.
[38] Beatty SJ, Hall M, Buckham BJ, Wild P, Bocking B. Experimental and numerical comparisons of self-reacting point absorber wave energy converters in regular waves. Ocean Eng 2015;104:370–86.
[39] Beatty S. Analysis and development of a three body heaving wave energy converter. University of Victoria; 2009.
[40] Falnes J. Radiation impedance matrix and optimum power absorption for interacting oscillators in surface waves. Appl Ocean Res 1980;2:75–80. http://dx.doi.org/10.1016/0141-1187(80)90032-2.
[41] Kirchhoff G. Ueber die Auflösung der Gleichungen, auf welche man bei der Untersuchung der linearen Vertheilung galvanischer Ströme geführt wird. Ann Phys 1847;148:497–508. http://dx.doi.org/10.1002/andp.18471481202.
[42] Thévenin L. Sur un nouveau théoreme d'électricité dynamique [On a new theorem of dynamic electricity]. CR Séances L'Académie Sci 1883;97:159–61.
[43] Hals J. Modelling and phase control of wave-energy converters. Norwegian University of Science and Technology; 2010.
[44] Hai L, Svensson O, Isberg J, Leijon M. Modelling a point absorbing wave energy converter by the equivalent electric circuit theory: a feasibility study. J Appl Phys 2015;117:164901. http://dx.doi.org/10.1063/1.4918903.
[45] Kurniawan A, Pedersen E, Moan T. Bond graph modelling of a wave energy conversion system with hydraulic power take-off. Renew Energy 2012;38:234–44. http://dx.doi.org/10.1016/j.renene.2011.07.027.
[46] Bacelli G, Gilloteaux J-C, Ringwood JV. State space model of a hydraulic power take off unit for wave energy conversion employing bondgraphs. WREC; 2008. http://eprints.maynoothuniversity.ie/4419/ [accessed December 23, 2015].
[47] Bott R, Duffin RJ. Impedance synthesis without use of transformers. J Appl Phys 1949;20:816. http://dx.doi.org/10.1063/1.1698532.
[48] Smith MC. Synthesis of mechanical networks: the inerter. IEEE Trans Autom Control 2002;47:1648–62. http://dx.doi.org/10.1109/TAC.2002.803532.
[49] Chen MZQ, Papageorgiou C, Scheibe F, Wang F, Smith MC. The missing mechanical circuit element. IEEE Circuits Syst Mag 2009;9:10–26. http://dx.doi.org/10.1109/MCAS.2008.931738.
[50] Hu Y, Chen MZQ, Xu S, Liu Y. Semiactive inerter and its application in adaptive tuned vibration absorbers. IEEE Trans Control Syst Technol 2017;25:294–300. http://dx.doi.org/10.1109/TCST.2016.2552460.
[51] Chen MZQ, Hu Y, Li C, Chen G. Semi-active suspension with semi-active inerter and semi-active damper. IFAC Proc 2014;47:11225–30. http://dx.doi.org/10.3182/20140824-6-ZA-1003.00138.
[52] Wang F-C, Hong M-F, Lin T-C. Designing and testing a hydraulic inerter. Proc Inst Mech Eng Part C J Mech Eng Sci 2011;225:66–72. http://dx.doi.org/10.1243/09544062JMES2199.
[53] Beatty S. Self-reacting point absorber wave energy convertors. University of Victoria; 2015.
[54] Evans DV. Maximum wave-power absorption under motion constraints. Appl Ocean

Applied Energy 228 (2018) 324–338

Res 1981;3:200–3. http://dx.doi.org/10.1016/0141-1187(81)90063-8.

[55] Newman JN. The interaction of stationary vessels with regular waves. In: Proc. 11th Symp. Nav. Hydrodyn. Lond.; 1976. p. 491–501.

[56] Evans DV. A theory for wave-power absorption by oscillating bodies. J Fluid Mech 1976;77:1–25. http://dx.doi.org/10.1017/S0022112076001109.

[57] Beatty S, Ferri F, Bocking B, Kofoed JP, Buckham B. Power take-off simulation for scale model testing of wave energy converters. Energies 2017;10:973. http://dx.doi.org/10.3390/en10070973.

[58] Liang C, Ai J, Zuo L. A self-reacting point absorber with a novel mechanical motion rectifier as power takeoff system; 2014. p. V002T32A004. http://doi.org/10.1115/DSCC2014-6292.

[59] Falcão AF de O. Phase control through load control of oscillating-body wave energy converters with hydraulic PTO system. Ocean Eng 2008;35:358–66. http://dx.doi.org/10.1016/j.oceaneng.2007.10.005.

[60] Korde UA. Phase control of floating bodies from an on-board reference. Appl Ocean Res 2001;23:251–62.

8 Appendix C: On establishing generalized analytical phase control conditions in self-reacting point absorber wave energy converters

K. Bubbar, B. Buckham, On establishing generalized analytical phase control conditions in self-reacting point absorber wave energy converters, Renewable Energy. (2018); Submitted.

On Establishing Generalized Analytical Phase Control Conditions in Self-Reacting Point Absorber Wave Energy Converters

K. Bubbar*, and B. Buckham

Department of Mechanical Engineering
West Coast Wave Initiative
Institute for Integrated Energy Systems
University of Victoria
3800 Finnerty Rd, Victoria, B.C.
V8W 3P6, CANADA

Abstract

It is widely suggested that step gains in wave energy converter power capture performance must be realized to achieve economic viability. One method of fulfilling such power capture gains is to invoke resonant conditions between the device and the incoming ocean wave. However, a general method that can establish the prerequisites for achieving resonant conditions in an arbitrarily complex wave energy converter architecture is nonexistent.

In this work, we present an analytical procedure, built on the mechanical circuit framework, for identifying the resonant conditions of an arbitrarily complex wave energy converter architecture. To demonstrate the procedure, we select three complex self-reacting point absorber devices as a case study, each with a geometry controllable feature set. Applying these constraints to each architecture, we illustrate how the frequency response of the power production varies across these architectures. Selecting the highest performing architecture, we then reveal how the analytical constraint can be applied as a generic design criterion in the design of an inerter device that provides optimal geometry control. Finally, we apply the analytics within a numerical case study of a previously published wave energy converter configuration and present a hierarchy, which describes the incremental performance improvements that can be realized through implementing steps in control complexity for this device.

Keywords: wave energy conversion; phase control; geometry control; mechanical circuits; WEC canonical form; inerter technology;

56 Nomenclature

Acronyms:

PTO	Power Take-Off
SBPA	Single Body Point Absorber
SRPA	Self-Reacting Point Absorber
WEC	Wave Energy Converter

Parameters:

β	Transmission ratio
γ	Relative phase angle between $\hat{F}_{PTO_{Clamp}}$ and $\hat{u}_r$ (deg)
ω	Excitation angular frequency of the incoming wave elevation time series (rad/s)
$\hat{F}_{ex1}, \hat{F}_{ex2}$	Complex amplitude of the hydrodynamic excitation force on float, spar (N)
$\hat{F}_{FSn}$	Complex force amplitude exerted by the nth Force Source (N)
$\hat{F}_{FSn_{free}}$	Complex force amplitude exerted by the nth Force Source when the PTO impedance is zero (N)
$\hat{F}_i$	Complex force amplitude exerted on the intrinsic mechanical impedance of the WEC (N)
$\hat{F}_{meff}$	Complex reaction force amplitude exerted by the inerter (N)
$\hat{F}_{PTO}$	Complex force amplitude exerted on the PTO (N)
$\hat{F}_{PTO_{Clamp}}$	Complex force amplitude exerted on the PTO when the magnitude of the PTO impedance is infinite (N)
$\hat{F}_{Zeq1}, \hat{F}_{Zeq2}$	Complex force amplitude exerted on the equivalent float, spar impedance (N)
$\hat{F}_{Zeq1_{Clamp}}, \hat{F}_{Zeq2_{Clamp}}$	Complex force amplitude exerted on the equivalent float, spar impedance when the magnitude of the PTO impedance is infinite (N)
$\hat{F}_{Zeq1_{free}}, \hat{F}_{Zeq2_{free}}$	Complex force amplitude exerted on the equivalent float, spar impedance when the PTO impedance is zero (N)
J	Moment of inertia of the flywheel $(kg \cdot m^2)$
k_3	Linear spring stiffness coefficient (N/m)
m_1, m_2, m_3	Mass of the float, spar, reaction mass (kg)
m_{eff}	Inertance (kg)
$m_{eff_{min}}, m_{eff_{max}}$	Minimum and maximum feasible inertance settings (kg)
$m_{eff_{opt}}$	Optimal inertance to maximize power capture (kg)
P_{Exp}	Average useful power capture per excitation angular frequency as measured in experimental trials (W)

P_U	Average useful power capture per excitation angular frequency (W)
$P_{U_{Max(AC)}}$	Average useful power capture per excitation angular frequency with the PTO operating under amplitude control (W)
$P_{U_{Max}}\|_{opt}$	Average useful power capture per excitation angular frequency under complex conjugate PTO force control and optimal geometry control (W)
R_{eqn}, X_{eqn}	Equivalent resistance and reactance of the float $(n=1)$ and spar $(n=2)$
R_{PTO}, X_{PTO}	Resistance and reactance of the PTO (Ns/m)
$R_{PTO_{opt}}, X_{PTO_{opt}}$	Optimal resistance and reactance of the PTO to maximize power capture (Ns/m)
$\hat{u}_1, \hat{u}_2, \hat{u}_3$	Complex velocity amplitude of float, spar, reaction mass (m/s)
$\hat{u}_{1_{free}}, \hat{u}_{2_{free}}$	Complex velocity amplitude of float, spar, when the PTO impedance is zero (m/s)
$\hat{u}_{Clamp}$	Complex velocity amplitude of float, spar, when the magnitude of the PTO impedance is infinite (m/s)
$\hat{u}_r$	Complex relative velocity amplitude measured between the float and spar (m/s)
$\hat{u}_{r_{Free}}$	Complex relative velocity amplitude measured across the PTO when the PTO impedance is set to zero (m/s)
$X_{eq1_{opt}}$	Optimal equivalent reactance of the float to maximize power capture (Ns/m)
$X_{eq2_{opt}}$	Optimal equivalent reactance of the spar to maximize power capture (Ns/m)
X_{FSn}	Reactance of the n^{the} Force Source (Ns/m)
$X_{FSn_{opt}}$	Optimal reactance of the n^{the} Force Source to maximize power capture (Ns/m)
Z, R, X	Generic mechanical impedance, resistance, reactance (Ns/m)
Z_{A11}, Z_{A22}	Hydrodynamic added mass impedance of float, spar (Ns/m)
Z_{B11}, Z_{B22}	Hydrodynamic radiation damping impedance of float, spar (Ns/m)
Z_{eq1}, Z_{eq2}	Equivalent impedance of the float, spar (Ns/m)
Z_{FSn}	Impedance of the nth Force Source (Ns/m)
Z_i	Intrinsic mechanical impedance of the WEC (Ns/m)
Z_{K1}, Z_{K2}	Hydrostatic buoyancy stiffness impedance of float, spar (Ns/m)
Z_{m1}, Z_{m2}	Mass impedance of float, spar (Ns/m)
Z_{meff}	Inerter mechanical impedance (Ns/m)
Z_{mH2}	Impedance of combined spar mass and hydrodynamics (Ns/m)
Z_{PTO}	PTO mechanical impedance (Ns/m)

1 Introduction

Being collocated with large coastal populations, ocean wave energy presents a compelling case as a potential renewable energy resource. However, wave energy converter (WEC) devices have yet to display commercial viability as compared to alternative renewable energy sources [1]. At present, WEC devices do not capture sufficient power from the wave resource to offset the costs of operating offshore, and thus are not economically viable [2]. As expressed by Weber, the power capture capacity of a WEC device is influenced by choices largely made early in the conceptual design stage of a development program [3]. The traditional conceptual development process involves: 1) choosing a device class based on operating principle [4,5], 2) defining the geometry and inertial characteristics of the floating body based on heuristics and logistical constraints, and 3) coupling this body to a Power Take-Off (PTO) unit used to convert the kinetic energy of the wave induced body into a useful form. In this process, the hydrodynamics and inertial properties of the body are adopted as constraints, whereas the Power Take-Off (PTO) is considered a configurable unit. In this traditional view, power capture maximization by the PTO, requires implementing the *complex-conjugate* [6] PTO force control conditions based on a set mechanical impedance of the WEC. Implementation of complex-conjugate control requires a multi-functional resistive/reactive PTO capable of optimally setting the: 1) PTO reactance, X_{FS1} in Figure 1a, to inject reactive power back into the body altering its relative phase with respect to the incoming wave excitation force, to achieve optimal phase control, and 2) PTO resistance, R_{PTO}, to achieve optimal amplitude control and maximize power capture through modulating the body motion [7]. For the specific case of a Single Body Point Absorber (SBPA) WEC architecture, the optimal settings for these sub functions to maximize power capture are well understood [7].

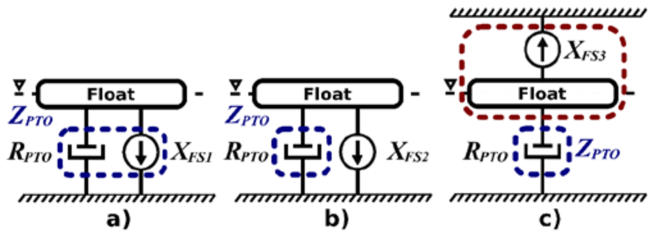

Figure 1: Mechanical schematic for SBPA WEC Architectures:
a) Resistive/Reactive PTO; b) Resistive PTO with Parallel Reactive Control;
c) Resistive PTO with Reactively Controlled Float

However, an SBPA with a resistive/reactive PTO, represented by Figure 1a, is only one possible SBPA architecture for realizing maximum power. For example, consider the mechanical schematics in Figure 1b and Figure 1c for which the PTO is represented as a solely resistive mechanical damper element. Clearly, neither PTO contains a reactive element in these architectures and thus cannot implement complex-conjugate PTO force control. However, both WEC architectures contain feature sets external to the PTO, represented as reactive force sources, which can inject the necessary reactive power to enable optimal phase control and hence achieve the same power capture performance. This distinction between the point absorber architectures in Figure 1 may appear as mere *semantics* in the SBPA as the differences originate from the choice to separate the reactive element from the PTO, while all three architectures remain topologically equivalent. With more complex WEC architectures, such as the Self-Reacting Point Absorber (SRPA), there are a variety of locations where the reactive element may be placed, leading to significant topological differences between architectures. Figure 2 pictorially represents three different SRPA architectures: 1) Figure 2a, labelled *Arch1*, is the conventional SRPA containing a traditional resistive/reactive PTO, 2) Figure 2b, labelled *Arch2*, contains a resistive PTO with an independent but parallel reactive force source, and 3) Figure 2c, labelled *Arch3*, contains a resistive PTO with a reactively controlled spar. There is a strong motivation to determine the optimal power capture performance of complex WEC architectures such as *Arch2* and *Arch3*, and to define the optimal conditions on the force sources $(X_{FS2_{opt}}, X_{FS3_{opt}})$ leading to optimal performance, with the emergence of new technologies based on these architectures. For example, SRPAs interfaced with: 1) Liang's [8] MMR technology, and 2) Gradowski's [9] Hydrodynamic Negative Spring are generically represented by *Arch2* and *Arch3* respectively. We believe that such contemporary WEC devices are only the *tip of the iceberg* as the WEC design space evolves to consider greater topological complexity in pursuit of step increases in power capture capacity.

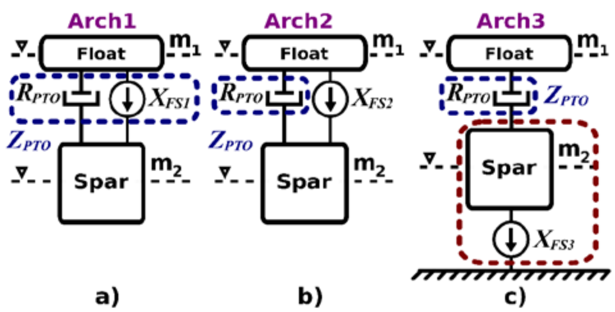

Figure 2: Mechanical Schematic for the three Resonantly Controlled SRPA WEC Architectures with:
a) *Arch1*—Resistive / Reactive PTO;
b) *Arch2*—Resistive PTO with a Reactive Force Source between the Floating Bodies;
c) *Arch3*—Resistive PTO with a Reactive Force Source between the Spar and Ground

To determine the performance merits of these complex alternative WEC architectures at the conceptual stage of development, we need a means to establish equations outlining both the conditions on the reactive force source required to implement optimal phase control and the subsequent power capture potential. The traditional view of a PTO with a reactive feature emerged as the result of the perception that a WEC device possessed unchangeable hydrodynamic and inertial parameters (i.e. no geometry control feature implemented within the

WEC). This view promoted the proposition of implementing the optimal phase control function as an internal feature of the PTO allowing for the determination of the optimal force source reactance $(X_{FS1_{opt}})$ in *Arch1*. To determine the optimal force source reactance $(X_{FS3_{opt}})$ in more complex WEC architectures such as *Arch3*, we must move beyond this traditional resistive/reactive PTO paradigm. To accomplish this, a more generalized view of phase control is required, for which we choose to revert to the original works of Mei [10], Evans [11], and Falnes [7]. In their works, the phase control condition was originally identified as simply the state of achieving system resonance. With this generalized interpretation of phase control, the equations sought above can be determined analytically if the complex WEC architectures are first transformed into the *WEC canonical form* [12]. Once in canonical form, constraints enforcing system resonance are imposed on the canonical form leading to the optimal force source reactance. Once the device is in resonance, one can apply optimal PTO damping and thus determine maximum power capture. Although the importance of enforcing resonant conditions with the incoming waves is clear, analytical expressions guiding WEC developers in their technology development processes do not exist except for very simple WEC architectures (e.g. SBPAs). In this work, we demonstrate through a case study the transformation of the three SRPA architectures in Figure 2, *Arch1*, *Arch2,* and *Arch3*, into the canonical form and then apply analytical constraints to invoke system resonance. In doing so, we will show that the choice of injecting reactance into *Arch3* delivers superior performance, both in terms of level of power capture and in the minimization of the relative travel between the float and spar.

The structure of this paper is as follows. In Section 2, we briefly review how a complex WEC architecture is transformed into canonical form through applying the process outlined by Bubbar et al. [12], followed by examining the definition of WEC resonance in this context. In

Section 3, we transform *Arch1*, *Arch2* and *Arch3* into the canonical form, enforce the resonant condition and extract the optimal force source reactances, $X_{FS1_{opt}}$, $X_{FS2_{opt}}$ and $X_{FS3_{opt}}$. In doing so, we generate analytical constraints used to guide technology design that apply across all configurations in the architectures considered. In Section 4, we perform a numerical analysis to compare the power capture performance and system dynamic responses of five specific configurations (*Config1-5*) generated based on *Arch1*, *Arch2*, and *Arch3* using experimentally validated device parameters from a 1/25th scale model published by Beatty et al. [13]. Finally, in Section 5, having selected a single configuration for further analysis, we demonstrate how the development process introduced in this work, enables technology innovation by substituting the reactive force source with a sub circuit of mechanical machinery components incorporating a unique technology, the inerter, encased within the confines of the spar. We explore the potential of inerter technology for enabling resonant control of our configuration, under realistic physical design constraints. We conclude by illustrating a hierarchy within our case study describing how incremental levels of WEC control complexity relate to improving the resulting power capture performance. Our motivation is to present WEC developers with choices and the associated trade-offs to consider during the conceptual design phase of an SRPA project leading to improved power capture potential.

2 Theory

2.1 Frequency Domain Modelling of WECs Using Mechanical Circuits

Restricting oneself to a linear hydrodynamics regime, WEC devices are initially considered as linear underdamped mechanical vibration systems comprised of masses, springs, and dampers [7]. Specific arrangements of these mechanical elements define a WEC architecture [12]. As described by Bubbar et al. [12], all WEC architectures may be represented in topological form as a mechanical circuit with mechanical impedance elements interfaced at common nodes [14]. These linear vibration systems are energized via a periodic sinusoidal external wave excitation force, represented as a force source, resulting in body motion. The PTO, represented as a configurable impedance block, captures energy when the wave-induced bodies do work against a reaction force within that block — characterized as a resistive element. Once a WEC architecture is represented as a mechanical circuit, the system topology may be simplified by substituting the mechanical impedance constitutive equations for each mechanical element and applying network synthesis methods [14] to determine the canonical form [12]. The canonical form is an equivalent mechanical circuit representing the simplest WEC architecture — the SBPA. Once in canonical form, system kinematic and dynamic variables, such as eq.(3)-eq.(5), can be calculated for any given monochromatic incident wave. We note any single mechanical impedance block is a complex quantity generically represented as the sum of resistive (R) and reactive (X) parameters as in eq.(1).

$$Z = R + iX \qquad \text{eq.(1)}$$

2.2 Resonance of the SBPA Architecture

For a heaving SBPA architecture, the power capture is maximized when both system resonance is achieved and the PTO resistance is optimally set. To enforce system resonance through an analytical means, a mathematical definition of the resonant condition consistent with the mechanical impedance formulation must be determined. Falnes [7] proposed an equation inspired from electronic circuit theory. In his proposition, a functional boundary was defined to separate the PTO impedance (Z_{PTO}), from the remaining lumped SBPA impedance or intrinsic impedance (Z_i), illustrated by the mechanical circuit in Figure 3b.

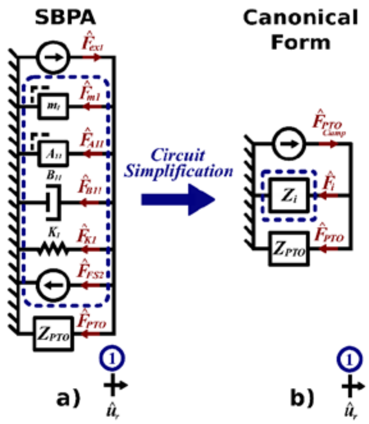

Figure 3: SBPA as the Canonical Form

From this functional separation, Falnes proposed that the natural frequency of the remaining SBPA WEC architecture is determined by evaluating eq.(2) (cf. 5.324 [7]).

$$\Im m\{Z_i\} = 0 \qquad \text{eq.(2)}$$

For a heaving SBPA with constant geometry and inertia, and with an amplitude controlled PTO, resonance only occurs when the incoming wave excitation frequency is equal to the natural frequency of the floating body. For all other wave excitation frequencies, resonance is not achieved without intervention. Clearly, invoking resonance across a bandwidth of operating frequencies is desired to maximize power capture. Thus a feature set independent from the PTO (i.e. within the definition of Z_i) capable of injecting the appropriate reactance into the remaining system to satisfy eq.(2) would achieve the desired result. In choosing to represent the SBPA architecture using a resistive PTO and a reactive force source external to the PTO, the resonance control problem may be classified as a subset of geometry control first introduced by Price [15]. In Figure 3a, we observe a mechanical circuit of the SBPA architecture schematically represented in Figure 1b, with a reactive force source, $\hat{F}_{FS2}$, external to the PTO.

Once system resonance is invoked, maximizing the power captured by the resistive PTO requires applying the impedance matching criteria [7] to set R_{PTO} according to eq.(3). When $R_{PTO} = R_{PTO_{opt}}$, amplitude control is invoked by the PTO and the power captured is defined by eq.(4), with the complex amplitude of the body velocity defined by eq.(5) [7].

$$R_{PTO_{opt}} = |Z_i| \qquad \text{eq.(3)}$$

$$P_{U_{Max(AC)}} = \frac{|\hat{F}_{PTO_{Clamp}}|^2}{4[\Re e\{Z_i\} + |Z_i|]} \qquad \text{eq.(4)}$$

$$\hat{u}_r = \frac{\hat{F}_{PTO_{Clamp}}}{Z_i + |Z_i|} \qquad \text{eq.(5)}$$

In SBPAs, resonance is the condition in which the wave excitation force is in phase with the float velocity. This description is visually intuitive and, thus, analytical design guidance is relatively straightforward to implement in linear monochromatic WEC models. As WEC architecture complexity increases and more bodies and components are considered in a conceptual design, (e.g. SRPAs), this visual intuition becomes clouded. As a multi-body system, the motion of the complex WEC architecture is described in terms of its natural modes of vibration. It is unclear how the shape of each vibration mode influences power capture. As such, WEC developers resort to specifying design parameters early in the design process. This locks focus onto a specific WEC configuration [12], but allows for implementation of numerical optimization routines to search for the resonant conditions. Unfortunately, the insights obtained from these numerical optimizations cannot be generalized across configurations, and WEC developers are left resorting to a trial and error process as configurations evolve. There is, therefore, an acute need for extending the analytical methods for evaluating the resonant conditions available to SBPAs, to more complex WEC architectures.

2.3 SBPA as the WEC Canonical Form

The SRPA [16], with its PTO interfaced between two wave activated bodies, was a natural development on the SBPA as the two-body architecture eliminated the need for an ocean floor reference. However, this introduced a new challenge as analytical equations describing the maximum power capture conditions were unknown. Falnes provided a path forward by developing an ingenious analytical interpretation of the impedance matching problem. Falnes applied a mechanical Thévenin [17,18] equivalency transformation and represented the SRPA WEC architecture as a phenomenological equivalent SBPA — the canonical form in Figure 1b with an equivalent single body intrinsic impedance, wave excitation force, and single body velocity [18]. In this formulation, the equivalent wave excitation force, $\hat{F}_{PTO_{Clamp}}$, is the force experienced across the PTO of the SRPA when the PTO rigidly secures the float to the spar, whereas the equivalent single body velocity $(\hat{u}_r)$ is the relative velocity measured across the PTO.

With this formulation Falnes exposed an important insight— resonant conditions are invoked in the SRPA architecture when $\hat{F}_{PTO_{Clamp}}$ is in phase with $\hat{u}_r$, which does not necessarily coincide with the resonant conditions of either of the individual bodies [18]. Since Thévenin's theorem is invariant to topological complexity, Falnes' impedance matching strategy in the

SRPA architecture has been generalized by Bubbar et al. [12] for WEC architectures of arbitrary complexity through the use of the mechanical circuit framework [14]. As the *canonical form* is simply the representation of a complex WEC architecture as an equivalent SBPA architecture, the resonant condition(s) for the complex WEC architecture may be determined through substituting Z_i, isolated from the canonical form, into Falnes' well-established analytical condition, eq.(2), for resonance in SBPAs. In this formulation, both $\hat{F}_{PTO_{Clamp}}$ and Z_i, isolated from the canonical form, are now functions of the physical parameters of the complex WEC architecture. In addition, the power capture, subject to optimal PTO damping, is determined by eq.(4), and the relative complex velocity amplitude between the float and spar, as measured across the PTO, is determined by eq.(5).

In this work, we will demonstrate the derivation of Z_i and $\hat{F}_{PTO_{Clamp}}$, for *Arch1*, *Arch2* and *Arch3*, enforce both the optimal resonant condition eq.(2), and amplitude PTO force control eq.(3) and establish conditions on the generic force sources $(X_{FS1}, X_{FS2}, X_{FS3})$ that ensure resonant control of our complex WEC architectures.

3 Establishing Resonant Conditions in SRPAs

In this section, we consider three complex SRPA WEC architectures *Arch1*, *Arch2*, and *Arch3*, illustrated in Figure 2, all capable of implementing resonant control. For simplifying the ensuing algebra, we choose an SRPA for which the coupled radiation forces are known to be negligible (cf. Appendix E [19]). Each architecture is configured with one reactive force source represented by the complex force amplitude $\hat{F}_{FSn}$, with $n=[1,2,3]$ signifying the indices for the architecture number considered. This force source generates an unbounded monochromatic force signal at the frequency of the incoming ocean wave. The force sources $\hat{F}_{FS1}$ and $\hat{F}_{FS2}$ are proportional to the relative complex velocity amplitude difference $(\hat{u}_1 - \hat{u}_2)$ between the float and spar in their respective architectures and described mathematically by eq.(6). Whereas the force source in *Arch3*, $\hat{F}_{FS3}$, is proportional to the absolute complex velocity amplitude of the spar as in eq.(7).

$$\hat{F}_{FSn} = Z_{FSn}(\hat{u}_1 - \hat{u}_2),\ n = [1,2] \qquad \text{eq.(6)}$$

$$\hat{F}_{FS3} = Z_{FS3}\hat{u}_2 \qquad \text{eq.(7)}$$

As introduced by Korde [20], we characterize the resulting force by the impedance in eq.(8), which is controlled by the force source reactance X_{FSn}.

$$Z_{FSn} = iX_{FSn},\ n = [1,2,3] \qquad \text{eq.(8)}$$

In this section we will derive $X_{FSn_{opt}}$ — the force source reactance, which results in resonant control of *Arch1*, *Arch2* and *Arch3*. To derive these equations, we must first determine analytical expressions of Z_i for *Arch1*, *Arch2* and *Arch3*.

We first explore *Arch2* and *Arch1* in Section 3.1 and Section 3.2 respectively, noting that while they are topologically equivalent, they are subtly distinct based on the definition of the PTO boundary as discussed in Section 1. For *Arch1*, with X_{FS1} defined internal to the PTO, we apply the complex-conjugate conditions verbatim, whereas for *Arch2*, with X_{FS2} defined external to the PTO, we apply the resonant control law in eq.(2). As we will demonstrate in Section 4.1, the choice of defining X_{FS1} internal to the PTO boundary, invalidates eq.(2) as a constraint equation to enforce system resonance. Although this result has little impact on determining $X_{FS1_{opt}}$, as the complex-conjugate impedance matching conditions may be applied in lieu of eq.(2) to solve for $X_{FS1_{opt}}$, the choice of defining the PTO boundary does have a significant impact on how $X_{FS3_{opt}}$ is determined in *Arch3*.

Consequently, next we explore *Arch3*, which is topologically represented by a reactive force source, X_{FS3}, interfaced between the spar and ocean floor. In *Arch3* the spar is seen as a variable reactance subsystem. In Section 3.2, we derive the optimal force source reactance, $X_{FS3_{opt}}$, for enacting resonant control of *Arch3*.

3.1 The Arch2 Canonical Form:

To determine the canonical form of *Arch2* we execute the procedure outlined by Bubbar et al. [12]. Step 1 comprises generating the mechanical circuit representing *Arch2* as in Figure 4a. Step 2 involves simplifying this mechanical circuit through the application of parallel $(\|)$ and series $(\multimap)$ circuit transformations [14] resulting in Figure 4b; for which we define two new lumped impedance terms, Z_{eq1} and Z_{eq2} in eq.(9)-eq.(10), representing the equivalent float and spar impedances respectively.

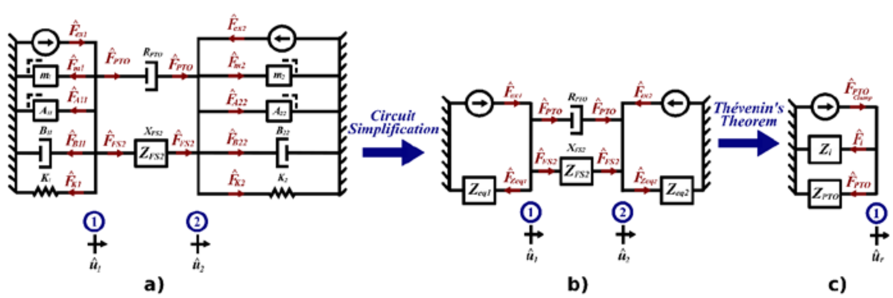

Figure 4: Mechanical Circuits for Arch2:
a) Full Circuit; b) Simplified Circuit; c) WEC Canonical Form

We explicitly note that in applying our circuit simplifications, Z_{FS2} is contained outside the definitions of either Z_{eq1} or Z_{eq2}.

$$Z_{eq1} = Z_{m1} \,||\, Z_{A11} \,||\, Z_{B11} \,||\, Z_{K1} = Z_{m1} + Z_{A11} + Z_{B11} + Z_{K1} \qquad \text{eq.(9)}$$

$$Z_{eq2} = Z_{m2} \,||\, Z_{A22} \,||\, Z_{B22} \,||\, Z_{K2} = Z_{m2} + Z_{A22} + Z_{B22} + Z_{K2} \qquad \text{eq.(10)}$$

With the simplified circuit of *Arch2* established, in Step 3 we analytically determine two parameters inherent to this architecture, $\hat{u}_{r_{Free}}$ — a case of the relative velocity between the float and spar when the PTO resistance is eliminated, and $\hat{F}_{PTO_{Clamp}}$ — a case of a PTO clamped through force developed when the PTO rigidly secures the float to the spar. To determine these parameters we represent these cases by augmenting the mechanical circuit of Figure 4b with the two new circuits in Figure 5. Upon establishing the analytical equations for $\hat{u}_{r_{Free}}$ in Section 3.1.1, and $\hat{F}_{PTO_{Clamp}}$ in Section 3.1.2, we continue with Step 4 by using these expressions to determine Z_i in Section 3.1.3. Finally, in Step 5 we substitute Z_i into eq.(2) and isolate the optimal force source impedance, $X_{FS2_{opt}}$, to enforce the system resonance condition in Section 3.1.4.

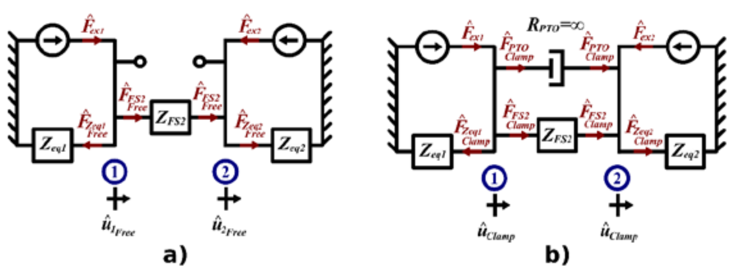

Figure 5: Solving for the Thévenin Equivalent System for Arch2
a) Free Relative Velocity; b) Clamped Through Force

3.1.1 Free Relative Velocity Difference

To determine $\hat{u}_{r_{Free}}$, we apply Kirchhoff's Node Law on each node in Figure 5a resulting in eq.(11)-eq.(12).

$$\hat{F}_{ex1} = Z_{eq1}\hat{u}_{1_{Free}} + Z_{FS2}(\hat{u}_{1_{Free}} - \hat{u}_{2_{Free}})\,|_{Node_1} \qquad \text{eq.(11)}$$

$$\hat{F}_{ex2} = Z_{eq2}\hat{u}_{2_{Free}} - Z_{FS2}(\hat{u}_{1_{Free}} - \hat{u}_{2_{Free}})\,|_{Node_2} \qquad \text{eq.(12)}$$

For which we can solve for $\hat{u}_{r_{Free}}$ as in eq.(13).

$$\hat{u}_{r_{Free}} = \hat{u}_{1_{Free}} - \hat{u}_{2_{Free}} = \frac{\hat{F}_{ex2}Z_{eq1} - \hat{F}_{ex1}Z_{eq2}}{Z_{eq1}Z_{eq2} + Z_{FS2}(Z_{eq1} + Z_{eq2})} \qquad \text{eq.(13)}$$

3.1.2 PTO Clamped Through Force:

To determine $\hat{F}_{PTO_{Clamp}}$ we analyze the circuit in Figure 5b under the knowledge that both the float and spar are constrained to move together and hence, there is no relative motion across the PTO leading to eq.(14).

$$\hat{u}_1 = \hat{u}_2 = \hat{u}_{Clamp} \qquad \text{eq.(14)}$$

We also note that all the force between nodes 1 and 2 passes through the PTO, and thus applying Kirchhoff's Node Law on each node results in eq.(15)-eq.(16).

$$\hat{F}_{ex1} = \hat{F}_{PTO_{Clamp}} + Z_{eq1}\hat{u}_{Clamp}\,|_{Node_1} \qquad \text{eq.(15)}$$

$$\hat{F}_{ex2} = -\hat{F}_{PTO_{Clamp}} + Z_{eq2}\hat{u}_{Clamp}\,|_{Node_2} \qquad \text{eq.(16)}$$

Using eq.(15) and eq.(16) to solve for $\hat{F}_{PTO_{Clamp}}$ while eliminating $\hat{u}_{Clamp}$ results in:

$$\hat{F}_{PTO_{Clamp}} = \frac{\hat{F}_{ex1} Z_{eq2} - \hat{F}_{ex2} Z_{eq1}}{Z_{eq1} + Z_{eq2}} \quad \text{eq.(17)}$$

3.1.3 Equivalent Single Body Intrinsic Impedance

The equivalent single body intrinsic impedance of the canonical form is determined to be:

$$Z_i = \frac{\hat{F}_{PTO_{Clamp}}}{\hat{u}_{r_{Free}}} = \frac{Z_{eq1} Z_{eq2}}{Z_{eq1} + Z_{eq2}} + Z_{FS2} \quad \text{eq.(18)}$$

Figure 4c depicts the ensuing circuit representation of the WEC canonical form — the equivalent wave excitation force in parallel with both the single body intrinsic impedance and the resistive PTO load. We now utilize eq.(18) to establish conditions on our force source for enabling resonant control on *Arch2*.

3.1.4 Determining the Force Source Reactance to Enable System Resonance

Having derived Z_i in eq.(18) for *Arch2*, we substitute eq.(18) into eq.(2) to enforce the optimal resonant condition and isolate the optimal force source reactance as in eq.(19).

$$X_{FS2_{opt}} = -\Im m \left\{ \frac{Z_{eq1} Z_{eq2}}{Z_{eq1} + Z_{eq2}} \right\} \quad \text{eq.(19)}$$

For *Arch2*, the combination of setting the force source reactance by enforcing eq.(19) while simultaneously setting the PTO resistance according to eq.(3), will maximize the power captured for this architecture.

3.2 The Arch1 Canonical Form:

In Section 3, we identified *Arch1* and *Arch2* as representing the same topology, with the distinction that *Arch1* contains a resistive/reactive PTO and thus, the reactive force source $(\hat{F}_{FS1})$ is defined within the boundary of the PTO. As such, the equivalent float and spar impedances for *Arch1* and *Arch2* are defined by eq.(9) and eq.(10) respectively. In his seminal work on SRPAs, Falnes derived the intrinsic impedance of the canonical form of *Arch1*, with the coupled radiation forces set to zero, as in eq.(20) (cf. (24) [18]).

$$Z_i = \frac{Z_{eq1} Z_{eq2}}{Z_{eq1} + Z_{eq2}} \qquad \text{eq.(20)}$$

To determine the optimal force source reactance $(X_{FS1_{opt}})$ on *Arch1*, the complex-conjugate PTO force control conditions must be applied leading to the optimal settings for the PTO resistance and reactance set as in eq.(21) and eq.(22).

$$R_{PTO_{opt}} = \Re e\{Z_i\} \qquad \text{eq.(21)}$$

$$X_{FS1_{opt}} = \Im m\{Z_i^*\} \qquad \text{eq.(22)}$$

In comparing eq.(22) from *Arch1* with eq.(19) from *Arch2*, it is clear that $X_{FS1_{opt}} = X_{FS2_{opt}}$ and thus, as expected, both *Arch1* and *Arch2* operate under the same resonant control state. Further, comparing eq.(21) with eq.(3) while eq.(2) is enforced, ensures that the PTO resistances are also equivalent. We can therefore conclude, *Arch2* operating with X_{FS2} set to eq.(19) with R_{PTO} set to eq.(3), functions equivalently to *Arch1* operating under complex-conjugate PTO force control. This is important as it demonstrates that, as expected, the resonant control conditions for both *Arch1* and *Arch2* were consistent with one another, however the constraint equation applied to determine the result, eq.(22) or eq.(2) respectively, differed depending on how we defined the PTO boundary. This point may appear as a *semantic* for *Arch2* but is of grave importance to determining the resonant control condition in *Arch3*. For a full derivation of the optimal PTO settings for *Arch1* using the mechanical circuit framework, please consult Bubbar et al. (cf. Section 3.1 [12]).

3.3 The Arch3 Canonical Form:

Bubbar et al.'s process is once again executed on *Arch3* to determine the canonical form parameters ($\hat{u}_{r_{Free}}$, $\hat{F}_{PTO_{Clamp}}$, and Z_i), followed by enforcing the resonant control law in eq.(2) to determine the optimal force source reactance $(X_{FS3_{opt}})$. In Step 1 the mechanical circuit is generated in Figure 6a, and simplified in Step 2 resulting in Figure 6b with new lumped impedance terms, eq.(23) and eq.(24), defined for Z_{eq1} and Z_{eq2} respectively. We note in this case, after applying our circuit simplifications, Z_{FS3} is contained within the definition of Z_{eq2}.

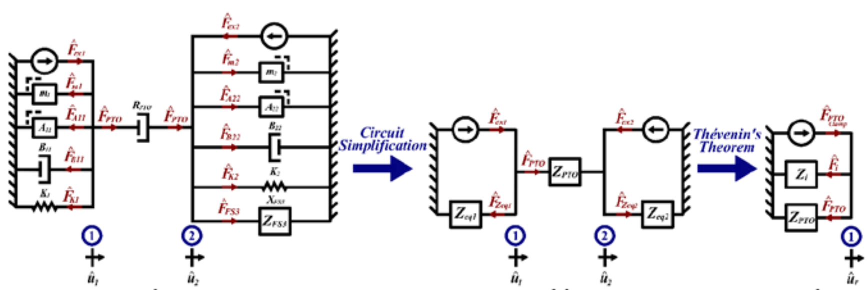

Figure 6: Mechanical Circuits for Arch3:
a) Full Circuit; b) Simplified Circuit; c) WEC Canonical Form

$$Z_{eq1} = Z_{m1} \| Z_{A11} \| Z_{B11} \| Z_{K1} = Z_{m1} + Z_{A11} + Z_{B11} + Z_{K1} = R_{eq1} + iX_{eq1} \qquad \text{eq.(23)}$$

$$Z_{eq2} = Z_{m2} \| Z_{A22} \| Z_{B22} \| Z_{K2} \| Z_{FS3} = Z_{m2} + Z_{A22} + Z_{B22} + Z_{K2} + Z_{FS3} = R_{eq2} + iX_{eq2} \qquad \text{eq.(24)}$$

Next $\hat{u}_{r_{Free}}$, $\hat{F}_{PTO_{Clamp}}$, and Z_i are determined using the augmented mechanical circuits in Figure 7 with details contained in Sections 3.3.1-3.3.3 respectively. Finally the optimal resonant condition is determined by substituting Z_i into eq.(2), to isolate $X_{FS3_{opt}}$ as described in Section 3.3.4.

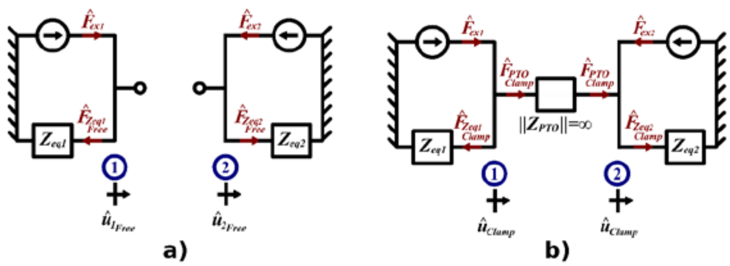

Figure 7: Solving for the Thévenin Equivalent System for Arch3
a) Free Relative Velocity; b) Clamped Through Force

3.3.1 Free Relative Velocity Difference

To determine $\hat{u}_{r_{Free}}$, we apply Kirchhoff's Node Law on each node in Figure 7a resulting in eq.(25)-eq.(26).

$$\hat{F}_{ex1} = Z_{eq1}\hat{u}_{1_{Free}} \,|_{Node_1} \qquad \text{eq.(25)}$$

$$\hat{F}_{ex2} = Z_{eq2}\hat{u}_{2_{Free}} \,|_{Node_2} \qquad \text{eq.(26)}$$

For which we can solve for $\hat{u}_{r_{Free}}$ as:

$$\hat{u}_{r_{Free}} = \hat{u}_{1_{Free}} - \hat{u}_{2_{Free}} = \frac{\hat{F}_{ex2}Z_{eq1} - \hat{F}_{ex1}Z_{eq2}}{Z_{eq1}Z_{eq2}} \qquad \text{eq.(27)}$$

3.3.2 PTO Clamped Through Force:

To determine $\hat{F}_{PTO_{Clamp}}$ we analyze the circuit in Figure 7b and recognize that all the force between nodes 1 and 2 pass through the PTO. As such, $\hat{F}_{PTO_{Clamp}}$ mirrors the result of eq.(17) from Section 3.1.2.

3.3.3 Equivalent Single Body Intrinsic Impedance

The equivalent single body intrinsic impedance is determined as eq.(28) with the canonical form depicted in Figure 6c.

$$Z_i = \frac{\hat{F}_{PTO_{Clamp}}}{\hat{u}_{r_{Free}}} = \frac{Z_{eq1}Z_{eq2}}{Z_{eq1} + Z_{eq2}} \qquad \text{eq.(28)}$$

We now utilize eq.(28) to establish conditions on our force source for enabling resonant control in *Arch3*.

3.3.4 Determining the Force Source Reactance to Enable System Resonance

Having derived Z_i for *Arch3*, we once again apply the optimal resonant condition of eq.(2). To accomplish this, we first substitute the generic complex form $Z_{eqn} = R_{eqn} + iX_{eqn}$, $n = [1, 2]$ into eq.(28) yielding an expression for Z_i based on the equivalent resistances and reactances of the float $(n=1)$ and spar $(n=2)$. We then substitute this expression of Z_i into eq.(2), yielding a quadratic polynomial expression in X_{eq2} described by eq.(29).

$$\frac{(X_{eq1})X_{eq2}^{2} + (R_{eq1}^{2} + X_{eq1}^{2})X_{eq2} + (\mathrm{R}_{eq2}^{2} X_{eq1})}{(\mathrm{R}_{eq1} + \mathrm{R}_{eq2})^{2} + (X_{eq1} + X_{eq2})^{2}} = 0 \qquad \text{eq.(29)}$$

Provided $R_{eq1} \neq -R_{eq2}$ and $X_{eq1} \neq -X_{eq2}$, we can solve for $X_{eq2_{opt}}$, the spar reactance required for system resonance, by applying the quadratic equation to the numerator of eq.(29) yielding the two solutions in eq.(30). These solutions are important as they represent design insight on how system resonance is achieved in *Arch3* through manipulating the spar reactance alone.

$${}^{(1),(2)}X_{eq2_{opt}} = \frac{-(R_{eq1}^{2} + X_{eq1}^{2}) \pm \sqrt{(\mathrm{R}_{eq1}^{2} + X_{eq1}^{2})^{2} - 4(X_{eq1})(R_{eq2}^{2} X_{eq1})}}{2X_{eq1}} \qquad \text{eq.(30)}$$

We note that all variables in eq.(30) can be recovered by applying the analytical real and imaginary operations outlined in eq.(31). Conversely, if we had assumed the float has a variable reactance feature set instead of the spar, the optimal float impedance could be determined by rearranging the numerator in eq.(29) as a polynomial in X_{eq1} and solving for $X_{eq1_{opt}}$ leading to a symmetrical equation to eq.(30) where '*eq2*' is substituted for '*eq1*' and vise versa.

$$R_{eq1} = \Re e\{\text{eq.(23)}\},\ X_{eq1} = \Im m\{\text{eq.(23)}\},\ R_{eq2} = \Re e\{\text{eq.(24)}\} \qquad \text{eq.(31)}$$

To determine the optimal force source reactance, we lump all the hydrodynamics and inertial impedances of the spar into the term Z_{mH2} as in eq.(32), then isolate X_{FS3} in eq.(24), and substitute eq.(30) into this expression yielding eq.(33).

$$Z_{mH2} = Z_{m2} + Z_{A22} + Z_{B22} + Z_{K2} \qquad \text{eq.(32)}$$

$${}^{(1),(2)}X_{FS3_{opt}} = {}^{(1),(2)}X_{eq2_{opt}} - \Im m\{Z_{mH2}\} \qquad \text{eq.(33)}$$

For *Arch3*, enforcing eq.(30) through setting $X_{FS3} = {}^{(1),(2)}X_{FS3_{opt}}$ in eq.(33), will give rise to two different system resonance states in the canonical form. As there are two system resonance states in *Arch3*, it follows that a comparative analysis must be performed. Having derived the optimal force source reactances to enable system resonance, the outstanding question at this point is what, if any, are the performance differences of *Arch2* and *Arch3* when operating under system resonant conditions with the PTO resistance set optimally. We answer this question in the next section.

4 Numerical Examples of WEC Configurations

The focus of this section is to demonstrate how the analytical constraints defining the optimal force source reactances, determined in Section 3, can be used to enforce the resonant conditions on each architecture considered. We achieve this through performing a comparative numerical analysis using physical parameters from an experimentally verified SRPA 1/25th Froude-scaled model, resembling a WaveBOB™ device, published by Beatty et al. and detailed in Appendix A (cf. 'WEC A' [13,19]). To perform this comparative analysis, a series of configurations are defined that are built on the parameters extracted from Beatty et al.'s single experimental model. To ensure equitable comparisons are based on performance, each of the configurations considered have the same: 1) hydrodynamic coefficients—the sizes and shapes of components do not change, and 2) total mass. We note at this stage of the analysis the reactive force source is represented conceptually without a physical embodiment. An embodied design of the reactive force source will be specified in Section 5.2.

To perform this comparative analysis, we first reproduce the same two SRPA WEC configurations originally published by Beatty et al. based on their experimental results. We note both of these configurations are based upon *Arch1* with the only distinguishing difference being the PTO force control mode – *Config1* is amplitude controlled, while *Config2* is complex-conjugate controlled. *Config1* and *Config2* serve as comparative baselines as neither contain a geometry control feature set external to the PTO. A third configuration, *Config3*, is generated based on *Arch2* of Figure 2b, while the last two configurations, *Config4* and *Config5*, are generated based on each of the resonant states derived for *Arch3* of Figure 2c. Numerical models of all *Config1-5* are constructed by substituting Beatty et al.'s model parameters verbatim into the equation sets detailed in Table 1.

Table 1: Overview of Configurations Used in the Comparative Analysis

Architecture:	**Configuration:**	Z_i	Z_{PTO}	X_{FSn}	Z_{eq2}
Arch1	***Config1***	eq.(20)	eq.(3)	-	eq.(10)
Arch1	***Config2***	eq.(20)	eq.(21), eq.(22)	-	eq.(10)
Arch2	***Config3***	eq.(18)	eq.(3)	X_{FS2} = eq.(19)	eq.(10)
Arch3	***Config4***	eq.(28)	eq.(3)	${}^{(1)}X_{FS3}$ = eq.(33)	eq.(24)
Arch3	***Config5***	eq.(28)	eq.(3)	${}^{(2)}X_{FS3}$ = eq.(33)	eq.(24)

In the subsequent sections, we explore the comparative performance of these configurations. Section 4.1 focuses on confirming whether optimal phase control is achieved for each configuration. Section 4.2 presents the power capture performance of each of these configurations, detailing the source of differences, and establishing *Config5* as the superior performing configuration.

4.1 Was Optimal Phase Control Achieved?

In Section 1, we made the conscious decision to revert to an earlier interpretation of the optimal phase control problem as 'enforcing the state of system resonance', allowing for the derivation of the generalized resonant conditions for the complex SRPA WEC architectures considered in this work. In this section, we demonstrate, using our numerical examples, that optimal phase control is achieved when the resonant conditions are enforced. In equation form, this requires that eq.(34) [18] is satisfied at each excitation frequency considered.

$$\gamma(\omega) = \measuredangle \hat{F}_{PTO_{Clamp}}(\omega) - \measuredangle \hat{u}_r(\omega) = 0 \qquad \text{eq.(34)}$$

We perform a comparative analysis by evaluating eq.(34) for each of the configurations detailed in Table 1 and plot the results versus Wave Excitation Frequency in Figure 8a. In observing Figure 8a, all the configurations except *Config1* adhere to the constraint outlined in eq.(34), and are thus, operating under optimal phase control. As anticipated, *Config1* cannot satisfy eq.(34) at all wave excitation frequencies as the PTO is purely resistive and there is no reactive feature set present to enable system resonance across the frequency band.

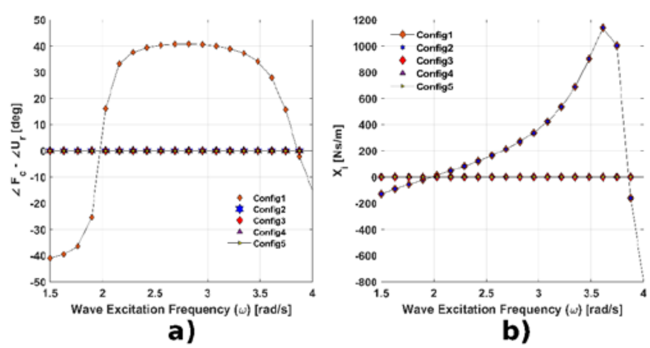

Figure 8: Plot of All Five WEC Configurations versus Wave Excitation Frequency:
a) Plot of $\measuredangle \hat{F}_{PTO_{Clamp}}(\omega) - \measuredangle \hat{u}_r(\omega)$; b) Intrinsic Reactance (X_i)

To expose the relationship between the optimal phase control condition in eq.(34) and the resonant control law presented in eq.(2), we plot the intrinsic reactance of the canonical form, $X_i(\omega)$, as a function of wave excitation frequency in Figure 8b using the corresponding form of Z_i specified in Table 1.

In Figure 8b we note *Config3-5*, all with geometry control feature sets external to the PTO, adhere to eq.(2), while *Config1-2* do not. The peculiar observation of *Config2* not adhering to the resonant control law of eq.(2), yet clearly enacting optimal phase control requires further elaboration and an explanation follows.

In specifying the topological layout of *Config2* based on *Arch1*, we had intentionally defined the boundary of the PTO to comprise of the single complex quantity Z_{PTO}, containing both R_{PTO} and X_{FS1}. Upon constructing the canonical form, Thévenin's theorem is applied across the nodes of Z_{PTO}, resulting in X_{FS1}, the quantity responsible for enforcing eq.(34), residing outside the definition of Z_i.

In contrast, in *Arch2* and *Arch3*, for which *Config3-5* are based on, the PTO boundary contains R_{PTO} only whereby Thévenin's theorem is applied across, necessitating that Z_i in eq.(18) contains X_{FS2}. In this sense, X_{FS2} is separate from the PTO while still being responsible for satisfying eq.(2) via implementing eq.(19). As demonstrated in Section 3.2, *Arch1* and *Arch2* are topologically equivalent requiring the same conditions on the PTO resistance and force source reactance for enabling system resonance. However, in *Arch1*, the choice of defining the boundary of the PTO to include the reactive force source has the effect of invalidating eq.(2) as a measure of system resonance. This occurs as eq.(2) defines the natural frequency of the canonical form, and only represents the condition of system resonance if the feature set enforcing eq.(2) resides within the definition of Z_i as in *Config3* of *Arch2*. This *semantic* of defining the PTO boundary to include the reactive force source has the unintended consequence of invalidating eq.(2) as a means to enforce optimal phase control. The significance of this choice is WEC developers are unaware that alternative WEC architectures exist, which do not implement the traditional complex-conjugate PTO force control method, but contain the capacity for much greater power capture potential. We, therefore, recommend that within linear monochromatic WEC models, the reactive force source should always be defined outside the PTO boundary with the role to satisfy eq.(2).

4.2 Power Capture Analysis

The following section explores the power capture performance of *Config1-5* in the context of the canonical form parameters via eq.(35) originally derived by Falnes (cf. (28)-(30) [18]).

$$P_U = \frac{1}{2} | \hat{F}_{PTO_{Clamp}} || \hat{u}_r | \cos(\gamma) - \frac{1}{2} \Re e\{Z_i\} | \hat{u}_r |^2 \qquad \text{eq.(35)}$$

To perform this comparison we generate data for: 1) $P_U(\omega)$ — monochromatic power capture, 2) $|\hat{F}_{PTO_{Clamp}}(\omega)|$ — amplitude of the equivalent excitation force, and 3) $|\hat{u}_r(\omega)|$ — amplitude of the relative body velocity between the float and spar; all as a function of wave excitation frequency, resulting in the three individual plots of Figure 9 respectively.

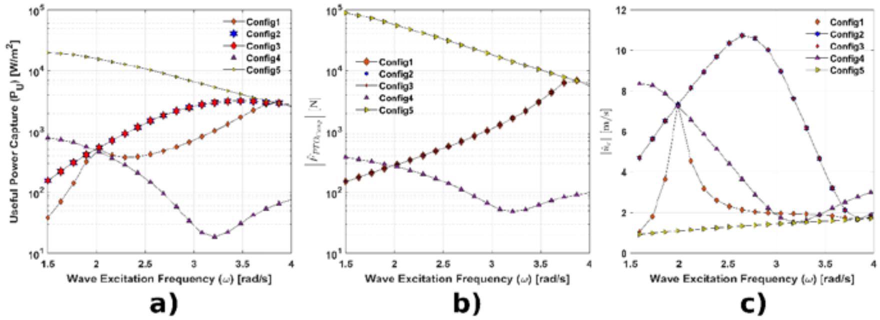

Figure 9: Frequency Response of Kinematic and Dynamic Quantities for *Config1-5*:
a) Normalized Useful Power Capture; b) Amplitude of the Equivalent Excitation Force;
c) Amplitude of the Relative Float to Spar Velocity

We begin by reviewing Figure 9a which exhibits the power capture frequency response of *Config1-5*, with *Config1* and *Config2* coincident with the results published by Beatty et al. (cf. Fig. 15 [13]). Although *Config2-5* are all operating under resonant control, their power capture responses vary widely. This behaviour confirms that multiple resonant conditions exist that are not equal when it comes to the power capture of complex WEC architectures. Solely enforcing system resonance should not be the end goal of WEC geometry control in the SRPA architecture. Rather the specific topology of the WEC architecture and the resonant control scheme greatly influences the power capture potential. To comprehend this result we must explore the corresponding frequency responses of $|\hat{F}_{PTO_{Clamp}}(\omega)|$ and $|\hat{u}_r(\omega)|$ of Figure 9b-c respectively. First, in reviewing Figure 9b we note that $|\hat{F}_{PTO_{Clamp}}(\omega)|$ is coincident for *Config1-3* and differs for *Config4-5*. The reason for this observation is traced back to the form of $|\hat{F}_{PTO_{Clamp}}(\omega)|$ in eq.(17) and its dependency on Z_{eq2}. Since neither X_{FS1} or X_{FS2} are contained within the definition of Z_{eq2} in eq.(10) for *Arch1* or *Arch2*, $|\hat{F}_{PTO_{Clamp}}(\omega)|$ is the same for *Config1-3*. This same reasoning also explains why *Config4-5* exhibit vastly different responses for $|\hat{F}_{PTO_{Clamp}}(\omega)|$ as X_{FS3} is contained within Z_{eq2} in eq.(24). This dependency between $|\hat{F}_{PTO_{Clamp}}(\omega)|$ and X_{FS3} has the effect of both lowering, as in *Config4*, and increasing, as in *Config5*, the frequency response of $|\hat{F}_{PTO_{Clamp}}(\omega)|$ relative to *Config1*-3. The benefit to increasing power capture via increasing $|\hat{F}_{PTO_{Clamp}}(\omega)|$ is clear in eq.(35) with *Config5* displaying the superior response.

Another important parameter to review is $|\hat{u}_r(\omega)|$, as it not only influences the power capture in eq.(35) but informs a WEC designer of predicted end stop collisions [18]. In comparing *Config1* with *Config2*, as noted above $|\hat{F}_{PTO_{Clamp}}(\omega)|$ is the same, but the power capture response of *Config2* is larger. Based on eq.(35) this necessitates that $|\hat{u}_r(\omega)|\cos(\gamma)$ must compensate with $\cos(\gamma)\rightarrow 1$ and $|\hat{u}_r(\omega)|$ increasing, which is what we observe in Figure 9c. Hence, the effect of transitioning an SRPA between an amplitude control PTO (as in *Config1*) to a complex-conjugate controlled PTO (as in *Config2* or *Config3*) is to realize larger device motions resulting in increased power capture [7]. This choice incurs additional risk to the WEC developer as there is a higher probability of end stop collisions due to float-spar oscillations. The conclusion here is that *Config1-3* based on *Arch1* and *Arch2* are inherently flawed as increases in power capture are only based on increasing the oscillation amplitude across the PTO.

Proceeding on we compare *Config3*, based on *Arch2*, with *Config4* and *Config5*, based on *Arch3*. In exploring Figure 9a, we note *Config4* is only larger in $P_U(\omega)$ relative to *Config3* in the frequency range $\omega < 2\ rad/s$ as a result of both larger $|\hat{F}_{PTO_{Clamp}}(\omega)|$ and $|\hat{u}_r(\omega)|$. In contrast, *Config5* exhibits the largest $P_U(\omega)$ response over the entire frequency range of

$1.5 < \omega < 4\ rad/s$, which is clearly attributed to a significantly larger force response, $|\hat{F}_{PTO_{Clamp}}(\omega)|$, with the added benefit of a small velocity response, $|\hat{u}_r(\omega)|$. Clearly, the power capture response of *Config5*, based on *Arch3*, is superior to all the alternatives in this analysis, and it remains to discuss how the reactance ${}^{(2)}X_{FS3_{opt}}$ can be realized using machinery.

5 Subsystem Architecture Design and Technology Innovation

Up to this point, we have identified a high performing configuration in *Config5* of *Arch3*, however we have yet to specify how the optimal force source reactance, ${}^{(2)}X_{FS3_{opt}}$, will be physically realized. Section 5.1 will focus on a brief review of a promising technology, inerters, as applied to wave energy conversion. Section 5.2 will follow by presenting a subsystem circuit that is systematically substituted for the optimal force source element. In this substitution, we will apply realistic physical constraints on the design and generate a feasible power capture response based on approximating the optimal force source frequency response. In Section 5.3 we will compare these power capture results against *Config1,2,5* in Figure 9a, experimental data previously published by Beatty et al. [13], and the SRPA power capture limit $(P_{U_{Max}}|_{opt})$ previously published by Bubbar and Buckham [21]. Finally, we conclude by presenting an explanation of how these power capture responses relate to the complexity of a WEC control regime.

5.1 Review of Inerter Technology

Developed by Smith [22] and formally introduced into the wave energy community by Bubbar and Buckham [21], inerters are mechanical devices capable of temporarily storing and delivering mechanical reactive power during an oscillation cycle. Inerters achieve this through converting relative translational mechanical motion into rotational motion of a flywheel, which exerts an opposing reaction force proportional to the relative acceleration as measured at the device nodes. This proportionality constant is known as the *inertance*, has SI units of kilograms, and is denoted as m_{eff} in this work. In general, the inertance is calculated as the product of the transmission ratio squared (β^2) with the moment of inertia of the flywheel (J) as in eq.(36) [23], and semi-active inerters are devices for which online adjustments of the inertance are permitted [24].

$$m_{eff} = \beta^2 J \qquad \text{eq.(36)}$$

Similar to mass elements, inerters induce a phase delay between the reaction force and the relative translational velocity as measured between its terminals. At present, three types of inerters exist: 1) rack and pinion [22], 2) reverse driven ball screw [25], and 3) hydraulic [26], for which the definition of β varies with each type. Inerters are signified as a flywheel in the mechanical circuit framework with the frequency domain constitutive equation described in Table 2.

Table 2: Mechanical Circuit Element for the Inerter

Element Description:	Circuit Element	Constitutive Equation
Inerter	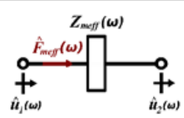	$Z_{meff}(m_{eff},\omega) = i\omega m_{eff}(\omega)$ $\hat{F}_{meff}(\omega) = Z_{meff}(m_{eff},\omega)[\hat{u}_1(\omega) - \hat{u}_2(\omega)]$

5.2 Substitution of Force Sources for Invoking Technology Innovation

For *Config5* to operate under resonant control, the force source reactance, X_{FS3}, is scheduled across the operating frequency range to ensure ${}^{(2)}X_{eq2_{opt}}$ in eq.(30) is satisfied. The force source at this point is still conceptual—a physical embodiment has not been defined. The utility of establishing the optimal force source reactance ${}^{(2)}X_{FS3_{opt}}$ in eq.(33) prior to defining the physical embodiment is it provides WEC designers with a tangible design constraint *prior* to specifying how this constraint must be satisfied, thereby opening up the possibility for innovative designs.

In reviewing the schematic of *Arch3* in Figure 2c, we note the *conspicuous* proposal of interfacing the spar to the ocean floor via X_{FS3}. Such a conceptual design, although predicted to increase device performance, is highly impractical in deep-water operation. In reality, our choice of specifying the topology in *Arch3* was to allow for a complete generalization of the ensuing conceptual design space, with an expectation that we would replace X_{FS3} with a feasible topology of linear mechanical components.

For example, we present a series of subsystems formed from linear mechanical components, which can satisfy this lone requirement in Figure 10: a) semi-active inerter interfaced between the spar and ocean floor; b) variable spring interfaced between the spar and ocean floor; c) variable hydrodynamic added mass via deformable spar hull; d) variable physical mass via water ballasting; and e) reaction mass internal to the spar, interfaced with a parallel combination of a semi-active inerter and constant spring. Although we have presented five potential subsystem circuits in Figure 10a-e, this list is by no means comprehensive.

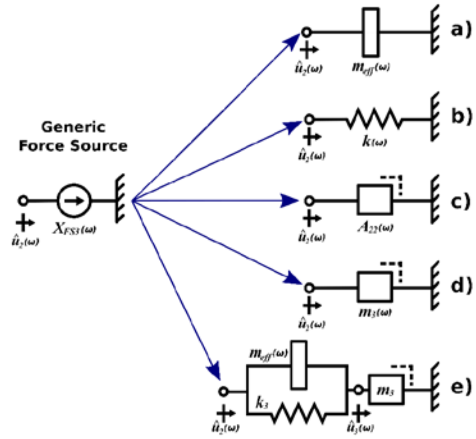

Figure 10: Mechanical Subsystem Schematic Replacements for X_{FS3}
a) Semi-active Inerter Tied to Ground; b) Variable Spring Tied to Ground;
c) Variable Spar Added Mass via Deformable Hull;
d) Variable Spar Physical Mass via Water Ballast;
e) Reaction Mass Internal to Spar with Parallel Semi-Active Inerter and Constant Spring

In this work, we select the subsystem circuit of Figure 10e to perform our substitution and provide a physical embodiment of X_{FS3}. In the corresponding subsystem, the geometry control variable is the inertance, $m_{eff}(\omega)$, whereas the reaction mass, m_3, and coupled spring, k_3, are constant and require specification. As a first step, to maintain an equitable comparison, we must ensure the total mass of the spar and the reaction mass subsystem in this configuration is the same as the mass of the original spar used in Beatty et al.'s experimental work. As such, we choose to set the sum of the masses m_2 and m_3 in *Config5* equal to the mass of Beatty et al.'s original spar following $m_2 = m_3 = 57.5$ kg. Next, to offset the gravitational force from m_3 and place it at the centre of travel inside the spar, we specify a constant spring stiffness of $k_3 = 2000\ N/m$.

To determine the inertance $m_{eff}(\omega)$ frequency response required to enforce ${}^{(2)}X_{FS3_{opt}}$, we develop an equation describing the equivalent reactance of this subsystem circuit by applying circuit simplification transformations to the subsystem circuit of Figure 10e. We then equate this expression to ${}^{(2)}X_{FS3_{opt}}$, required to enforce optimal phase control, yielding eq.(37). Finally, we substitute the impedance relationships (cf. Table 1 [12]) for each term in eq.(37) and solve for the optimal inertance, $m_{eff_{opt}}(\omega)$, to give eq.(38).

$$ {}^{(2)}X_{FS3_{opt}}(\omega) = \Im m\{Z_{meff} \,\|\, Z_{k3} \circ\!\!-\!\!\circ\, Z_{m3}\} = \frac{(X_{meff} + X_{k3})X_{m3}}{X_{meff} + X_{k3} + X_{m3}} \qquad \text{eq.(37)} $$

$$ m_{eff_{opt}}(\omega) = \frac{k_3 m_3 + {}^{(2)}X_{FS3_{opt}}(\omega)\left(\omega m_3 - \dfrac{k_3}{\omega}\right)}{\omega[\omega m_3 - {}^{(2)}X_{FS3_{opt}}(\omega)]} \qquad \text{eq.(38)} $$

We note in calculating $m_{eff_{opt}}(\omega)$ using eq.(38), we must supply the updated value for $m_2 = 57.5kg$ into eq.(32) to calculate ${}^{(2)}X_{FS3_{opt}}$. The frequency response of $m_{eff_{opt}}(\omega)$ is plotted in Figure 11 with two key observations. First, $m_{eff_{opt}}(\omega)$ becomes negative at $\omega \approx 3.5\ rad/s$ which is impossible to satisfy with the chosen subsystem design. Second, a vertical asymptote is observed at $\omega \approx 3.85\ rad/s$ where the denominator of eq.(38) tends to zero, drastically extending the range of $m_{eff_{opt}}(\omega)$. To circumvent these challenges, we select a feasible inertance operating range of $m_{eff} = [m_{eff_{\min}}, m_{eff_{\max}}] = [100, 830]\ kg$. We choose $m_{eff_{\min}} = 100kg$ as extreme low values of inertance are challenging to achieve due to the quadratic relationship of the moment of inertia with the radius of gyration as inferred in eq.(36). This feasible inertance range allows for $m_{eff_{opt}}(\omega)$ to be satisfied for the frequency range of $\omega = [1.5, 3.16]\ rad/s$, with the compromise of setting $m_{eff} = 100\ kg$ for all frequencies in the range $3.16 \le \omega \le 4\ rad/s$. In specifying these realistic design constraints, we have in essence created a new configuration, we label as *Config6*, for which we will present a comparative power capture response in Figure 12 of Section 5.3 to outline the consequence of this trade-off.

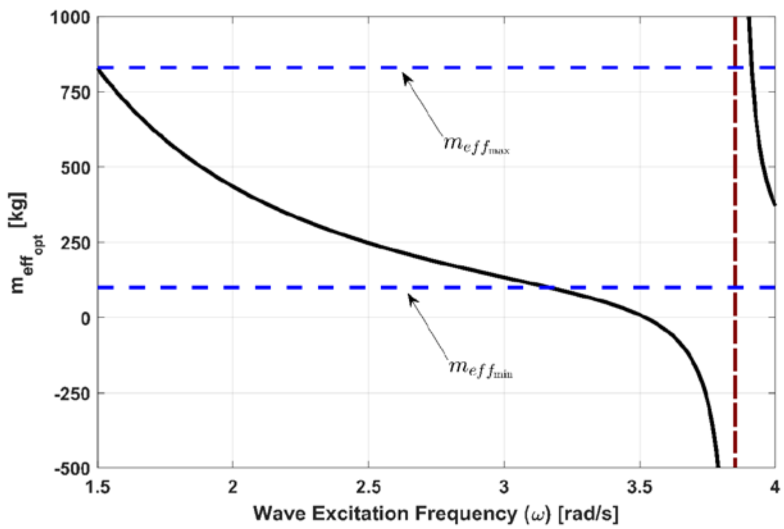

Figure 11: Plot of $m_{eff_{opt}}(\omega)$ versus Wave Excitation Frequency:

The combination of the WEC model parameters and the chosen subsystem circuit created a scenario in which the full range of ${}^{(2)}X_{eq2_{opt}}$ could not be satisfied across the frequency spectrum. Trade-offs were required to allow for a feasible configuration that implemented resonant control for a majority of the frequency range. To further broaden the bandwidth of operation, a WEC designer may consider: 1) redesigning the device to alter the WEC model parameters to allow for a more suitable frequency response of ${}^{(2)}X_{eq2_{opt}}$ to be satisfied by a feasible range of $m_{eff_{opt}}$, and /

or 2) replacing X_{FS3} with a different subsystem circuit which theoretically can satisfy ${}^{(2)}X_{eq2_{opt}}$ through supplying the required negative reactance values of $X_{FS3_{opt}}$.

5.3 Comparison of Numerical Results with Experimental Data

In this final section we quantify the power capture performance of *Config1,2,5,6* proposed in this work in relation to data obtained from experimental trials performed by Beatty et al. [13], for which these configurations are based.

To begin, we define the datasets observed in Figure 12. Six overlaid datasets of power capture as a function of excitation frequency are noted. The first three are *Config1,2,5* originally presented in Figure 9a and described in detail in Section 4.2. Next, we observe P_{Exp} based on the experimental trails conducted by Beatty et al. [13] performed in a monochromatic wave regime using a PTO simulator [27] that generates an amplitude controlled PTO force response [7]. As originally presented by Beatty et al. [13], there is good alignment of *Config1* with P_{Exp} and thus confidence in the linearized hydrodynamic and inertial parameters used in all the configurations presented. The next dataset is *Config6*, defined using the subsystem circuit of Figure 10e in Section 5 and based on a feasible operating range of $m_{eff}(\omega)$ for best approximating ${}^{(2)}X_{FS3_{opt}}$. Clearly, the power capture response of *Config6* is coincident with *Config5*, until $\omega = 3.16\ rad/s$ — the frequency at which the inerter of *Config6* can no longer supply the required inertance to maintain resonant control. Above $\omega = 3.16\ rad/s$ we observe a steep decline in power capture. The final dataset is $P_{U_{Max}}|_{opt}$ represents the upper bound in power capture by a SRPA with a complex-conjugate controlled PTO and an optimally set inertial modulated spar as originally introduced by Bubbar and Buckham [21].

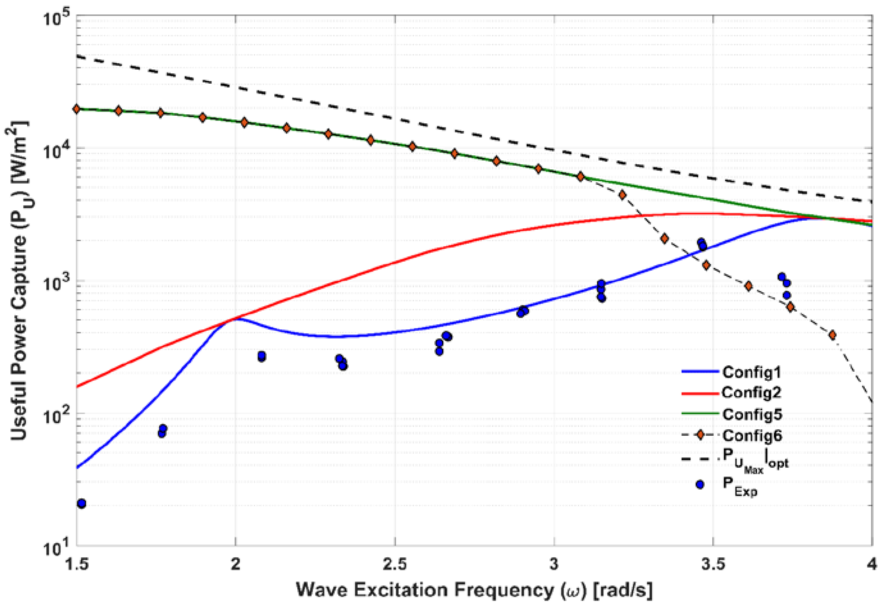

Figure 12: Power Capture Frequency Response for Various SRPA Configurations Adapted from [21]

To understand how a WEC designer leaps up on the configuration chart of Figure 12, we explore the relationship between the complexity of the WEC control regimes to the resulting power capture performance when the WEC is represented in canonical form. We first qualitatively describe the complexity of the WEC control regime as a combination of both the: 1) number of simultaneous control parameters, and 2) the dependencies of these control parameters upon one another. A summary of these attributes are pictorially represented in Figure 13 for the configurations considered. Clearly, *Config1*, with the lowest power capture performance, enacts the simplest control regime, an amplitude controlled PTO with R_{PTO} set optimally to eq.(3) as the single control variable with no geometry control feature set present to influence the system dynamics. Next, *Config2* enacts a more complicated control regime with improved power capture utilizing a complex-conjugate PTO with two controlled parameters—R_{PTO} set optimally to eq.(21) and X_{PTO} set optimally to eq.(22), but again without a geometry control feature set present. The subsequent configuration is *Config5* with again two controlled parameters, however there is an additional dependency between these parameters manifesting in a *master-slave relationship* [12], for which the value set in the *master* parameter, Z_{FSn}, influences the optimal value set in the slave *parameter*, R_{PTO}. Optimal power capture is achieved when the spar dynamics are set through Z_{FSn} to induce system resonance, with R_{PTO} being subsequently set based on Z_{FSn} to maximize the power capture. Finally, the most complex and highest performing regime is the $P_{U_{Max}}|_{opt}$ configuration, containing three controllable parameters—one *master* parameter, Z_{FSn}, which influences the spar dynamics, and two *slave* parameters, X_{PTO} and R_{PTO}, which set the resonant state and maximize power capture respectively.

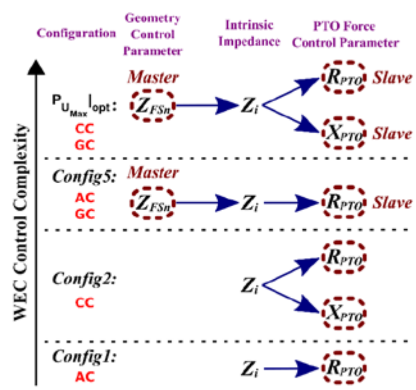

Figure 13: Classification of WEC Control Complexity for all WEC Configurations
with Red Dashed Squares Highlighting a Control Parameter
and Blue Arrows Describing Parameter Dependencies
AC≡Amplitude Control, CC≡Complex-Conjugate Control, GC≡Geometry Control

In reviewing Figure 12, we note the gap between *Config2* and *Config5* is substantial justifying the added complexity of introducing a *master-slave relationship*. However, the gap between *Config5* and $P_{U_{Max}}|_{opt}$ is smaller and requires an additional dependent control parameter introducing a further complex technological design challenge. Clearly, this relationship between WEC control complexity and power capture is non-linear and thus, a WEC developer must cautiously consider the appropriate control complexity to power capture ratio applicable for their development program.

6 Conclusions

For wave energy to become an economically viable form of renewable energy, the power capture performance of WEC devices must continue to improve. To succeed with this challenge, WEC developers must be encouraged to focus on devices with more promising power capture potential early on in the conceptual design phase of a development program. To support the identification of WEC architectures with a promising power capture performance, we proposed an analytical method previously unavailable to WEC developers, based on transforming an arbitrarily complex WEC architecture into a simplified canonical form, to extract analytical expressions on how to achieve system resonance.

We followed this proposal with a case study implementing the method to extract design insights to compare five WEC configurations based upon three complex SRPA WEC architectures, the last two of which incorporated an embedded geometry control feature set. We then demonstrated using numerical models, that although the WEC architectures are similar in topology, power capture performance can vary greatly necessitating important considerations on WEC topology and its influence on the equivalent single body excitation force early in the conceptual phase of development. We followed by demonstrating how the generality of the analytical method offered a performance target for the design of a subsystem without constraining the design to a specific technology. We revealed how multiple potential subsystems could be simultaneously considered to satisfy the analytical performance requirements leading to the selection of a subsystem circuit implementing inertial modulation using inerter technology. Finally, we presented an explanation of a power capture hierarchy of the WEC configurations under study in the context of the ensuing complexity of the control regime revealed through our numerical analysis.

Although this work has offered a new viewpoint on the utility of monochromatic linear frequency domain WEC models in the conceptual design stage of a development program, our future outlook will focus on the following areas: 1) exploration of alternative subsystem circuits capable of satisfying the optimal spar reactance, 2) sensitivity analysis of the presented control parameters in the context of power capture, 3) methods for developing time-domain WEC models operating under the control regimes presented, and 4) fabricating a scaled model using an inerter and performing experimental trails in a wave tank.

Acknowledgments

We would like to acknowledge the support of the Natural Sciences and Engineering Research Council of Canada (NSERC) in funding this research.

References

[1] S. Astariz, G. Iglesias, The economics of wave energy: A review, Renew. Sustain. Energy Rev. 45 (2015) 397–408. doi:10.1016/j.rser.2015.01.061.

[2] A. Babarit, Ocean Wave Energy Conversion: Resource, Technologies and Performance, Elsevier, 2017.

[3] J. Weber, WEC Technology Readiness and Performance Matrix–finding the best research technology development trajectory, in: Int. Conf. Ocean Energy, 2012.

[4] A.F. de O. Falcão, Wave energy utilization: A review of the technologies, Renew. Sustain. Energy Rev. 14 (2010) 899–918. doi:10.1016/j.rser.2009.11.003.

[5] J. Cruz, ed., Ocean wave energy: current status and future prepectives [i.e. perspectives], Springer, Berlin, 2008.

[6] P. Nebel, Maximizing the efficiency of wave-energy plant using complex-conjugate control, Proc. Inst. Mech. Eng. Part J. Syst. Control Eng. 206 (1992) 225–236.

[7] J. Falnes, Ocean waves and oscillating systems: linear interactions including wave-energy extraction, Cambridge University Press, Cambridge ; New York, 2002.

[8] C. Liang, X. Li, D. Martin, A. Wise, R. Parker, K. Ngo, L. Zuo, Dynamics and Power Absorption of a Self-React Wave Energy Converter With Mechanical Power Takeoff System, (2017) V006T10A052. doi:10.1115/DETC2017-67464.

[9] M. Gradowski, M. Alves, R.P. Gomes, J.C. Henriques, Integration of a hydrodynamic negative spring concept into the OWC Spar Buoy, in: Cork, Ireland, 2017.

[10] C.C. Mei, Power extraction from water waves, J. Ship Res. 20 (1976) 63–66.

[11] D.V. Evans, A theory for wave-power absorption by oscillating bodies, J. Fluid Mech. 77 (1976) 1–25. doi:10.1017/S0022112076001109.

[12] K. Bubbar, B. Buckham, P. Wild, A method for comparing wave energy converter conceptual designs based on potential power capture, Renew. Energy. (n.d.). doi:10.1016/j.renene.2017.09.005.

[13] S.J. Beatty, M. Hall, B.J. Buckham, P. Wild, B. Bocking, Experimental and numerical comparisons of self-reacting point absorber wave energy converters in regular waves, Ocean Eng. 104 (2015) 370–386.

[14] C.M. Harris, C.E. Crede, H.M. Trent, Shock and Vibration Handbook Vol I, 1st ed., 1962. http://adsabs.harvard.edu/abs/1962PhT....15i..65H (accessed December 23, 2015).

[15] A.A.E. Price, C.J. Dent, A.R. Wallace, On the capture width of wave energy converters, Appl. Ocean Res. 31 (2009) 251–259. doi:10.1016/j.apor.2010.04.001.

[16] K. Budal, Floating structure with heave motion reduced by force compensation, in: Proc. Fourth Int. Offshore Mech. Arct. Eng. Symp., 1985: pp. 92–101.

[17] L. Thévenin, Sur un nouveau théoreme d'électricité dynamique [On a new theorem of dynamic electricity], CR Séances L'Académie Sci. 97 (1883) 159–161.

[18] J. Falnes, Wave-Energy Conversion Through Relative Motion Between Two Single-Mode Oscillating Bodies, J. Offshore Mech. Arct. Eng. 121 (1999) 32–38. doi:10.1115/1.2829552.

[19] S. Beatty, Self-Reacting Point Absorber Wave Energy Convertors, University of Victoria, 2015.

[20] U.A. Korde, On providing a reaction for efficient wave energy absorption by floating devices, Appl. Ocean Res. 21 (1999) 235–248.

[21] K. Bubbar, B.J. Buckham, On Establishing an Analytical Power Capture Limit for Self-Reacting Point Absorber Wave Energy Converters Based on Dynamic Response, Appl. Energy. (2018). **Currently Under Review**

[22] M.C. Smith, Synthesis of mechanical networks: the inerter, IEEE Trans. Autom. Control. 47 (2002) 1648–1662. doi:10.1109/TAC.2002.803532.

[23] Y. Hu, M.Z.Q. Chen, S. Xu, Y. Liu, Semiactive Inerter and Its Application in Adaptive Tuned Vibration Absorbers, IEEE Trans. Control Syst. Technol. 25 (2017) 294–300. doi:10.1109/TCST.2016.2552460.

[24] M.Z.Q. Chen, Y. Hu, C. Li, G. Chen, Semi-active suspension with semi-active inerter and semi-active damper, IFAC Proc. Vol. 47 (2014) 11225–11230. doi:10.3182/20140824-6-ZA-1003.00138.

[25] M.Z.Q. Chen, C. Papageorgiou, F. Scheibe, F. Wang, M.C. Smith, The missing mechanical circuit element, IEEE Circuits Syst. Mag. 9 (2009) 10–26. doi:10.1109/MCAS.2008.931738.

[26] F.-C. Wang, M.-F. Hong, T.-C. Lin, Designing and testing a hydraulic inerter, Proc. Inst. Mech. Eng. Part C J. Mech. Eng. Sci. 225 (2011) 66–72. doi:10.1243/09544062JMES2199.

[27] S. Beatty, F. Ferri, B. Bocking, J.P. Kofoed, B. Buckham, Power Take-Off Simulation for Scale Model Testing of Wave Energy Converters, Energies. 10 (2017) 973. doi:10.3390/en10070973.

7 Appendix A: Physical SRPA Model Specifications

The motivation of Appendix A is to describe the physical design parameters associated with Beatty et al.'s [13] SRPA WEC model used to perform the numerical analysis presented in Sections 4-5. We highlight key dimensions in Figure 14 with an overview of the model parameters listed in Table 3. Detailed frequency response plots of the linear hydrodynamic coefficients can be found in Beatty et al. [13].

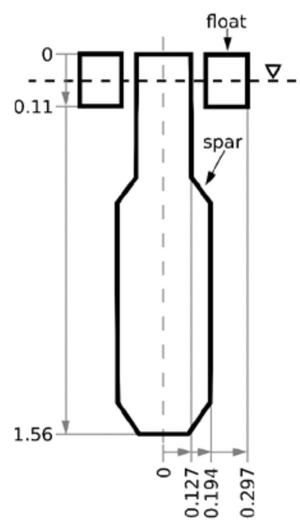

Figure 14: Simplified Cross-Sectional Drawing of the
Original SRPA WEC Configuration Adapted from [13]
Callouts in Metres

Table 3: Overview of Inertial and Hydrodynamic Parameters of the 1/25 WEC Model Adapted from [13]

Parameter	Value	Units
Float		
Outer diameter	0.595	m
Inner diameter	0.317	m
Hydrostatic stiffness	2000	N/m
Physical mass	12	kg
Radiation damping (min, max)	8.90, 59.6	Ns/m
Added mass (min, max)	27.6, 32.7	kg
Excitation force (min, max)	1290, 1850	N/m
Spar		
Hydrostatic stiffness	509.5	N/m
Physical mass	115	kg
Total damping (min, max)	39.74, 69.13	Ns/m
Added mass (min, max)	64.22, 67.81	kg
Excitation force (min, max)	16.00, 337.5	N/m